
First Principles Quantitative Modeling of Molecular Devices

Zhanyu Ning

Centre for the Physics of Materials

Department of Physics

McGill University

Montréal, Québec

Canada

A Thesis submitted to the
Faculty of Graduate Studies and Research
in partial fulfillment of the requirements for the degree of
Doctor of Philosophy

© Zhanyu Ning, 2010

*To
my parents and my wife huanhuan.*

CONTENTS

Abstract	xiii
Résumé	xv
Statement of Originality	xvii
Acknowledgments	xix
Abbreviations and Symbols	xx
1 Introduction	1
2 Theory of Electronic Structure	7
2.1 The Born-Oppenheimer approximation	7
2.2 Density functional theory	8
2.2.1 The Hohenberg-Kohn(HK) theorem	9
2.2.2 The Kohn-Sham equation	10
2.2.3 Exchange-correlation energy functionals	14
2.2.4 Numerical implementation of DFT	19
3 Quantum transport theory	27
3.1 The Landauer quantum transport theory	28
3.2 The non-equilibrium Green's function theory	30
3.2.1 NEGF and Landauer theory	31
3.2.2 Construction of nonequilibrium charge density	33
3.3 Implementation of the NEGF theory	36
3.3.1 Two-probe model	36
3.3.2 2-D Brillouin zone sampling	38
3.3.3 Self-energy	39
3.3.4 Contour integration	39
3.3.5 The NEGF-DFT approach	40
3.4 Summary	42
4 Tunnel Magnetoresistance of molecular wires	43
4.1 Introduction to spintronics	43
4.2 Tunnel Magnetoresistance	46
4.3 Experimental and theoretical background	48
4.4 Calculation details	50
4.5 Calculation results	54
4.5.1 Analysis of spin injection	57
4.5.2 Spin polarized current and TMR	58
4.6 Summary and outlook	61

5	Transport in molecular wires: the role of contacts	63
5.1	The Au/BDT/Au: background	66
5.1.1	Experimental measurements	66
5.1.2	Theoretical analysis	68
5.2	Calculation of the Au/BDT/Au junction	71
5.2.1	Total energy structural relaxation	71
5.2.2	Junction breakdown force	74
5.2.3	Bond Energies	80
5.2.4	Conductance	83
5.2.5	Scattering states	84
5.3	Charged systems	86
5.3.1	Two charged models	87
5.3.2	Conductances	88
5.4	Other molecular junctions	92
5.4.1	Total energy and conductance	94
5.5	Summary	97
6	Summary	101
	APPENDICES	105
A	PSEUDOPOTENTIAL GENERATION	105
A.1	General procedure	105
A.2	Non-linear Core corrections	106
A.3	Non-local pseudo potential	107
A.4	Kleinman-Bylander non-local pseudo-potential	108
A.5	Tips for pseudo potential generation	108
B	LCAO BASIS SET	109
B.1	Data of benchmark calculation	109
B.2	Basis optimization with constructed cost function	110
	References	117

LIST OF FIGURES

2.1	Schematic diagram of self-consistent loop for DFT calculation.	14
2.2	Schematic diagram of boundary conditions.(a) Dirichlet boundary condition for isolated systems such as free molecules. (b)Periodic boundary condition for periodic systems, the idea of supercell is also shown here using an example of the adsorption of benzene-dithiol(BDT) on Au(111) surface, a system studied in this thesis.	21
2.3	Schematic diagram of a pseudopotential. The wave function (ψ^{AE}) calculated in the Coulomb potential (V^{AE}) of the nucleus (red) is compared to the pseudo wave function (ψ^{PP}) calculated in the pseudopotential (V^{PP}) (blue). Beyond the chosen cutoff radius r_c , both the pseudo wave function and pseudopotentials should be identical to the all-electron ones.	22
3.1	Electrons propagating from the left contact suffer some elastic scattering. T is the transmission probability for the electron to traverse the system. The electrochemical potential in the two electron reservoirs are μ_L and μ_R (assuming $\mu_L > \mu_R$), respectively. L is the length of the scattering region of the device.	29
3.2	Schematic diagram of a two-probe device model with periodic boundary conditions applied in the x-y directions. A molecule with four buffer layers in the central scattering region is sandwiched by two semi-infinite slabs. A bulk boundary condition is also applied at the boundary of the central region in the transport direction (z) for calculating the electronic potential self-consistently. The bulk properties of the leads are calculated with DFT.	37
3.3	Closed contour at finite temperature. For: L ($[\infty + i\Delta, \mu_L - \sigma + i\Delta]$), C, $[-\infty + i0^+, \infty + i0^+]$ and $[\infty + i0^+, \infty + i\Delta]$, the poles (black dots) due to Fermi distribution function are enclosed, they are at $z_n = i(2n + 1)\pi KT$, and n is an integer $0, 1, 2 \dots$. E_B is the bottom of the valence bands.[1]	41
3.4	Schematic diagram of the self-consistent loop in the NEGF-DFT method.	42
4.1	Schematic illustration of a typical TMR device: an insulator or molecular layer sandwiched by two ferromagnetic leads. (a) Parallel (PC) and (c) antiparallel configurations (APC) of spin polarization in the left/right ferromagnetic leads. The corresponding spin-resolved density of the states in ferromagnetic metals are also shown in (b) and (d), in which the blue block represents the minority-spin subband while the red block is the majority-spin subband.	46

- 4.2 Schematic diagram of the device(Ni/octanethiolate/Ni junctions). The scattering central region consists of octanethiolate molecules and four Ni(100) buffer layers connected to each side of the molecules. As shown, the structure is asymmetric. 50
- 4.3 Convergence of Green's function with respect to size of k-mesh. Vertical axis: error $\equiv Tr(|G^r|)/Tr(|G^r(256^2\text{k-mesh})|) - 1$. For 96×96 or greater k-mesh, the result converges. 51
- 4.4 (a)-(d): Zero bias transmission coefficient at E_f in the 2D Brillouin zone. (a) Spin-up channel for PC; (b) spin-down for PC; (c) spin-up for APC; (d) spin-down for APC. Note the different transmission scales indicated by the vertical bar. (e) and (f): Number of incoming channels in the Ni-lead at E_f in 2D BZ. Note spin-up electron is majority carrier but has less DOS at E_f . For this reason the number of conducting channel of spin-up, (e), is less than that of spin-down, (f). 53
- 4.5 (a) k_1 for spin up of PC, $T = 1.1 \times 10^{-3}$ (b) k_2 for spin up of PC, $T = 1.02 \times 10^{-4}$ (c) k_1 for spin down of PC, $T = 8.7 \times 10^{-3}$ (d) k_2 for spin down of PC, $T = 6.3 \times 10^{-4}$ (e) k_1 for spin up of APC, $T = 3.8 \times 10^{-3}$ (f) k_2 for spin up of APC, $T = 2.5 \times 10^{-4}$ (g) k_1 for spin down of APC, $T = 1.2 \times 10^{-3}$ (h) k_2 for spin down of APC, $T = 1.9 \times 10^{-4}$ 55
- 4.6 I-V curves (right axis) and voltage dependence of TMR (left axis). The solid line with diamond (red) and solid-dot (green) are I-V curves for PC and APC. The TMR-V curve (blue line with solid-star) peaks at -20mV with 33% and decays to zero at -200mV and $+120\text{mV}$ 58
- 4.7 The four panels are total transmission $T(E)$ versus energy E for PC (solid blue line) and APC (dashed red) for four different V_b . The difference of PC and APC transmission within the energy window (marked by two dotted vertical lines) reduces for increasing $|V_b|$. Inset in (b): DOS of the Ni leads. 60
- 4.8 The bias-dependent magnetic moment(= $Charge_{\uparrow} - Charge_{\downarrow}$) in sulphur atom of Ni/alkanethiolate/Ni junction for parallel configuration. It shows the proximity effect to the magnetic leads. 61
- 5.1 Top view of the configuration of BDT adsorption to the Au(111) surface. (a) BDT attaches to the surface via the Au adatom. (b) BDT attaches to the surface directly while a Au adatom is also on the surface but sitting aside. 71
- 5.2 Top views of examples for (a) parallel and (b) perpendicular configurations. (c) Four positions of H have been considered for each configuration at several orientations: (A) is for non-dissociated H; (B,C,D) are for dissociated H which attaches to the (B) ad-atom, (C) the surface, or (D) escapes into vacuum forming an H_2 molecule. 72

- 5.3 Fully relaxed configurations for H-non-dissociative junctions: (a) at $L = 13.0 \text{ \AA}$, in which $L_L = 6.846 \text{ \AA} \approx L_R = 6.849 \text{ \AA}$, very close to the D value of an adatom on a bare surface; (b) a surface that an adatom attaches to a bare Au(111) surface, where $D = 6.846 \text{ \AA}$; (c) the junction is at its equilibrium, when $L = 13.8 \text{ \AA}$, in which $L_L = 6.935 \text{ \AA} \approx L_R = 6.933 \text{ \AA}$; (d) the junction starts to break at $L = 15.7 \text{ \AA}$, $L_L = 7.101 \text{ \AA}$, $L_R = 7.052 \text{ \AA}$ 75
- 5.4 Calculated (red dots) and fitted (black lines) data for H-non-dissociative junctions of: (a) total energies of the junction with different lengths, the cross indicates the equilibrium position; (b) derived force from (a) according to equation $F_{\text{Junction}} = dE/dL \approx \Delta E/\Delta L$; (c) calculated force (by the second method) which is acted on the adatom at non-equilibrium positions in the transport direction, the largest likely D value obtained from the H-non-dissociative junction elongation is marked by a plus sign; that from the H-dissociative junction elongation is marked by a cross sign. 78
- 5.5 Calculated (red dots) and fitted (black lines) data for H-dissociative(HD) junctions of: (a) total energies of the junction with different lengths, the cross indicates the equilibrium position; (b) derived total energy (presenting force) according to equation $F_{\text{Junction}} = dE/dL \approx \Delta E/\Delta L$; 79
- 5.6 The molecule NH_2 -benzene-SH attaches to the Au(111) surface via (a) $-\text{NH}_2$ group (b) $-\text{SH}$ group (c) $-\text{S}$ group, the hydrogen atom in $-\text{SH}$ group is considered to be dissociated via the adsorption. 81
- 5.7 Upper panels are for H-dissociative junctions: (a) BDT linked to Au(111) via ad-atoms; (b) BDT linked by Au chains of various lengths. Lower panels are for H-non-dissociative junctions: (c) BDT linked by ad-atoms; (d) as as (c) but with mechanical stretching of the junction. 84
- 5.8 Transmission of H-dissociative (solid blue) and H-non-dissociative (dashed red) models versus energy without junction stretching. The cross denotes the experimental value $0.011G_o$ [2] . Inset: conductance(G_o) versus junction length(\AA) under mechanical stretching (Fig. 5.7b) for H-non-dissociative model. 85
- 5.9 Scattering states of: (a) H-dissociative; (b) H-non-dissociative models. Insets are the HOMO and LUMO of the corresponding molecule 1,4-benzenedithiolate and 1,4-benzenedithiol. 86
- 5.10 The conductance of Au/BDT/Au junction with interface charging. The black-solid line with circles is obtained with negative effective charges applied to the S atom(Case-1). The blue-solid line with triangles is obtained with positive effective charges applied to the hydrogen atom(Case-2). The green-horizontal line corresponds to conductance of the HND-model; the red-horizontal line corresponds to conductance of the HD-model. 89

-
- 5.11 The transmission and projected density of states (PDOS) of Au/BDT/Au with the representative effective charge for both Case-1 (HD model with negative effective charge(EC)=-0.4e,-0.75e in S bond) and Case-2(HND model with positive effective charge(EC)=0.4e,0.8e in H atom of -SH bond). (a)Transmission of Case-1; (b) PDOS of Case-1; (c) Transmission of Case-2; (d) PDOS of Case-2. 89
- 5.12 The molecular junctions calculated in this Section. (a) Au/benzene-dithiol(BDT)/Au, (b) Au/1,4-benzene-diamine(BDA)/Au (c) Au/amine-benzene-thiol(ABT)/Au (d) Au/amine-benzene-thiolate/Au (e) Au/thiol-benzene-thiolate/Au (f) Au/1,4-benzene-dithiolate. 93
- 5.13 The equilibrium conductance of molecular junctions is calculated by varying the length of the junctions. The blue-circle line is for Au/benzene-dithiol/Au junctions, marked as “BDT”; the red-cross line is for Au/benzene-diamine/Au junctions, marked as “BDA”; the green-plus line is for Au/amine-benzene-thiol/Au junctions, marked as “ABT”; the yellow-left-triangle line is for Au/amine-benzene-thiolate/Au junctions, marked as “NH2-S”; the violet-right-triangle line is for Au/thiol-benzene-thiolate/Au junctions, marked as “SH-S”; and the black-up-triangle line is for Au/benzene-dithiolate/Au junctions, marked as “S-S/10” since the value of conductance is divided by a factor of 10 in order to make the data compatible to the others in the same figure. 97
- B.1 The calculated band structures of Silicon FCC crystal with different sets of SZP basis obtained in the example of the present appendix. (a) Basis parameters generated by a reasonable initial guess. (b) Starting from the initial guess in (a), optimized against total energy. (c) Starting from the initial guess in (a), optimized against band gap. . . 114

LIST OF TABLES

4.1	Values of partial transmission P_{AB} in Γ -point from left to right lead. First column indicates for partial wave labels of left lead (incoming), first row is for right lead (out-going). Arrows indicate spin channel. Some values are much larger than others, indicating those scattering channels are dominating.	56
5.1	Experimental measurements of Au/BDT/Au junction.	68
5.2	Theoretical calculations of the conductance Au/BDT/Au/ junctions.	69
5.3	The difference of total energies (units eV) compared to the the most stable structure (the parallel 0^0) for typical configurations of Au/BDT interface. For all situations, the H-non-dissociative structures have lower energies.	73
5.4	Changes of L_L , L_R , and Au-SH bond lengths at the left (Au-S(L)) and right (Au-S(R)) leads in the HND-model. All values are in Angstrom. Here L , L_L , L_R are defined in Fig 5.3. L is defined by the gap between the surfaces of the left and right leads at their initial configurations. L_L/L_R are defined by the distance of left/right adatom to the the third layer of the left/right Au surface.	77
5.5	The total energies E_{total} of ABT adsorption and the bond energies E_B . Au-NH ₂ is corresponding to the case that ABT attaches to the Au surface via NH ₂ group, Au-SH and Au-S are corresponding to the cases of ABT attaches to the Au surface via -SH group but with hydrogen non-dissociated or hydrogen dissociated model. The angles 0^0 and 60^0 are used to cover the configurations in case of rotational symmetry of the system. Energies are in unit of eV.	82
5.6	Total energies of the scattering region and the corresponding conductance are given for various length of the transport junctions. (a)Au/benzene-dithiol(BDT)/Au, (b)Au/benzene-diamine(BDA)/Au and (c) Au/amine-benzene-thiol(ABT)/Au. L is defined as the distance between the two Au lead surfaces in the junction, the same definition as Tab. 5.4 and Fig.5.3 in Section 5.2.2. The conductance is calculated using the standard NEGF-DFT method. *The equilibrium positions are found at (a) $L = 13.8\text{\AA}$ (b) $L = 13.0\text{\AA}$ and (c) $L = 13.4\text{\AA}$. **The break-down positions are found at(a) $L = 15.7\text{\AA}$ (b) $L = 14.7\text{\AA}$ and (c) $L = 15.0\text{\AA}$	98

- 5.7 This table is the continuation of Tab.5.6. The total energies of the scattering region and the corresponding conductance are given for various length of the *(d)Au/amine-benzene-thiolate/Au*, *(e)Au/thiol-benzene-thiolate/Au* and *(f) Au/benzene-dithiolate/Au* junctions. L is defined as the distance between the two Au slabs in the junctions, the same definition as Tab. 5.4 and Fig.5.3 in Section 5.2.2. For different L , the conductance of these molecular junctions is calculated using standard NEGF-DFT method. *The equilibrium positions are found at (d) $L = 13.2\text{\AA}$ (e) $L = 13.5\text{\AA}$ and (f) $L = 13.6\text{\AA}$. **The break-down positions are found at(d) $L = 14.9\text{\AA}$ (e) $L = 15.5\text{\AA}$ and (f) $L = 16.0\text{\AA}$. 99
- B.1 Lattice constants for elements with FCC, BCC structures are optimized by LDA/PBE functional using the VASP package. The results are compared with the available experimental data in www.webelements.com. 111
- B.2 Lattice constants(a/c) for elements and compounds with HCP structure are optimized by LDA/PBE functionals using the VASP package. The results are compared with the available experimental data in www.webelements.com. 112
- B.3 Lattice constants of various compounds are optimized by LDA/PBE functionals using the VASP package. The results are compared with the available experimental data in www.webelements.com. 113

Abstract

In this thesis, we report theoretical investigations of nonlinear and nonequilibrium quantum electronic transport properties of molecular transport junctions from atomistic first principles. The aim is to seek not only **qualitative** but also **quantitative** understanding of the corresponding experimental data. At present, the challenges to quantitative theoretical work in molecular electronics include two most important questions: (i) what is the proper atomic model for the experimental devices? (ii) how to accurately determine quantum transport properties without any phenomenological parameters? Our research is centered on these questions. We have systematically calculated atomic structures of the molecular transport junctions by performing total energy structural relaxation using density functional theory (DFT). Our quantum transport calculations were carried out by implementing DFT within the framework of Keldysh non-equilibrium Green's functions (NEGF). The calculated data are directly compared with the corresponding experimental measurements. Our general conclusion is that quantitative comparison with experimental data can be made if the device contacts are correctly determined.

We calculated properties of nonequilibrium spin injection from Ni contacts to octane-thiolate films which form a molecular spintronic system. The first principles results allow us to establish a clear physical picture of how spins are injected from the Ni contacts through the Ni-molecule linkage to the molecule, why tunnel magnetoresistance is rapidly reduced by the applied bias in an asymmetric manner, and to what extent *ab initio* transport theory can make quantitative comparisons to the corresponding experimental data. We found that extremely careful sampling of the two-dimensional Brillouin zone of the Ni surface is crucial for accurate results in such a spintronic system.

We investigated the role of contact formation and its resulting structures to quantum transport in several molecular wires and show that interface contacts critically control charge conduction. It was found, for Au/BDT/Au junctions, the H atom in -SH groups energetically prefers to be **non-dissociative** after the contact formation, which was supported by comparison between computed and measured break-down forces and bonding energies. The H-non-dissociated (HND) junctions give equilibrium conductances from $0.054G_0$ (equilibrium structure) to $0.020G_0$ (stretched structure) which is within a factor of 2-5 of the measured data. On the other hand, for all H-

dissociated contact structures - which were the assumed structures in the literature, the conductance is at least more than an order of magnitude larger than the experimental value. The HND-model significantly narrows down the theory/experiment discrepancy. Finally, a by-product of this work is a comprehensive pseudopotential and atomic orbital basis set database that has been carefully calibrated and can be used by the DFT community at large.

Résumé

Cette thèse présentera nos recherches théoriques sur les propriétés quantiques de transport électronique des jonctions de transport moléculaire. Cette analyse a été effectuée à l'aide de méthodes *ab initio* atomiques qui sont valides dans les régimes non-linéaire et hors-équilibre. L'objectif est de rechercher non seulement une compréhension **qualitative** des données expérimentales mais aussi **quantitative**. Les deux questions les plus importantes quant au travail théorique en électronique moléculaire sont: (i) quel est le bon modèle atomique pour simuler les dispositifs expérimentaux? (ii) comment déterminer avec précision les propriétés de transport quantique sans l'utilisation de paramètres phénoménologiques? Nos recherches sont centrées sur ces questions. Nous avons systématiquement calculé les structures atomiques de jonctions moléculaires en effectuant la relaxation structurale dans le cadre de la théorie de la fonctionnelle de la densité (DFT). Les calculs de transport quantique ont été réalisés en combinant la DFT avec les fonctions de Green hors-équilibre de Keldysh (NEGF). Les calculs sont directement comparés aux données expérimentales correspondantes. Notre conclusion générale est qu'un accord quantitatif entre les valeurs théoriques et empiriques est possible si la structure atomique du contact est correctement déterminée.

Nous avons calculé les propriétés hors-équilibre d'injection de spin à travers un film d'octane-thiole en contact avec des électrodes en Ni, formant ainsi un système spintronique moléculaire. Les résultats obtenus par premiers principes nous fournissent une compréhension claire sur la façon dont les spins sont injectés à partir des électrodes en Ni à la molécule par la liaison Ni-molécule. De plus, nous expliquons pourquoi la magnéto-résistance à effet tunnel décroît rapidement avec une augmentation du potentiel électrique, et ce, de manière asymétrique. Finalement, nous démontrons que la théorie *ab initio* du transport électronique est en mesure d'effectuer des comparaisons quantitatives avec les données expérimentales. Nous avons constaté qu'un échantillonnage minutieux de la zone de Brillouin 2D de la surface du Ni est crucial afin d'obtenir des résultats précis dans un tel système spintronique.

Nous avons étudié le rôle de la formation du contact, ainsi que la structure atomique associée sur l'influence du transport quantique dans le cas de plusieurs jonctions moléculaires. Nous démontrons que l'interface reliant les électrodes aux molécules

contrôle très sensiblement la conduction de charge. Il a été trouvé, pour les jonctions Au/BDT/Au, que l'atome d'hydrogène dans les groupes -SH préfère énergétiquement la **non-dissociation** après la formation du contact. En effet, ceci a été corroboré par la comparaison entre les données calculées et mesurées des forces de rupture et des énergies de liaison. Les jonctions avec l'hydrogène non-dissocié (HND) donnent des valeurs de conductances à l'équilibre de $0.054G_0$ (structure d'équilibre) à $0.020G_0$ (structure étirée). Ces valeurs sont à l'intérieur d'un facteur de 2-5 aux données expérimentales actuelles. D'autre part, toutes les structures de contact H-dissociées — qui ont été les structures supposées dans la littérature — résultent en des valeurs de conductances calculées au moins un ordre de grandeur plus élevé que les valeurs empiriques. Le modèle HND réduit de manière significative l'écart entre la théorie et les expériences. Pour terminer, une conséquence de ce travail est le regroupement d'une base de données complète incluant des pseudo-potentiels et des orbitales atomiques. Celle-ci a été soigneusement calibrée et est disponible à toute la communauté DFT.

Statement of Originality

In this thesis, we investigated the transport properties of various molecular devices by state-of-the-art first-principles techniques. Specifically, my main contributions to these studies include:

- I developed a number of computational methods and software calculator modules for the NEGF-DFT quantum transport packages `matdcal` (matlab-based Device Calculator) and `nanodcal` (nanoelectronic device calculator), which include basis function optimization, massive adaptive k-sampling, and GGA functionals for nonequilibrium quantum transport.
- I invented and investigated various optimization target functions and used them to develop a comprehensive optimized pseudo-potential and atomic basis sets across the entire periodic table (over 70 elements). This database allows us to achieve very accurate LCAO DFT calculations that are comparable to large basis set methods such as planewaves. This database is now the best and most complete in the literature regarding LCAO DFT computation.
- I investigated spin injection in Ni/octane-thiolate/Ni molecular spintronic system. In this work, I carried out the entire calculation, solved all the technical difficulties, and discovered the microscopic physics that control the spin injection.
- I discovered the hydrogen non-dissociative (HND) Au-SH bonding structure through systematic investigations on total-energy, junction break-down force and bond energies. The HND-model drastically narrowed down the discrepancy of theory-experiment conductance in Au/BDT/Au junctions by at least an order of magnitude. It also serves a further confirmation on the validity of the NEGF-DFT formalism for molecular electronics.
- I implemented the ionic pseudo-potential and its associated basis sets for calculating charged systems. To the best of my knowledge, the problem of interface charging was investigated for the first time in the literature for quantum transport from atomic first principles.

- I developed a comprehensive method to estimate the transport junction mechanical break-down force. Two models were developed and investigated that provide the range of the forces.
- I developed a standard procedure that allows systematic calculations of electronic transport properties in molecular junctions. Using this procedure, I investigated many molecular junctions which allowed to abstract a conceptual quantity named “electronic stability” for molecular junctions as a measure of metal-molecule bonding for charge transport.

Acknowledgments

First and foremost, I would like to pass my appreciation to Prof. Hong Guo. He is far more than the best supervisor that I was expecting to have. In addition to providing great guides in scientific researches, he has the magic power to make me confident and enlighten my inspirations while facing difficulties. Also, he selflessly taught me the rich experience of being a scientist, which will be beneficial throughout my future career. It is my great honor to have the opportunity of working in his group in the last five years.

Next, I would like to thank all the group members. It is the wonderful experience to work with your guys. In particular, I would like to thank Dr. Wei Ji. and Dr. Eric Zhu. It is the fruitful discussions with them that finally produced the work in this thesis and many insightful collaborations in the future. Also, I want to thank Dr. Vladimir Timochevskii, I learned a lot of experience about pseudopotential and basis generation from him. And I thank Dr. Lei liu and Dr. Yibin Hu for their instructive discussions about the codes of MATDCAL and NanoDCAL. I also have many interesting discussions with Tao, Youqi, Dr. Ferdows Zahid, Jesse and Manny. Thank all of you. Specially, I should thank Jesse again for his great help of French.

Last but not the least, I wish to thank my parents and my sister. Every step of my life is accompanied by their love and support. Without them, none of these would have been possible. Here I wish to pass my last thank to my destined love: huanhuan, for her great support. She is the most special one in my “thank you ” list, because the thesis is written for her.

Abbreviations and Symbols

MCBJ: Mechanically Controllable Break Junction.

STM: Scanning Tunneling Microscopy.

AFM: Atomic force microscopy.

BEM: Ballistic electron microscopy.

IETS: Inelastic electron tunnelling spectroscopy.

DFT: Density Functional Theory.

SCF: Self-consistent field.

LDA: Local-Density Approximation.

LSDA: Local-Spin-Density Approximation.

GGA: Generalized Gradient Approximation.

SIC: Self-interaction Correction.

BZ: Brillouin Zone.

DOS: Density of States.

PDOS: Projected Density of States.

STO: Slater-Type Orbitals.

GTO: Gaussian-Type Orbitals.

LCAO: Linear Combination of Atomic Orbital.

PW: Plane Wave.

LAPW: Linear Augmented Plane Wave

HOMO: Highest Occupied Molecular Orbital.

LUMO: Lowest Unoccupied Molecular Orbital.

NEGF: Non-Equilibrium Green's Function.

TMR: Tunnel Magnetoresistance.

BDT: benzene-dithiol

HND: Hydrogen-non-dissociated

HD: Hydrogen-dissociated

SAM: self-assembled monolayer

EBL: electron-beam lithography

EM : electromigration

BDA: benzene-diamine

ABT: amine-benzene-thiol

EC: effective charge

1

Introduction

Fifty years ago, Nobel laureate Prof. Richard P. Feynman gave a visionary talk entitled “There’s Plenty of Room at the Bottom”[3]. He foresaw there to be an “... invitation to enter a new field of physics”. Today, this new field is known as nano-science. Indeed, fifty years later, tremendous research and development in nano-science are making some of his ideas a reality. In physics, one can very precisely predict the dynamics of a small number of particles such as the motion of electrons in a hydrogen atom ; or understand the macroscopic assembly of $\sim 10^{23}$ particles by statistical mechanics. Our ability to make quantitative predictions for systems not too small yet not macroscopic,i.e., systems in the nano- and mesoscopic scales, is actually rather limited. In a way, Feynman’s vision was related to the complex dynamics of charge carries in nanoscale structures.

This thesis is concerned with theoretical efforts of electronic transport through nanoscale contacts. Particularly, I shall focus on the metal-molecule contacts. Our work strongly suggested that these contacts play crucial and, in some cases, dominating roles for the interesting endeavor of molecular electronics. Molecular electronics envisions the use of individual molecules for electronics applications[4]. Understanding molecular electronics is challenging because it requires a combined effort from physics, chemistry, materials science and electrical engineering. Charge and spin quantum transport in molecular electronics is strongly coupled to the microscopic physics and chemistry of the molecules. From a practical point of view, even though molecular electronics may not be able to replace solid-state switching devices such as the field effect transistors in computer chips, molecular electronics can be quite

useful for applications in ultra-sensitive bio-sensors[5], molecular thin film photovoltaic devices[6], smart materials[7], and molecule-solid hybrid devices[8]. As many new artificial molecules are being synthesized, exploiting molecules for electronics has become a very active field of interdisciplinary research.

Research and developments in molecular electronics are also important and useful for investigating conventional semiconductor electronics. In 2010, the channel feature in commercially available transistors has reached 32 nm which is about the length of 120 metal atoms lined in a row. At such an ultra small length scale, the semiconductor material can no longer be considered as continuous but must be treated as discrete atomistic entities. Quantum transport theory for such atomic sized materials is essentially the same, apart from some chemical issues, as that for molecular electronics. In fact, the theoretical formalism and computational method we use and extend in this thesis can be equally well applied to both molecular electronics and semiconductor nanoelectronics. Furthermore, in addition to its electrical properties, molecular electronics also have rich properties in many other aspects including properties suitable for optoelectronics, spintronics, thermoelectricity, electro-mechanics and molecular recognition[9]. It is these versatile and interesting properties that have drawn a broad interest in the past decade from physics, chemistry, materials science and electrical engineering[10, 11, 12, 13, 14, 15, 16, 17, 18, 19, 20, 21, 22].

The concept of molecular electronics was first introduced in 1974 by Mark Ratner and Ari Aviram where they theoretically analyzed the properties of a single molecule electric rectifier[4]. However, experimental measurements of the transport characteristics of individual molecules require the development of techniques that can control molecular-scale electrical contacts. This turned out to be extremely difficult to achieve even today. In 1997, Mark Reed and co-workers published[23], to the best of my knowledge, the first experimental conductance measurement of a single molecule using the method of mechanically controllable break junction (MCBJ). Since then, molecular electronics has progressed rapidly as an important branch of nano-electronic device physics, accompanied by great developments of structural and spectroscopic

characterization techniques. Several important experimental tools[9] have been applied to molecular electronics systems such as:

- Structural measurement tools:
 - scanning tunneling microscopy (STM);
 - Atomic force microscopy (AFM);
 - Ballistic electron microscopy (BEM).

- Spectroscopy measurement tools:
 - Surface spectroscopy techniques including photoemission and inelastic electron tunnelling spectroscopy (IETS);
 - Optical spectroscopy including infrared and Raman.

- Transport measurement tools:
 - Mechanically controllable break junction;
 - STM;
 - Conducting AFM;
 - Nanopore[24];
 - Solid state lithography[25].

The multitude of experimental tools have drastically enhanced our current understanding of structural, electronic and transport properties of molecular electronics.

On the theoretical side, in order to understand the general physics of nanoelectronic devices, one needs to start from a proper modeling of the nanostructures. Due to the lack of atomic details in most (if not all) experiments, a wide range of possible different metal-molecule contact geometries should be examined. In fact, a central issue of molecular electronics has been the structural-transport relationship, namely how do quantum transport of charge and spin relate to the atomic structures. At present, the non-equilibrium Green's Function (NEGF) combined with density

functional theory (DFT) is becoming one of the most popular and effective methods for parameter-free calculations of quantum transport from atomistic point of view. Compared with traditional DFT approaches which are for equilibrium and for finite or periodic structures, NEGF-DFT accounts for the influence of molecule-electrode interactions and externally applied bias by a self-energy correction, thus allowing first principles calculations of open device systems. As summarized by a recent review article[26], for a rather wide selection of molecules, the difference between the measured conductance and parameter-free theoretical calculation based on NEGF-DFT is within a factor of two to five. Even though such a level of theory/experiment consistency appears to be less impressive than those achieved in spectroscopy (i.e. band structures of solids), it represents great progress in both theory and experiment over the situation just ten years ago, where adjustable parameters were needed to simulate the experiments, and different experimental labs often reported drastically different results for the same system. Considering the uncertainties in the experimental atomic structures, measurements and uncontrollable fluctuations, and the inevitable approximations in the NEGF-DFT theory, at present the “norm” of quantitative consistency between parameter-free theoretical predictions and measurements is within a range of two to five, even though for many situations the agreement is much better, to within a few percent. However, there have been two exceptions where the theory and experimental results differ by a much larger factor than the norm[26]. One system is the benzene-dithiol (BDT) molecule contacted by gold leads, where the theoretical conductance is larger than the measured one by a factor of at least 50. The other system is the Au/phenylene ethynylene/Au molecular junction, which gives the theory-experiment difference with a factor of about 14. If we go further into these details of the molecules, we find that these theoretically “unsuccessful” systems purely consist of π -bonds. Indeed, all the σ -bond dominated molecular wires gave much more satisfactory comparisons to experimental data[26, 27].

Clearly, difference with experimental data by a factor of 50 or by a factor of 2, requires very different theoretical improvements. The former clearly calls for a drasti-

cally different formalism than the present NEGF-DFT, while the latter can probably be resolved by a more careful examination of device details and physical understanding. These issues present an important question in molecular electronics theory, namely to what extent the present level of the NEGF-DFT formalism can provide reliable quantitative predictions in molecular electronics and if higher-level correlations should be included into the NEGF-DFT. In particular, the Au/BDT/Au device is a serious challenge to the NEGF-DFT formalism of ab initio quantum transport theory.

It is the aim of this thesis to present the current status of theoretical calculations based on the NEGF-DFT formalism for some typical metal-molecule systems. Our work clearly shows that with correctly determined atomic structures, the calculated conductances are actually comparable to the experimental measurements within the same order of magnitude. Each system adopted in this thesis is taken as an example of a prototype in molecular electronics. With the most careful analysis, our results should provide benchmarks that clarify the present status of a first principles theory of quantum transport in molecular systems.

Each chapter of this thesis covers a representative topic which can be exploited and extended to more complicated molecular electronic devices. The outline is as follows:

Chapter 2 presents an overview of electronic structure calculations. Density functional theory (DFT) is discussed in detail including aspects of practical numerical implementations. Comparisons with other methods are also provided.

Chapter 3 introduces the theoretical framework of the Keldysh non-equilibrium Green's functions (NEGF). The focus is on combining the NEGF with a self-consistent field (SCF) theory. At equilibrium SCF can be described solely by DFT. At nonequilibrium, SCF differs from the ground state DFT in a crucial aspect, namely it is the nonequilibrium density matrix calculated from NEGF that enters the SCF, instead of the equilibrium density matrix entering the conventional DFT. We further discuss phase-coherent quantum transport within NEGF.

Chapter 4 presents an investigation of spin-polarized quantum transport in the molecular tunnel junction Ni/octanethiolate/Ni. We review the conventional magnetic tunnel junction theory. The behavior of spin-transfer in the molecular junction is investigated from first principles and is satisfactory in comparison to the experimental measurements. Results for this work have been published in Ref.[28] and resulted in another manuscript[29].

Chapter 5 reviews the long-time controversial status of the Au/BDT/Au molecular junction in both experimental and theoretical sides. More importantly, through a set of DFT based total energy calculations, we discovered a new possible Au-thiol bonding structure in the device contact formation. Using this newly-discovered atomic structure, our results on conductance significantly narrowed the gap between theoretical calculation and experimental measurement. Based on this work, a series of molecular junctions with different metal-molecule contacts are carefully investigated, which can be taken as an additional proof for the consistency of our comparison between experiments and our theoretical results. The contents of this Chapter are summarized in three manuscripts[30, 31, 32].

Appendixes A and B provide discussions on the generation of a database for pseudopotential and LCAO basis sets, respectively. The technical details for constructing and optimizing the pseudopotential and basis sets are introduced as well.

During the course of this thesis research, I have also participated in several applied projects using the tools discussed here. These resulted in three publications not included in this thesis, but can be found in Refs.[33, 34, 35].

Theory of Electronic Structure

Electronic structure calculation is a large subject, covering properties of electrons in atoms, molecules and condensed-phase materials using quantum mechanical theories. Physical systems can be considered as a collection of heavy positively charged nuclei and light, negatively charged electrons. For a system of N nuclei each having Z electrons, one is dealing with a system of $N + ZN$ interacting particles, which is a many-body problem. Mathematically, the many-body problem is described by the following Hamiltonian operator¹:

$$\hat{H} = -\frac{1}{2} \sum_i \frac{\nabla_{\vec{R}_i}^2}{M_i} - \frac{1}{2} \sum_i \nabla_{\vec{r}_i}^2 - \sum_{i,j} \frac{Z_i}{|\vec{R}_i - \vec{r}_j|} + \frac{1}{2} \sum_{i \neq j} \frac{1}{|\vec{r}_i - \vec{r}_j|} + \frac{1}{2} \sum_{i \neq j} \frac{Z_i Z_j}{|\vec{R}_i - \vec{R}_j|}. \quad (2.1)$$

Here M_i is the mass of a nucleus at position \vec{R}_i ; $m_e (=1)$ is the mass of an electron at position \vec{r}_i , and Z_i, j is the atomic number of the atom i, j . The first and second terms are the kinetic energy operators for the nuclei and electrons, respectively. The last three terms are the Coulomb interactions between electrons and nuclei, between electrons, and between nuclei, respectively. Due to the complexity of the many-body correlations, in general an exact solution of the above Hamiltonian operator is impossible. Therefore approximations are necessary in order to make progress in electronic structure calculations.

2.1 *The Born-Oppenheimer approximation*

To solve the many-body problem of Eq.(2.1) for condensed phase materials, one typically applies the Born-Oppenheimer approximation which separates the motion of the

¹Throughout this thesis atomic units are used, namely $e^2 = \hbar = m_e = 1$

nuclei from that of the electrons. This is possible because the nuclei are much heavier than the electrons and the inertia of electrons is negligible in comparison to the that of the nuclei. Therefore, when considering electrons one can freeze the motion of nuclei and the potential due to nuclei is treated as an external potential. Physically, the Born-Oppenheimer approximation assumes the electrons to follow the motion of nuclei instantaneously.

With the Born-Oppenheimer approximation, the first kinetic energy term, for the nuclei in Eq.(2.1), vanishes since all the nuclei are now fixed in position. The last term in Eq.(2.1) is reduced to a constant. The Hamiltonian (2.1) is now reduced to three major terms: the kinetic energy of the electron gas (\hat{T}), the potential energy (\hat{V}) due to Coulomb interactions among electrons and the external potential energy (\hat{V}_{ext}) contributed by the nuclei,

$$\hat{H} = \hat{T} + \hat{V} + \hat{V}_{ext} . \quad (2.2)$$

It is worth noting that in Eq.(2.2), the kinetic energy \hat{T} and electron-electron interaction \hat{V} are independent of the nuclei. All the additional information related to the system such as the position of the nuclei and the interactions from nuclei is included in \hat{V}_{ext} . The Born-Oppenheimer approximation turns the many-body electrons/nuclei system into a many-electron problem.

2.2 Density functional theory

Although the Born-Oppenheimer approximation has remarkably simplified the many-body problem, the resulting Hamiltonian, Eq. (2.2), is still too difficult to solve due to the complicated electron-electron interactions. Next level approximations are necessary. In early developments of electronic structure theory, the Hartree-Fock(HF) approximation was widely applied in solving the electronic Schrödinger equation of atoms, molecules and solids. The HF approximation neglects electron correlation and does not provide accurate results for many condensed phase materials.

A better approximation is the density functional theory (DFT) which plays a key role in the work presented in this thesis. In the following I will first present the

Hohenberg and Kohn(HK) theorems which establish the core idea of DFT. I will introduce the Kohn-Sham formalism followed by a discussion of exchange-correlation functionals. Finally I will introduce some details about the numerical implementations of DFT methods. Particularly, the choice of boundary conditions, the theory of pseudopotentials and the issues of basis sets are important factors in numerical calculations of electronic structure within DFT, which will be discussed carefully.

2.2.1 The Hohenberg-Kohn(HK) theorem

In 1964, Hohenberg and Kohn proved two important theorems[36] which formally established the theoretical framework of DFT. Their first theorem stated that the ground-state charge density $\rho(\vec{r})$ of a many-body system uniquely determines the external potential. This mapping relationship $\{V_{ext}(\vec{r})\} \leftrightarrow \rho(\vec{r})$ is one-to-one and invertible. An immediate consequence is that any observable physical property (\hat{O}) is a unique functional of the ground-state charge density:

$$\langle \psi | \hat{O} | \psi \rangle = O[\rho] . \quad (2.3)$$

Suppose \hat{O} to be the Hamiltonian \hat{H} of Eq.(2.2), we have the ground-state total energy functional:

$$E[\rho] = \langle \psi | \hat{T} + \hat{V} | \psi \rangle + \langle \psi | \hat{V}_{ext} | \psi \rangle = F_{HK}[\rho] + \int \rho(\vec{r}) V_{ext}(\vec{r}) d\vec{r} . \quad (2.4)$$

Here the Hohenberg-Kohn density functional $F_{HK}[\rho]$ is universal for any many-electron system. $E[\rho]$ reaches a minimal value of ground-state total energy for the ground-state charge density ρ corresponding to V_{ext} . Formula 2.4 is usually taken as the second Hohenberg-Kohn theorem. We shall not repeat the proof of the HK theorems here since they have been thoroughly scrutinized for more than four decades.

Going back to quantum mechanics to solve a many-body Schrödinger equation, the usual procedure is as follows:

$$V(\vec{r}) \longrightarrow \psi(\vec{r}_1, \vec{r}_2, \dots, \vec{r}_N) \longrightarrow \langle \psi | \hat{O} | \psi \rangle . \quad (2.5)$$

Namely, one first specifies the system by a potential $V(\vec{r})$, solves the many-body Schrödinger equation to evaluate the many-body wave function $\psi(\vec{r}_1, \vec{r}_2, \dots, \vec{r}_N)$, then

calculates the expectation value of physical properties using the many-body ψ . For example, charge density is obtained as

$$\rho(\vec{r}) = N \int d^3r_2 \int d^3r_3 \cdots \int d^3r_N \psi^*(\vec{r}, \vec{r}_2, \cdots, \vec{r}_N) \psi(\vec{r}, \vec{r}_2, \cdots, \vec{r}_N). \quad (2.6)$$

The above calculation procedure, based on the many-body wave function $\psi(\vec{r}_1, \vec{r}_2, \cdots, \vec{r}_N)$, appears to hint that ψ contains more information than the charge density ρ , namely one obtains ρ from the many-body ψ . However, the HK theorems tell us that the ground-state wave function and the charge density are one-to-one equivalent. Hence, only having the ground state charge density of the system, all the observable physical quantities can be obtained directly. For example, they can be evaluated as the functionals of the density - shown in formula 2.4. From the HK theorem point of view, only ρ is needed to obtain the ground state electronic structure which provides an idea to bypass the calculation of many-body wave functions.

It's important to note that the $F_{HK}[\rho]$ is a **universal** functional of ρ . The universality of $F_{HK}[\rho]$ means that it is independent of the external potential V_{ext} of the system since it does not contain any information about the nuclei and their positions. Although we don't know the explicit expression of $F_{HK}[\rho]$, in principle such an expression exists and can be used to calculate atom, molecule or solids. Numerically, further approximations are needed since $F_{HK}[\rho]$ is just a functional of a 3-dimensional real space density. If we knew ρ , the contribution to the total energy from the external potential is easily calculable since $\int \rho(\vec{r}) V_{ext}(\vec{r}) d\vec{r}$ can be explicitly evaluated. Thus, the total energy is in principle can be solved as a functional of the charge density ρ .

Assuming we have found $F_{HK}[\rho]$, it is possible to numerically determine the ground-state charge density using the Rayleigh-Ritz variational principle. The density which can minimize the energy functional $E[\rho]$ in the second HK theorem, Eq.(2.4), is that of the ground-state corresponding to the external potential $V_{ext}(\vec{r})$.

2.2.2 The Kohn-Sham equation

The very important Kohn-Sham equation[37] provides a numerical procedure that makes DFT applicable. Instead of searching for an explicit and exact many-body

energy functional, Kohn and Sham introduced[37] a special set of non-interacting quasi-particle orbitals $\phi_i(\vec{r})$. The density $\rho(\vec{r})$ is then constructed from $\phi_i(\vec{r})$:

$$\begin{aligned}\rho(\vec{r}) &= \sum_{i=1}^N f_i |\phi_i(\vec{r})|^2 \\ \langle \phi_i(\vec{r})^* | \phi_j(\vec{r}) \rangle &= \delta_{ij} ,\end{aligned}\tag{2.7}$$

where f_i is the Fermi-Dirac distribution function applied for the energy level of orbital i . Compared with the many-body expression Eq.(2.6), formally Eq.(2.7) is much easier to calculate. Importantly, by the HK-theorems, the ρ from both Eq.(2.6) and Eq.(2.7) give the same physics - as long as Eq.(2.7) can be calculated with the full exchange-correlation functional.

As a consequence of Eq.(2.7), the N-body problem in DFT formally becomes solving N single-particle problems (for the N ϕ_i orbitals) where the many-body effects are taken into account by an exchange-correlation functional. The formal manipulation goes as follows. Let's start by rewriting the $F_{HK}[\rho]$ functional in a different way. We will explain the physical quantities introduced through the derivation,

$$\begin{aligned}F_{HK}[\rho] &= \langle \psi | \hat{T} + \hat{V} | \psi \rangle = T + V \\ &= T_0 + V + V_c , \text{ Define } V_c = T - T_0 \\ &= T_0 + V_H + V_c + V_x , \text{ Define } V_x = V - V_H \\ &= T_0 + V_H + V_{xc} , \text{ Define } V_{xc} = V_x + V_c .\end{aligned}\tag{2.8}$$

In the above expression, we defined several quantities. For kinetic energy, T is the exact many-body kinetic energy functional and T_0 is defined as the kinetic energy functional for a non-interacting electron gas. Usually, T_0 cannot be expressed explicitly and exactly as a functional of ρ , but it can be easily written in terms of the single particle orbitals $\phi_i(\vec{r})$ (defined in formula 2.7) of a non-interacting system with density $\rho(\vec{r})$, as

$$T_0[\rho(\vec{r})] = -\frac{1}{2} \sum_{i=1}^N \int d^3r \phi_i(\vec{r})^* \nabla_i^2 \phi_i(\vec{r}) .\tag{2.9}$$

The difference between T and T_0 is put into a correlation potential functional V_c . For the electron-electron interactions, V is the exact many-body potential while V_H is the

Hartree potential. The difference between V and V_H is put into an exchange potential V_x . In fact, all these differences are collectively called the exchange-correlation potential functional V_{xc} . V_{xc} accounts for all the interactions which are difficult to calculate exactly in the many-body system. As a specific and important topic, we will discuss how to calculate the exchange-correlation functional in the next section. Before that, assume we have somehow obtained V_{xc} . Recall the second HK theorem, i.e. Eq.(2.4), the energy functional $E[\rho]$ can also be written in a new form based on the F_{HK} as follows:

$$\begin{aligned} E[\rho] &= T_0[\rho] + V_H[\rho] + V_{xc}[\rho] + V_{ext}[\rho] \\ &= T_0[\rho] + \frac{1}{2} \int \frac{\rho(\vec{r})\rho(\vec{r}')}{|\vec{r} - \vec{r}'|} d\vec{r}d\vec{r}' + V_{xc}[\rho] + \int \rho(\vec{r})v_{ext}(\vec{r})d\vec{r} . \end{aligned} \quad (2.10)$$

So far, the mathematical manipulations are exact without introducing any approximation. What we have done is to transform an interacting many-body energy functional to a form of non-interacting electron gas plus an unknown exchange-correlation term. Effectively, we can consider that the system is a non-interacting electron gas with two external potentials: V_{xc} contributed by the exchange-correlation interaction and V_{ext} contributed by the nuclei. To find the ground state, all we need to do is to minimize $E[\rho]$ with respect to ρ . Kohn and Sham suggested a scheme for the minimization[37], namely:

$$\begin{aligned} 0 &= \frac{\delta E[\rho]}{\delta \rho(\vec{r})} = \frac{\delta T_0[\rho]}{\delta \rho(\vec{r})} + \frac{\delta V_H[\rho]}{\delta \rho(\vec{r})} + \frac{\delta V_{xc}[\rho]}{\delta \rho(\vec{r})} + \frac{\delta V_{ext}[\rho]}{\delta \rho(\vec{r})} \\ &= \frac{\delta T_0[\rho]}{\delta \rho(\vec{r})} + v_H + v_{xc} + v_{ext} . \end{aligned} \quad (2.11)$$

As a consequence of Eq.(2.10), the term of $\delta V_H[\rho]/\delta \rho(\vec{r})$ simply yields the Hartree potential $\int d\vec{r}'\rho(\vec{r}')/|\vec{r} - \vec{r}'|$. The term $\delta V_{ext}[\rho]/\delta \rho(\vec{r})$ represents the external potential $v_{ext}(\vec{r})$ from the nuclei. Only for $\delta V_{xc}[\rho]/\delta \rho(\vec{r})$, there is no explicit expression yet. Once the functional form of V_{xc} is known, we can then write the term as $v_{xc} \equiv \delta V_{xc}[\rho]/\delta \rho(\vec{r})$.

To simplify the problem, let us consider a system of noninteracting particles moving

in the potential $v_0(\vec{r})$. For this problem, the minimization condition gives:

$$0 = \frac{\delta E_0[\rho]}{\delta \rho(\vec{r})} = \frac{\delta T_0[\rho]}{\delta \rho(\vec{r})} + \frac{\delta V_0[\rho]}{\delta \rho(\vec{r})} = \frac{\delta T_0[\rho]}{\delta \rho(\vec{r})} + v_0(\vec{r}) . \quad (2.12)$$

The non-interacting Hamiltonian can be written as:

$$\hat{H}_0 = \hat{T}_0 + \hat{V}_0 = -\frac{1}{2} \nabla_i^2 + v_0 . \quad (2.13)$$

As an analogy, the Kohn-Sham Hamiltonian will be:

$$\hat{H}_{KS} = \hat{T}_0 + \hat{V}_{eff} = -\frac{1}{2} \nabla_i^2 + v_{eff} , \quad (2.14)$$

here we defined an effective potential \hat{V}_{eff} as:

$$\hat{V}_{eff} = \hat{V}_H + \hat{V}_{xc} + \hat{V}_{ext} = \int \frac{\rho(\vec{r}')}{|\vec{r} - \vec{r}'|} d\vec{r}' + v_{xc} + v_{ext} , \quad (2.15)$$

where the exchange-correlation potential v_{xc} is given by the functional derivative

$$v_{xc} = \frac{\delta V_{xc}[\rho]}{\delta \rho} . \quad (2.16)$$

Consequently, one can calculate the density of the many-body interacting system by solving the equations of a single particle noninteracting system in an effective potential $v_{eff}(\vec{r})$. In particular, the Schrödinger equation of this auxiliary system is:

$$\hat{H}_{KS}\phi_i = \left(-\frac{1}{2} \nabla_i^2 + v_{eff} \right) \phi_i = \epsilon_i \phi_i . \quad (2.17)$$

This is the well known Kohn-Sham (KS) equation. With it, the solution to a complicated many-body problem is switched to solving an effective non-interacting single particle Schrödinger equation. One should note that the single-particle wave functions $\phi_i(\vec{r})$ are not the real wave functions of electrons. They are just introduced by a mathematical transformation, and should be taken as some quasi-particle wave function without a clear physical meaning. Similarly, the physical meaning of the eigenvalues ϵ_i corresponding to the wave function ϕ_i is also unclear. They are just the eigen-energies of the quasi-particles. However, as shown in Eq.(2.7), the overall density of these quasi-particles are equivalent to the real many-body electron density. This fact suffices for DFT to obtain physically meaningful ground state results.

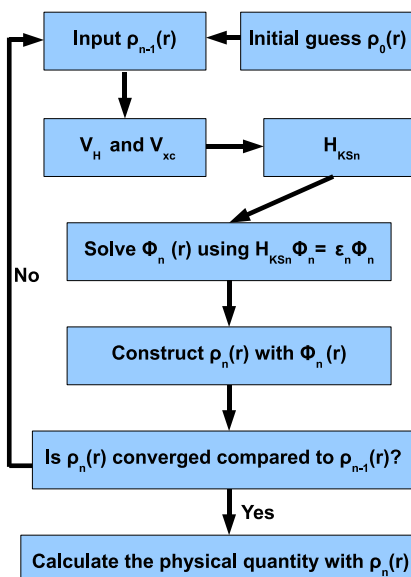


Figure 2.1: Schematic diagram of self-consistent loop for DFT calculation.

If we take a look at the Eq.(2.17), the Hartree potential v_H and exchange-correlation energy v_{xc} are both related to the charge density $\rho(\vec{r})$ which in turn is given by the solved $\phi_i(\vec{r})$. But to solve for $\phi_i(\vec{r})$, one needs the effective potential v_{eff} (or v_H and v_{xc}). This is naturally a self-consistency problem. Figure 2.1 shows the idea clearly. Hence, assuming a trial charge density ρ_{trial} , one can construct an initial H_{KS0} and solve the KS equation 2.17. The solution of the eigenvalue problem gives a set of wave functions ϕ_1 which can be used to calculate the charge density ρ_1 . Using ρ_1 , one constructs H_{KS1} and calculates ϕ_2 . The procedure repeats until the charge density and the KS Hamiltonian are consistent to each other. In this way, a self-consistent loop is set up which makes DFT a numerically applicable tool for electronic structure calculations.

2.2.3 Exchange-correlation energy functionals

As mentioned in the last section, Kohn-Sham theory switches an interacting many-body problem to a formally non-interacting single particle problem by introducing the effective potential v_{eff} . All the complications arising from the many-body physics are taken into account in the exchange-correlation term v_{xc} . However, the explicit

functional form of the exchange–correlation is so far unknown. In order to make DFT practical, further approximation for the exchange–correlation functional is required.

- LDA - local density approximation.

Kohn and Sham showed the idea of local density approximation (LDA)[37]:

$$E_{xc}^{LDA} = \int d\vec{r} \rho(\vec{r}) \epsilon_{xc}[\rho(\vec{r})] . \quad (2.18)$$

They stated that this approximation works in the limiting cases of slowly varying density and high densities. Here $\epsilon_{xc}[\rho(\vec{r})]$ is the exchange and correlation energy per particle of a homogeneous electron gas with density ρ . The limiting cases noted here are not realized in atoms, molecules or solids. Kohn and Sham commented that “we do not expect an accurate description of chemical bonding” with the LDA.[37]. However, more than 30 years passed after the first attempts were made to test its ability to describe the bonds in molecules, and it is remarkable that these tests showed that LDA could generally reproduce ground state geometries, vibration spectra, and moments of the density very well for a large list of problems[38]. The density functional theory has thus found widespread applications to molecules, clusters or other extended systems with parameter-free calculations. Most calculations have used the LDA described in Eq.(2.18) or some modified versions of it. The LDA functional is given with two parts: the exchange functional and the correlation functional. For the exchange functional, it can be solved analytically for the homogeneous electron gas. Usually, the exchange functional approximately adopts the solution for a homogeneous electron gas to a general case, which yields:

$$E_x^{LDA}[\rho] = -\frac{3}{4} \left(\frac{3}{\pi} \right)^{1/3} \int \rho(\vec{r})^{4/3} d\vec{r} . \quad (2.19)$$

However, the correlation functional is much more complicated and in general without an exact analytical form. It commonly uses fitting parameters (See equation 2.20 below) based on the results of quantum Monte Carlo (QMC) calculations for a homogeneous electron gas of different densities[39]. By interpolating these accurate values obtained from QMC simulations, one can reproduce

the exactly known limiting behavior. Various approaches, using different analytical forms for the exchange energy ϵ_c , have generated several LDA for the correlation functional[40, 41, 42]. For example, the most popular one proposed by Perdew and Zunger[40] is as follows:

$$\epsilon_c^{LDA-PZ} = \begin{cases} A \ln r_s + B + C r_s \ln r_s + D r_s & r_s \leq 1 \\ \gamma / (1 + \beta_1 \sqrt{r_s} + \beta_2 r_s) & r_s > 1 \end{cases}, \quad (2.20)$$

Where r_s , the Wigner-Seitz radius, satisfies :

$$\frac{4}{3} \pi r_s^3 = \frac{1}{\rho}. \quad (2.21)$$

and the fitting parameters A,B,C,D, γ , β_1 and β_2 can be found in the original literature[40].

- LSDA - local spin density approximation.

To treat spin polarized cases, a spin-dependent exchange-correlation functional known as local spin density approximation (LSDA) was presented in the literature[42]. In principle, LSDA is still based on the idea of LDA but it includes the degree of freedom for spin components:

$$E_{xc}^{LSDA}(\rho_\uparrow(\vec{r}), \rho_\downarrow(\vec{r})) = \int d\vec{r} \rho(\vec{r}) \epsilon_{xc}[\rho_\uparrow(\vec{r}), \rho_\downarrow(\vec{r})]. \quad (2.22)$$

where $\epsilon_{xc}[\rho_\uparrow, \rho_\downarrow]$ is the exchange and correlation energies per particle of a homogeneous, spin-polarized electron gas with spin-up and spin-down densities ρ_\uparrow and ρ_\downarrow , respectively.

By introducing a spin polarization factor ζ :

$$\zeta \equiv \frac{\rho_\uparrow - \rho_\downarrow}{\rho_\uparrow + \rho_\downarrow}, \quad (2.23)$$

the spin-polarized exchange-correlation functional $\epsilon_{xc}(\rho, \zeta)$ is written as:

$$\epsilon_{xc}(\rho, \zeta) = f(\zeta) \epsilon_{xc}^U(\rho) + (1 - f(\zeta)) \epsilon_{xc}^P(\rho). \quad (2.24)$$

Using the formula above, ϵ_{xc} can be evaluated by interpolation from the unpolarized (U) and fully polarized (P) functionals. Here the form of $f(\zeta)$ is based

on the Hartree-Fock and random-phase approximation suggested by von Barth and Hedin[42] and Vosko et al. [43], respectively. A similar idea can also be found in Ref[40] which will be used in one of the works presented in this thesis.

- GGA - generalized gradient approximation.

As stated above, the exchange-correlation functional in LDA is rooted in the homogeneous electron gas. For very non-homogeneous cases, the LDA may not be accurate enough. The non-homogeneous nature may be expressed in terms of gradients or higher spatial derivatives of the charge density. Therefore, the generalized gradient approximation (GGA) for the exchange-correlation functional has been invented[38]:

$$E_{xc}^{GGA}(\rho_{\uparrow}(\vec{r}), \rho_{\downarrow}(\vec{r})) = \int d\vec{r} f_{xc}[\rho_{\uparrow}(\vec{r}), \rho_{\downarrow}(\vec{r}), \nabla\rho_{\uparrow}(\vec{r}), \nabla\rho_{\downarrow}(\vec{r})] . \quad (2.25)$$

To obtain reasonable values, the functional f should be chosen carefully. Because it is not derived from a physical system, some natural conditions such as the sum rule $\int n_{xc}(\vec{r})d\vec{r} = -1$ should be imposed. The details for constructing GGA functionals can be found in Ref[38, 44, 45]. In comparison with LDA/LSDA, GGA tends to improve total energies, binding energies, energy barriers and energy differences for atomic geometries. However, GGA also expands and softens bonds, which sometimes correct and sometimes over-correct the LDA/LSDA predictions. For example, in most cases, the lattice constants optimized by LDA/LSDA are smaller than the experimental values while the results from GGA are overestimated slightly. In general, for systems where the charge density is slowly varying, GGA has been proved to favor the density inhomogeneity better than LDA does. For this reason, the xc-functional adopted in most calculations presented in this thesis is the GGA proposed by Perdew, Burke and Ernzerhof, so called PBE96 functional[44].

- Other functionals beyond LDA/GGA.

Although many multitudes of advances have been achieved by LDA/GGA, the requirement for more accurate functionals is still actively pursued in the litera-

ture. Various higher level (beyond GGA) functionals have appeared in both the physics and chemistry literature. Since they are not implemented in the work of this thesis, only a brief description is given for completeness.

- The hybrid scheme: combination of HF and DFT

The idea of a hybrid scheme is based on the fact that errors of exchange and correlation energy in LDA tend to have a balance with other approaches. It suggests that a combination of Hartree-Fock and DFT might be helpful in this regard, thus:

$$E_{xc}^{hybrid} = \alpha E_x^{HF} + E_c, \quad (2.26)$$

where α is a parameter to be chosen for satisfying the criteria of particular systems. For example, the B3LYP hybrid functional is widely used in quantum chemistry which is a combination of the Lee-Yang-Parr(LYP) GGA for correlation[46] with Becke's three-parameter hybrid functional B3 for the exchange[47]. The construction of hybrid functionals involves a certain amount of empiricism in the choice of functionals that are mixed and in the optimization of the weight factors given to the HF and DFT terms. The parameters are fitted using the calculated values in a large molecular database[47]. A more extreme example of this semi-empirical model of functional construction is Becke's 1997 hybrid functional[48] which contains 10 mixing parameters.

- Meta-GGA - kinetic functionals.

Another recent beyond-GGA functional is the Meta-GGAs. In addition to the density and its derivatives, Meta-GGA also requires Kohn-Sham kinetic energy $\tau_\sigma(\vec{r})$,

$$\tau_\sigma(\vec{r}) = \frac{1}{2} \sum_i^{occ} |\nabla \phi_{i\sigma}(\vec{r})|^2, \quad (2.27)$$

where $\phi_{i\sigma}$ are the occupied Kohn-Sham orbitals. So the exchange-correction function E_{xc} can be written as $E_{xc}[\rho_\uparrow, \rho_\downarrow, \nabla\rho_\uparrow, \nabla\rho_\downarrow, \nabla\tau_\uparrow, \nabla\tau_\downarrow]$. In the recent work of TPSS[49], the functional form satisfied the requirement that

the exchange potential be finite at the nucleus for ground state one- and two-electron densities. This is an exact constraint satisfied by LSDA but lost in GGA. Extensive numerical tests for atoms, molecules, and solids showed generally good results.

– LDA-SIC: self-interaction correction.

There is another type of functional called LDA plus self interaction correction (SIC). Most implementations of SIC are based on the scheme proposed Perdew and Zunger[40]:

$$E_{xc}^{approx,SIC}[n_{\uparrow}n_{\downarrow}] = E_{xc}^{approx}[n_{\uparrow}n_{\downarrow}] - \sum_{i,\sigma} (E_H[n_{i\sigma}] - E_{xc}^{approx}[n_{i\sigma}, 0]) , \quad (2.28)$$

where the SIC is applied orbital by orbital. If there is only one electron in the system, the Hartree approximation will be corrected by the exchange-correlation approximation. Usually, we believe LDA is exact for a completely uniform system, in such a limit the self-interactions are free. However, neither LDA nor GGAs satisfy the requirement of freedom from self-interaction in general. In particular, this self-interaction becomes critical for localized states, such as the d-states in transition-metal oxides. For such systems LDA-SIC has been shown to give great improvements compared to the usual LDA. But for thermochemistry, LDA-SIC does not seem to be significant. In LDA-SIC, the self-interaction term is directly removed from an approximate LDA functional which does not seem to be a good strategy to improve the functional's performance due to the ongoing balance of error cancellation. The LDA-SIC scheme was pointed out to lose the correct slow varying density limit in LSDA/GGAs or Meta-GGAs[50]. These issues call for more elaborate ways of constructing DFT-SIC functionals.

2.2.4 Numerical implementation of DFT

The Kohn-Sham equation effectively reduced the complicated N-body problem to a system of N single-particle problems. However, for real materials, the KS equation

is still too difficult to solve analytically and can only be solved numerically. The numerical implementation discussed in this section is to explain how to make the DFT scheme a practical tool for electronic structure calculations.

In this thesis, five DFT packages (MATDCAL, NanoDCAL, SIESTA, VASP and WIEN2K) have been used. MATDCAL[51] and NanoDCAL[52] are two LCAO (linear combination atomic orbital) based pseudo potential implementations of DFT for electronic structures and nonequilibrium transport calculations. In order to treat nonequilibrium transport, the Keldysh non-equilibrium green's function (NEGF) theory is implemented in combination of a self-consistent field theory (SCF) in MATDCAL/NanoDCAL while the SCF theory reduces to DFT at equilibrium. The SIESTA package[53] is another DFT code based on LCAO and pseudo potential for equilibrium electronic structure calculation. The VASP package is based on plane wave basis sets, which are using the ultra-soft and projected augmented wave (PAW) pseudo potential method[54, 55, 56, 57, 58]. The WIEN2K package[59] is based on a linear augmented plane wave (LAPW) method[60] that does not use pseudopotentials. For numerical implementations, we shall introduce three important issues, namely the boundary conditions, pseudo potential approximation and basis sets.

Boundary conditions

As a second order partial differential operator, to determine the Kohn-Sham Hamiltonian, we should specify the boundary conditions. Boundary conditions must be carefully specified to fit the physical problem of interest. From the point of view of numerical implementation, how to treat the boundary conditions is a technical issue.

In typical electronic structure calculations, Dirichlet[61] or periodic boundary conditions are adopted depending on the systems. For isolated systems such as free molecules or cluster of atoms, Dirichlet boundary condition[61] is applied. The criterion is to set the boundary large enough until the wave functions vanish at the boundary surface, as shown in Fig.2.2(a). For periodic systems, the Bloch theorem must be satisfied. The Bloch function is usually represented as:

$$\psi_{n\vec{k}}(\vec{r}) = e^{i\vec{k}\cdot\vec{r}} u_{n\vec{k}}(\vec{r}), \quad (2.29)$$

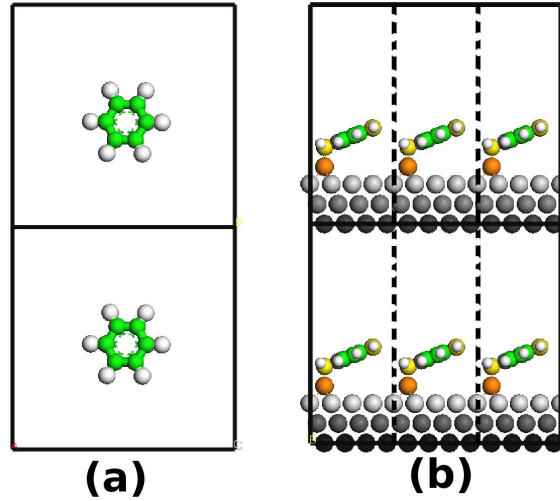


Figure 2.2: Schematic diagram of boundary conditions. (a) Dirichlet boundary condition for isolated systems such as free molecules. (b) Periodic boundary condition for periodic systems, the idea of supercell is also shown here using an example of the adsorption of benzene-dithiol (BDT) on Au(111) surface, a system studied in this thesis.

where \vec{k} is the wave vector in the first Brillouin Zone (BZ), and $u_{n\vec{k}}$ is the envelope function with the periodicity of the lattice. The corresponding energy eigenvalue is $\epsilon_n(\vec{k}) = \epsilon_n(\vec{k} + \vec{K})$, with periodicity \vec{K} of a reciprocal lattice vector. The energies associated with the index n vary continuously with wave vector \vec{k} and form an energy band identified by the band index n . Bloch's theorem decomposes the Hilbert space into \vec{k} -subspaces using the irreducible representations of the lattice translation groups.

Another subject related to the boundary conditions is the supercell. Forming a supercell makes it possible to extend the use of Bloch's theorem to a larger class of non-periodic structures. For example, in surface science problems there is no translational symmetry in the direction perpendicular to the surface, but one can still put the surface and several layers underneath the surface into a large box or cell, and periodically repeat this cell in all directions to form a super-lattice. In this large cell, a vacuum region is included which isolates the atoms from their periodic images in the neighboring cells, as shown in Fig2.2(b). The vacuum region should be large enough to ensure that the repeated surface slabs or molecules do not interact. Within the supercell approach, the ground state expectation value of a one-body operator,

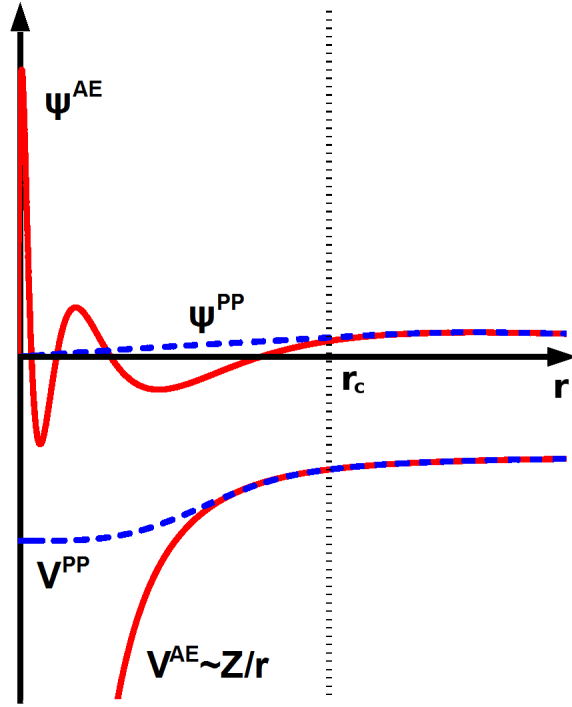


Figure 2.3: Schematic diagram of a pseudopotential. The wave function (ψ^{AE}) calculated in the Coulomb potential (V^{AE}) of the nucleus (red) is compared to the pseudo wave function (ψ^{PP}) calculated in the pseudopotential (V^{PP}) (blue). Beyond the chosen cutoff radius r_c , both the pseudo wave function and pseudopotentials should be identical to the all-electron ones.

A , is evaluated as an integral over the first Brillouin zone

$$\langle A \rangle = \frac{1}{V_{BZ}} \int_{BZ} A(\vec{k}) d\vec{k}, \quad (2.30)$$

where V_{BZ} is the volume of the first Brillouin zone, $A(\vec{k}) = \sum_n \langle \psi_{n\vec{k}} | A | \psi_{n\vec{k}} \rangle$, n runs over the occupied states. In practice the integral is approximated by a finite sum, $\int dk/V_{BZ} \rightarrow \sum_k \omega_k$, where ω_k is the weight of k -points.

In Chapter 3, the NEGF based electronic transport theory will be introduced. Another type of boundary condition related to the open systems of the transport problems will be discussed combining with the implementation of NEGF.

Pseudo potential approximation

The idea of pseudo potential approximation is rooted on the fact that most physical properties of solids are dependent on the valence electrons to a much greater degree

than on the tightly bound core electrons. The core electrons are chemically inert: they do not participate in bonding and essentially only serve to screen the potential of the bare nucleus seen by the valence electrons. Therefore, as a good approximation, it is reasonable to remove the core electrons and the nuclear potential and replace them with a core-electron screened pseudo potential. This approximation reduces the number of electrons in the calculation.

The schematic plot in Fig2.3 shows how to construct the pseudopotential. Due to the strong ionic potential (Z/r), the true valence wave functions (ψ^{AE}) are rapidly oscillating in the core region. By introducing the pseudo potential approximation, it is able to switch the valence wave functions (ψ^{AE}) to a relatively smooth pseudopotential wave functions (ψ^{PP}). There are several ways for pseudopotential generation and it is not unique. However, all these methods must satisfy several basic criteria, as follows:

- The pseudopotential radial wave function should be exactly the same as the all-electron wave function beyond a cutoff radius r_c , where r_c is defined for each angular momentum dependent wave functions.
- There are no radial nodes in the pseudopotential wave function for $r < r_c$. This way, the pseudopotential wave function is a smooth function in the core region. In other words, for $r < r_c$ the pseudo wave functions are non-oscillatory and their first and second derivatives should be continuous.
- The core charge should be exactly the same for pseudo and all-electron wave functions which ensures that the pseudo atoms produce the same scattering properties as the ionic core, which is the norm-conserving criteria.
- The valence eigenvalues calculated by all-electron and pseudopotential methods should be equal.
- Excited states can also be included in pseudopotential generation.

As a by-product of this Ph.D. thesis research, a database of norm-conserving non-local pseudopotentials is produced and carefully tested. The detailed procedures

for constructing the pseudopotential is included in Appendix A following the algorithm described in the pseudopotential and basis generation codes NanoBase[62] and ATOM[63]. Since the pseudopotential of an atom is not unique, some pseudopotentials are better than others under specific situations. The quality of a pseudopotential is determined by its transferability, that is, its ability to recreate all electron properties in a variety of chemical environments.

Basis sets

Basis sets used for electronic structure calculations can be roughly divided into two groups. The first is designed to mimic the exact eigenstates of the atoms in the system. Examples of such basis functions are the linear combination atomic orbitals (LCAO) used by DFT packages SIESTA[53], MATDCAL[51] and NanoDCAL[52], or the Gaussian atom-centered orbitals (GTO) used in the Gaussian electronic structure package[64]. In general, these DFT codes give reliable results with a relatively small number of basis functions, making them optimal for large scale computation. On the other hand, there is no consistent way to extend these basis sets and thereby converge the results with respect to the size of the basis sets.

The second type of basis set covers the system-independent functions such as plane waves[54, 55, 56, 57, 58]. The main advantage of the plane wave basis sets is that their size can be systematically increased until the calculated results are converged with respect to the number of basis functions. Plane wave basis sets are generally considered to be able to give more accurate results than the LCAO basis. The number of plane wave basis functions required to obtain convergence is normally so large that direct solution of the eigenvalue problem of matrix within the entire basis space is not possible. Instead one uses iterative methods to determine the lowest (occupied) part of the spectrum. However, inversion of Hamiltonian matrix is necessary for constructing Green's functions in quantum transport calculation. Therefore, LCAO basis sets are generally useful in this case. We shall focus on introducing LCAO methods. Other methods for constructing the basis will be mentioned and we cite references for readers' interests[64, 60].

To solve the Kohn-Sham Hamiltonian, we specify a LCAO basis set. The atomic orbitals are precisely those obtained from the pseudopotential, namely:

$$\phi_{lm}(\vec{r}) = R_l(r)Y_{lm}(\Omega_{\vec{r}}) = R_l(r)|l, m\rangle \quad (2.31)$$

By evaluating a particular linear combination, we can get the real-type spherical harmonics $|l, M\rangle$ with $|l, m\rangle$:

$$|l, M\rangle = \frac{1}{\sqrt{2}}(|l, m\rangle + (-1)^M |l, -m\rangle) \quad (2.32)$$

$$|l, M\rangle = \frac{1}{\sqrt{2i}}(|l, m\rangle - (-1)^M |l, -m\rangle), \quad (2.33)$$

where l is the angular momentum, m is the projection of angular momentum and $M = |m|$.

To further reduce numerical computation, the orbital radial function requires a finite cutoff. With this extra cutoff, atoms far apart do not have direct orbital overlap and, as a result, the Hamiltonian matrix becomes a sparse matrix. There are several techniques for cutting off the pseudo-orbital radial function. The methods we use follow the existing literature[53, 62]. For example, one can specify the cutoff energy for the generated orbitals. Aside from this, in order to make the radial functions more flexible, a confining potential is added to the atomic Hamiltonian which is used to generate the basis orbitals. For our work here, this confining potential is parameterized in the following form:

$$V(r) = V_0 \frac{e^{-\left(\frac{r_c - r_i}{r - r_i}\right)}}{r_c - r}, \quad (2.34)$$

where r_i and V_0 are input parameters (strictly speaking, defined variationally). Here r_c specifies the orbital cutoff (not to be confused with the core radius cutoff in the pseudopotential generation), r_i determines the onset of the confining potential, and V_0 is the strength of the potential applied. The above potential diverges at $r = r_c$, ensuring the orbital is confined with r_c . In some of the studies, we found that the choice of basis orbital parameters to be very important which can even qualitatively influence the calculated physical results. For example, the calculation with a LCAO

basis without optimization gives the wrong band gap for bulk Si. For such systems, we use a downhill simplex optimization method[65] to optimize the physical quantities (total energy, energy bands, etc.) of the system with respect to the basis set parameters described above[66]. A full set of the optimized basis database has thus been generated which we shall publish for the research community to use[52]. The basis set in the database are carefully checked with benchmark calculations by higher precision codes such as VASP[58], WIEN2K[59] and gaussian98[64] with details in Appendix B.

Quantum transport theory

In this chapter, we shall review quantum electronic transport theory. Specifically, we focus on the Landauer theory which is applied throughout this thesis. Classically, charge transport in conductors usually shows an Ohmic behavior. However, in the quantum regime the Ohm's law may not be valid depending on several length scales which are important in characterizing the transport regimes. These length scales are,

- *Fermi wave length* λ_f : The Fermi wave length is proportional to the square root of electron density n_s

$$\lambda_f = 2\pi/k_f = \sqrt{2\pi/n_s} , \quad (3.1)$$

where k_f is the wave number and n_s is the electron density. At low temperatures, the electric current is contributed by electrons whose energy is close to the Fermi energy. Hence the conductance is mainly contributed by electrons having the Fermi wave length.

- *Mean free path* L_m : The mean free path is a measure of the distance traveled by electrons between two consecutive collisions with impurities. For static scatterers, the collisions are elastic since no energy is lost or gained by the electron. The mean free path can be specified by the momentum relaxation time τ_m : $L_m = v_f\tau_m$. Here v_f is the Fermi velocity. The mean free path may be influenced by extrinsic factors such as temperature and density of impurities. A typical scale for L_m found in transition metals under regular experimental environment is around 10-20Å[67].

- *Phase-relaxation length L_ϕ* : The phase-relaxation length is a measure of the distance traveled by electron before the phase of its wave function is lost due to inelastic scattering events. Similar to the mean free path, the phase-relaxation length can be specified with the phase relaxation time τ_ϕ : $L_\phi = v_f \tau_\phi$. Depending on the system details, L_ϕ can be larger, similar to or smaller than L_m . At low temperature, L_ϕ can be as long as many microns in high mobility semiconductors. In this thesis, we shall consider system sizes L such that $L \ll L_\phi$, hence inelastic scattering is not a concern.
- *Screening length L_s* : The screening length is a measure of the distance beyond which electron-electron interaction is screened. Estimated by the Thomas-Fermi free electron gas model, $L_s = [D(E_f)e^2/\epsilon_0]^{(-1/2)}$, where $D(E_f)$ is the density of states near the Fermi level and ϵ is the dielectric constant in vacuum. For metals, $D(E_f)$ is generally very large hence L_s is very small, e.g. a typical value is around 1-10Å[67]. L_s is an important reference for constructing buffer layers in the scattering region of our device model (see Section 3.3.1).

3.1 The Landauer quantum transport theory

The Landauer scattering theory[68, 69] provides a general framework for investigating quantum transport from a quantum scattering point of view. We can use a simple one-dimensional (1D) transport junction (Fig.3.1) to illustrate the idea. In this figure, the device has a scattering region of length L , and two electrodes extending to electron reservoirs at $z = \pm\infty$. The reservoirs maintain electrochemical potentials μ_L and μ_R , respectively. Since the electrodes are assumed to be the metal, they acquire the same chemical potentials as the reservoirs. The discussion of Landauer formula can be found in many excellent papers and we shall follow the book of Datta[70] for our discussion.

Consider a single transverse mode in the $+k$ state incoming from the left electrode. It scatters into the conductor (scattering region). Assuming the conductor is an uniform electron gas with charge density n per unit length, the right-moving current

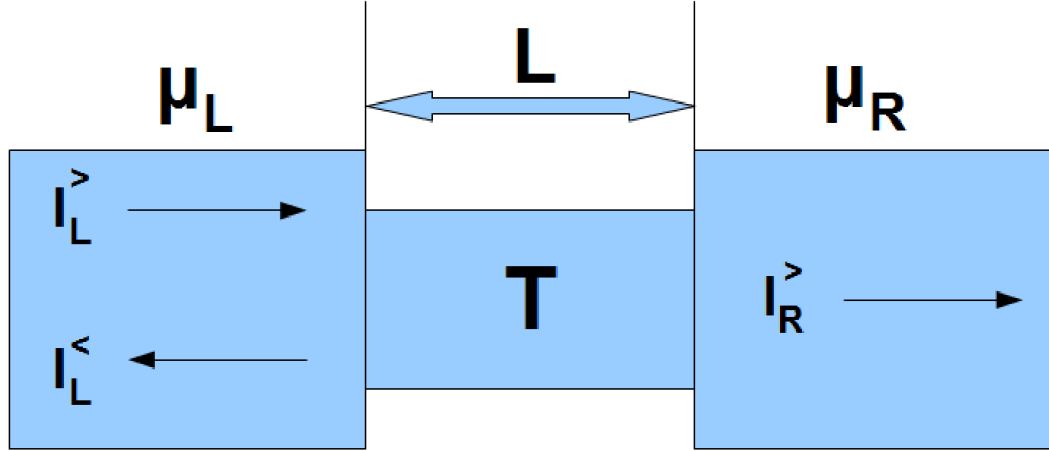


Figure 3.1: Electrons propagating from the left contact suffer some elastic scattering. T is the transmission probability for the electron to traverse the system. The electrochemical potential in the two electron reservoirs are μ_L and μ_R (assuming $\mu_L > \mu_R$), respectively. L is the length of the scattering region of the device.

from the left lead can be written as:

$$I_L^> = \frac{e}{L} \sum_k v f_L(E) = \frac{e}{L} \sum_k \frac{1}{\hbar} \frac{\partial E}{\partial k} f_L(E) , \quad (3.2)$$

where $f_L = f(E - \mu_L)$ is the Fermi-Dirac distribution function of the left electrode and E is the electron energy. Changing the sum to an integral according to:

$$\sum_k \rightarrow 2(\text{spin}) \times \frac{L}{2\pi} \int dk , \quad (3.3)$$

we obtain

$$I_L^> = \frac{2e}{h} \int f_L(E) dE . \quad (3.4)$$

Using T to denote the transmission probability through the conductor, the probability of reflection is then $1 - T$. Following Eq.3.4, the left-moving current in the left lead $I_L^<$ can be written as:

$$I_L^< = \frac{2e}{h} \int [f_L(E)(1 - T) + f_R(E)T] dE . \quad (3.5)$$

It consists of two parts: the states back-scattered by the conductor and the states transmitted from the right lead. The net current I_{total} in the left lead is:

$$I_{total} = I_L^> + I_L^< = \frac{2e}{h} \int [f_L(E) - f_R(E)] T dE . \quad (3.6)$$

Considering the zero temperature limit, we obtain:

$$I = \frac{2e}{h} T |\mu_L - \mu_R| \longrightarrow G = \frac{2e^2}{h} T . \quad (3.7)$$

Here $G_o \equiv (2e^2)/h$ is the conductance quanta $(12.9\text{K}\Omega)^{-1}$.

The single channel result, Eq.3.7, can be generalized to multi-channel, such that

$$G = \frac{2e^2}{h} \sum_i T_i , \quad (3.8)$$

where i is the channel number. This way, the current is related to the transmission probability for electrons to traverse elastically through the conductor. More recently, inelastic scattering problems are also investigated by a generalized Landauer theory[71].

Finally, for finite bias voltages, the current formula in Eq.3.7 becomes:

$$I = \frac{2e}{h} \int T(E, V_b) [f_L(E) - f_R(E)] dE . \quad (3.9)$$

Here the transmission coefficient $T(E, V_b)$ is not only energy dependent but also bias (V_b) dependent. The central problem in quantum transport theory is to calculate $T(E, V_b)$ for a given device Hamiltonian.

3.2 The non-equilibrium Green's function theory

Another theoretical formalism for quantum transport analysis is based on the Keldysh non-equilibrium Green's functions (NEGF)[72]. For coherent quantum conductors, NEGF gives the same results as the Landauer theory. In particular, combined with methods in materials theory such as the density functional theory (DFT), NEGF formalism has become a powerful *ab initio* approach for investigating quantum transport phenomena in nanoelectronics.

In the following, we shall briefly review the derivation of Landauer theory from the NEGF formalism and list a set of important expressions which we will use in the rest of the thesis. To save space, we refer the interested readers to Refs.[70, 72, 73, 74] for further details of NEGF.

3.2.1 NEGF and Landauer theory

Starting from the Hamiltonian of a system that includes the central device scattering region (C) and the left/right (L,R) semi-infinite leads (see Fig.3.2), the second-quantized form of the Hamiltonian is:

$$\hat{H} = \sum_{k\alpha \in L,R,n} \epsilon_{k\alpha} c_{k\alpha}^\dagger c_{k\alpha} + H_c(\{d_n^\dagger\}, \{d_n\}) + \sum_{k\alpha \in L,R,n} [V_{k\alpha,n} c_{k\alpha}^\dagger d_n + H.C.] . \quad (3.10)$$

where $k\alpha$ labels the electronic states with momentum k and channel α in lead L or R; $\{d_n^\dagger\}$ and $\{d_n\}$ are creation and annihilation operators in the central scattering region for charge carriers. The last term represents the coupling between the leads and the central scattering region, where $V_{k\alpha}$ is the coupling constant. The current in the left lead can be evaluated from the time evolution of the occupation number, that is

$$I_L = -e \frac{d\hat{N}_L}{dt} = -e \langle \dot{N}_L \rangle = -\frac{ie}{\hbar} \langle [H, N_L] \rangle . \quad (3.11)$$

Taking in the definition of H in Eq.3.10 and $N_L = \sum_{k\alpha \in L,n} c_{k\alpha}^\dagger c_{k\alpha}$, we have:

$$I_L = \frac{ie}{\hbar} \sum_{k\alpha \in L,n} [V_{k\alpha,n} \langle c_{k\alpha}^\dagger d_n \rangle - V_{k\alpha,n}^* \langle d_n^\dagger c_{k\alpha} \rangle] \quad (3.12)$$

$$= \frac{e}{\hbar} \sum_{k\alpha \in L,n} \int \frac{dE}{2\pi} [V_{k\alpha,n} G_{n,k\alpha}^<(E) - V_{k\alpha,n}^* G_{k\alpha,n}^<(E)] . \quad (3.13)$$

Here the lesser Green's function $G^<(t)_{n,k\alpha} = i \langle c_{k\alpha}^\dagger d_n(t) \rangle$ [72]. Following the derivation of Meir and Wingreen in Ref.[74], the lesser Green's function can be obtained through time-ordered contour Green's functions and expressed as advanced and retarded Green's functions using the Langreth theorem[72]:

$$G_{n,k\alpha}^<(E) = \sum_{k\alpha,m} V_{k\alpha,n}^* [G_{nm}^r(E) g_{k\alpha}^<(E) + G_{nm}^<(E) g_{k\alpha}^a(E)] . \quad (3.14)$$

Take this expression back to Eq.3.13 and use the lesser Green's function of the left lead: $g_{k\alpha,k\alpha}^< = 2\pi i f_L(E) \delta(E - \epsilon_{k\alpha})$, we have:

$$I_L = \frac{ie}{\hbar} \sum_{\alpha \in L,nm} \int dE \rho_\alpha(E) V_{\alpha,n}(E) V_{\alpha,m}^*(E) \times \{f_L(E) [G_{n,m}^r - G_{n,m}^a] + G_{n,m}^<(E)\} . \quad (3.15)$$

Similarly, we can get the equation of current for the right leads. For steady states, the expression of current can be symmetrized to the following form,

$$I = \frac{ie}{2\hbar} \int dE Tr \{ [f_L(E)\Gamma_L - f_R(E)\Gamma_R](G^r - G^a) \} + Tr((\Gamma_L - \Gamma_R)G^<). \quad (3.16)$$

where $\Gamma_{L,R} = 2\pi \sum_{\alpha \in (L,R), n, m} \rho_\alpha(E) V_{\alpha, n}(E) V_{\alpha, m}^*(E)$. So far, the expression is exact. Using the Dyson equation for the Green's function:

$$G = G_0 + G_0 \Sigma G. \quad (3.17)$$

Employing the Langreth's rules for the expression $D = ABC$ involving three operators[72]:

$$D^< = A^r B^r C^< + A^r B^< C^a + A^< B^a C^a, \quad (3.18)$$

we have:

$$G^< = G_0^< + G_0^< \Sigma^a G^a + G_0^r \Sigma^< G^a + G_0^r \Sigma^r G^<. \quad (3.19)$$

Solving the above equation iteratively, we obtain

$$G^< = (1 - G_0^r \Sigma^r)^{-1} G_0^< (1 + \Sigma^a G^a) + (1 - G_0^r \Sigma^r)^{-1} G_0^r \Sigma^< G^a. \quad (3.20)$$

Applying the following expressions,

$$G^r = G_0^r + G_0^r \Sigma^r G^r \quad \text{and} \quad G^a = G_0^a + G_0^a \Sigma^a G^a, \quad (3.21)$$

we can simplify Eq.3.20 to:

$$G^< = G^r (G_0^r)^{-1} G_0^< (1 + \Sigma^a G^a) + G^r \Sigma^< G^a \quad (3.22)$$

$$= G^r (G_0^r)^{-1} G_0^< (G_0^a)^{-1} G^a + G^r \Sigma^< G^a \quad (3.23)$$

$$= (1 + G^r \Sigma^r) G_0^< (1 + \Sigma^a G^a) + G^r \Sigma^< G^a. \quad (3.24)$$

The first term in $G^<$ is nonzero for truly bound states and vanishes identically for states acquiring any width. When the device scattering region is coupled to the electrodes, states in the scattering region are broadened by the coupling. Hence the first term in Eq.(3.24) vanishes. $G^<(E)$ is simplified to:

$$G^<(E) = G^r(E) \Sigma^<(E) G^a(E), \quad (3.25)$$

where the lesser self energy term $\Sigma^<(E)$ is:

$$\Sigma^<(E) = \sum_{k,\alpha=L,R} |V_{k\alpha}|^2 g_{k,\alpha}^< = i[f_L(E)\Gamma_L + f_R(E)\Gamma_R] . \quad (3.26)$$

So we have:

$$G^<(E) = iG^r(E)[f_L(E)\Gamma_L + f_R(E)\Gamma_R]G^a . \quad (3.27)$$

and

$$G^r - G^a = G^r((G^a)^{-1} - (G^r)^{-1})G^a = G^r(\Sigma^r - \Sigma^a)G^a = iG^r(\Gamma_L + \Gamma_R)G^a . \quad (3.28)$$

Taking Eq.3.27 and 3.28 into Eq.3.16, the current formula reduces to:

$$I = \frac{2e}{h} \int dE [f_L(E) - f_R(E)] Tr\{\Gamma_L G^r \Gamma_R G^a\} . \quad (3.29)$$

Compared with the Landauer formula Eq.3.9, we immediately identify:

$$T(E, V_b) = Tr\{\Gamma_L G^r \Gamma_R G^a\} . \quad (3.30)$$

Hence transmission coefficients can be determined by the NEGF. In general, the transport problem of an open system is reduced to the evaluation of the retarded and advanced Green's functions for a given device Hamiltonian.

3.2.2 Construction of nonequilibrium charge density

In order to calculate the device Hamiltonian for a device nanostructure, various materials theories can be applied. We shall use the density functional theory (DFT) for our work. In conventional DFT at equilibrium, the charge density $\rho(r)$ is constructed by solving the Kohn-Sham eigenstates as discussed in the previous Chapter, namely Eq. 2.7. Note that in Eq.2.7, the distribution function, f_i , is the Fermi-Dirac distribution. For open device systems during current flow, the system is actually under non-equilibrium conditions. Therefore the density matrix is best constructed by NEGF, namely:

$$\rho = -\frac{i}{2\pi} \int_{-\infty}^{+\infty} G^<(E) dE . \quad (3.31)$$

In other words, NEGF allows us to obtain a non-equilibrium density matrix which is necessary for analyzing non-equilibrium quantum transport problems.

To proceed further, we write Eq.3.10 in matrix form by expanding all quantities using a complete basis set.

$$H = \begin{pmatrix} H_L & \tau_1 & 0 \\ \tau_1^\dagger & H_C & \tau_2 \\ 0 & \tau_2^\dagger & H_R \end{pmatrix}. \quad (3.32)$$

Here, $\tau_{1,2}$ are the coupling terms between the left/right lead and the central scattering region. The matrix form of the Green's function satisfies:

$$(ES - H)G(E) = I. \quad (3.33)$$

where G is the Green's function corresponding to the Hamiltonian H, E is the energy, and S is the overlap matrix which arises if a non-orthogonal basis set is used. Eq.3.33 refers to an infinite matrix equation due to the presence of leads which extend to $\pm\infty$.

Plugging the Hamiltonian Eq.3.32 into Eq.3.33, we can solve for the retarded and advanced Green's functions of the central device region:

$$G^{r,a}(E) = (ES - H_C - \Sigma_L^{r,a}(E) - \Sigma_R^{r,a}(E) \pm i0^+)^{-1} \quad (3.34)$$

Here $\Sigma_L^{r,a}$ and $\Sigma_R^{r,a}$ are

$$\Sigma_L^{r,a}(E) = \tau_1^\dagger g_{sL}(E) \tau_1 \quad (3.35)$$

$$\Sigma_R^{r,a}(E) = \tau_2^\dagger g_{sR}(E) \tau_2. \quad (3.36)$$

$\Sigma^{r,a}$ is the self-energy that accounts for effects of leads which interact with the central region. Here g_{Ls} and g_{Rs} are the surface Green's functions for the leads, which will be introduced in Section 3.3.3. Going back to Eq.3.30, $\Gamma_{L,R}$ are defined by self-energy terms as follows:

$$\Gamma_{L,R}(E - qV_{L,R}) = i(\Sigma_{L,R}^r(E) - \Sigma_{L,R}^a(E)), \quad (3.37)$$

where q is the symbol for charge (q=-1 for electrons) and $V_{L,R}$ are the bias of the left and right lead.

With these expressions, the calculation of transport properties can be accomplished by solving the Green's functions[70, 72].

Recalling Eq.3.25 and 3.26, the density matrix ρ is written as

$$\rho = -\frac{i}{2\pi} \int_{-\infty}^{+\infty} dE G^r(E) \Sigma^<(E) G^a(E) , \quad (3.38)$$

where $\Sigma^<(E)$ is given in Eq.3.26. This expression is used to determine the non-equilibrium density matrix.

In equilibrium, namely $V_L = V_R$, $f_L(E) = f_R(E)$, the lesser self-energy $\Sigma^<(E)$ can be simplified,

$$\Sigma^<(E) = if(E)\Gamma(E) = -f(E)(\Sigma^r(E) - \Sigma^a(E)) = -f(E)((G^a)^{-1} - (G^r)^{-1}) . \quad (3.39)$$

If we define a spectral function $A = i(G^r - G^a)$, then $G^<$ can be rewritten as:

$$G^<(E) = G^r(E)\Sigma^<(E)G^a(E) = -f(E)(G^r(E) - G^a(E)) = if(E)A(E) . \quad (3.40)$$

This expression is the fluctuation-dissipation theorem. We can rewrite the formula for the density matrix in equilibrium as:

$$\begin{aligned} \rho &= -\frac{i}{2\pi} \int_{-\infty}^{E_f} G^r(E) \Sigma^<(E) G^a(E) dE \\ &= \frac{1}{2\pi} \int_{-\infty}^{E_f} f(E) A(E) dE \\ &= \frac{1}{2\pi} \int_{-\infty}^{E_f} f(E) A(E) dE \\ &= -\frac{1}{\pi} \int_{-\infty}^{E_f} f(E) \text{Im}(G^r(E)) dE , \end{aligned} \quad (3.41)$$

where the distribution function $f(E) = 1$ when states are occupied. In this way, the lesser Green's function is simplified to the retarded Green's function which is important for numerical computation (see below). Even if at non-equilibrium, the above equation is still valid as long as $f_L(E) = f_R(E)$. However, for $f_L(E) \neq f_R(E)$, no simplification of $G^<$ can be made. With these considerations, we can rewrite the nonequilibrium density matrix into two terms:

$$\rho = -\frac{1}{\pi} \int_{-\infty}^{\min(\mu_L, \mu_R)} f(E) \text{Im}(G^r(E)) dE - \frac{i}{2\pi} \int_{\min(\mu_L, \mu_R)}^{\max(\mu_L, \mu_R)} G^<(E) dE . \quad (3.42)$$

The first term is for energies where $f_L(E) = f_R(E)$, and is called “equilibrium contribution”. The second term is for $f_L(E) \neq f_R(E)$, and is called “non-equilibrium contribution”. Eq. 3.42 is used in our numerical implementation for computing the density matrix.

3.3 Implementation of the NEGF theory

The numerical implementation of NEGF theory for solving realistic systems involves several major challenges:

- A transport junction is actually infinitely large due to the semi-infinite long electrodes. One has to reduce the infinite system to one that can be calculated. A two-probe model is therefore introduced that divides the device into a central scattering region plus the left/right electrodes. Periodic boundary conduction is applied to the transverse direction and a k-sampling in the transverse 2D Brillouin zone should be carried out efficiently.
- Because the Green’s functions are ill behaved near the real energy axis, calculating the integral in Eq. 3.42 can be difficult. An appropriate contour integral is introduced in order to reduce the numerical difficulty.
- For realistic materials and parameter-free modeling, one has to calculate the Hamiltonian of the device. The combination of DFT with NEGF provides a good solution to this problem.

Some important implementation details are discussed below.

3.3.1 Two-probe model

In order to implement the NEGF technique for realistic nanostructures, an appropriate atomic model is necessary. Let us start by considering a general device system shown in Fig.3.2 where a molecule is sandwiched by two semi-infinite slab electrodes. The central scattering region of this system is taken as the molecule plus some buffer

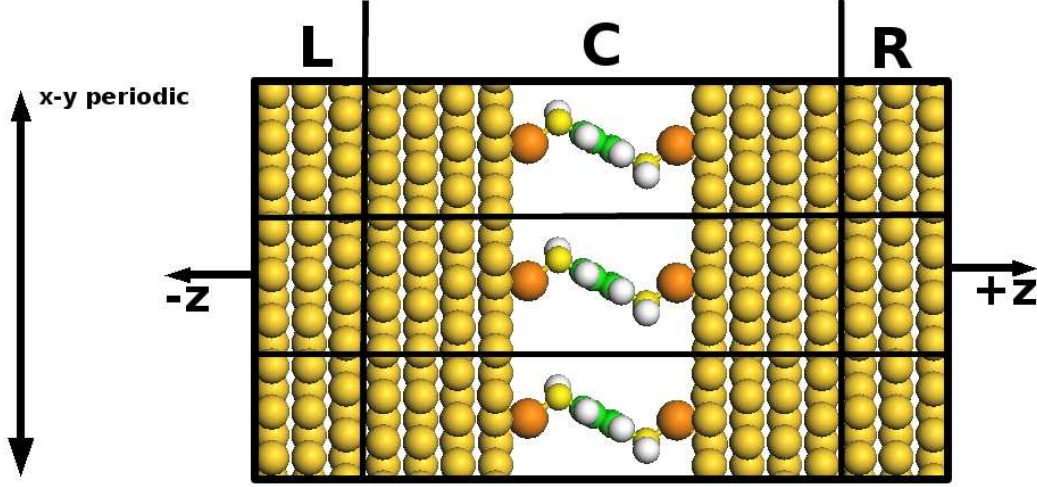


Figure 3.2: Schematic diagram of a two-probe device model with periodic boundary conditions applied in the x-y directions. A molecule with four buffer layers in the central scattering region is sandwiched by two semi-infinite slabs. A bulk boundary condition is also applied at the boundary of the central region in the transport direction (z) for calculating the electronic potential self-consistently. The bulk properties of the leads are calculated with DFT.

layers. The length of the buffer layers depends on the screening length of the material of leads. At the boundary of the central region, the lattice is fixed to the bulk electrode material so that the electric potential at the boundary matches the bulk value of the electrodes. This screening approximation is justified due to the short screening length of metals (10\AA). Assuming electrons travel along the z direction (see Fig.3.2), periodic boundary conditions are applied to the x-y directions. The electrodes of the device are therefore 3-dimensional (3D). This is important for properly modeling magnetism in spintronic devices.

To impose the two-probe boundary conditions, the Hartree potential is solved in real-space of the central scattering region. Assuming the lattice vector of the central scattering region is chosen as (L_x, L_y, L_z) , the boundary condition is as follows:

$$V_H(x + L_x, y, z) = V_H(x, y, z) \quad (3.43)$$

$$V_H(x, y + L_y, z) = V_H(x, y, z) \quad (3.44)$$

$$V_H(x, y, 0) = A(x, y) \quad (3.45)$$

$$V_H(x, y, L_z) = B(x, y) . \quad (3.46)$$

Here $A(x, y)$ and $B(x, y)$ are the Hartree potentials at the boundary of left/right scattering region along z-direction. The Hartree potential is obtained by solving the Poisson equation

$$\nabla^2 V_H = -4\pi\rho \quad (3.47)$$

Practically, the Poisson equation can be solved by fast-Fourier transform (FFT) with high accuracy in the periodic x-y directions. In the z-direction, it is solved by finite differencing on a fine grid. After imposing the above boundary conditions, the charge density and the Hartree potential match smoothly at the device boundaries. In practical calculations, the thickness of the buffer layer is checked to make sure that the screening approximation is well satisfied.

3.3.2 2-D Brillouin zone sampling

In Fig.3.2, the transverse x-y directions are periodic hence the Bloch theorem can be applied. As a result, the Hamiltonian is determined in k-space. Let us define the Bloch wavevector \vec{k}_{\parallel} and the lattice vector $\vec{R}_{\parallel} = n_x\vec{a} + n_y\vec{b}$. The Bloch state corresponding to the orbital α is:

$$\psi_{\alpha} = \frac{1}{\sqrt{N_{\parallel}}} \sum_{R_{\parallel}} e^{ik_{\parallel}R_{\parallel}} \phi_{\alpha}(R_{\parallel}) . \quad (3.48)$$

The Hamiltonian is then written as[51]:

$$H^{\vec{k}_{\parallel}} = \sum_{n_x, n_y} H_{n_x, n_y} e^{i\vec{k}_{\parallel} \cdot \vec{R}_{\parallel}} . \quad (3.49)$$

Projecting the Hamiltonian to the k_{\parallel} -direction of the 2D Brillouin zone, the retarded Green's function $G^r(E)$ can be written as[51]:

$$G_{k_{\parallel}}^r(E) = \left(\begin{array}{ccc} ES_L^{k_{\parallel}} - H_L^{k_{\parallel}} + \Sigma_L^{k_{\parallel}}(E) & ES_{CL}^{k_{\parallel}} - H_{CL}^{k_{\parallel}} & 0 \\ (ES_{CL}^{k_{\parallel}} - H_{CL}^{k_{\parallel}})^{\dagger} & ES_C^{k_{\parallel}} - H_C^{k_{\parallel}} & (ES_{CR}^{k_{\parallel}} - H_{CR}^{k_{\parallel}})^{\dagger} \\ 0 & (ES_{CR}^{k_{\parallel}} - H_{CR}^{k_{\parallel}})^{\dagger} & ES_R^{k_{\parallel}} - H_R^{k_{\parallel}} + \Sigma_R^{k_{\parallel}}(E) \end{array} \right)^{-1} . \quad (3.50)$$

where $H_L^{k_{\parallel}}$, $H_C^{k_{\parallel}}$ and $H_R^{k_{\parallel}}$ are the finite sized sub-matrices of the L (left), C (center), R (right) regions, respectively. $S_{CL}^{k_{\parallel}}$, $S_{CR}^{k_{\parallel}}$, $\Sigma_L^{k_{\parallel}}(E)$, $\Sigma_R^{k_{\parallel}}(E)$ are the sub-matrices corresponding to the quantities in real space. Unlike the infinite real-space Hamiltonian matrix defined in Eq.3.32, the projected Hamiltonian matrix for each \mathbf{K} corresponds to a finite-size one in the central scattering region. This way, adoption of the Bloch theorem effectively switches the infinitely large system in real space to a finite-size problem with \mathbf{k} -sampling. The introduction of \mathbf{k} -sampling also brings numerical issues. For example, a very large \mathbf{k} -mesh is required for spintronic devices (see Chapter 4). This difficulty can be somewhat relieved by using an adaptive \mathbf{k} -sampling scheme.

3.3.3 Self-energy

Next, we determine the self-energy terms in Eq.3.36, which are due to the semi-infinite electrodes. In our device model, we assume the electrodes are perfect crystals extending to $z \pm \infty$. As shown in Eq.3.36, the self-energy Σ is related to the surface Green's functions $g_{sL,sR}$. Roughly, $g_{sL,sR}$ can be calculated starting from the surface layer of the lead which has a finite number of atoms. Afterward, one adds the second layer of the lead using the Dyson equation; and then the third layer, etc.. This is iterated to an infinite number of layers. Practically, the iteration converges after a finite number of layers are included. In practical implementations, there are at least two different approaches: the Bloch wave method[75] and iteration method[76]. We have implemented both methods. For more details, interested reader are referred to the original papers. After $g_{sL,sR}$ is obtained, we multiply the coupling matrices $\tau_{1,2}$ as in Eq.3.36. By comparing Eq.3.32 and Eq.3.50, $\tau_1 = ES_{CL} - H_{CL}$.

3.3.4 Contour integration

The integration in Eq. 3.42 can be difficult due to the poles of the Green's functions near the real axis. For a retarded Green's function, the poles are close to the real axis in the lower complex energy plane. For the equilibrium contribution of Eq.3.42, namely the first term on the right hand side, an upper-plane contour will be useful to bypass the poles. At zero temperature, the contour can be a semi-circle in the upper

complex energy plane. This scheme can also be generalized to finite temperature[1]. For the non-equilibrium contribution of Eq.3.42, namely the second term on the right hand side, poles exist in both the upper and the lower complex energy plane because $G^< = G^r \Sigma^< G^a$. Therefore, in the energy window of $[\mu_L, \mu_R]$, there is no other choice except doing the integration along the real energy axis which may require a massive number of energy points. A way to smooth out the sharp peaks of $G^<(E)$ is to add a small broadening $i\eta$ to the Green's functions, and reduce η systematically to vanishing values.

Figure 3.3 is a schematic diagram for the contour chosen in our calculations. A closed contour starts from a straight line $C_2([\infty + i\Delta, \mu_L - \sigma + i\Delta])$, followed by a semi-circle segment C_1 , then go along the real energy axis by $[-\infty + i0^+, \infty + i0^+]$ and finally enclose the contour with $[\infty + i0^+, \infty + i\Delta]$. Since there is no state far above the Fermi level, the contour $[\infty + i0^+, \infty + i\Delta]$ is negligible. The values for Δ, σ are flexible. Since all poles of the retarded Green's function G^r are below the real axis, G^r in the integration contour is analytic. Poles of the Fermi distribution function are $z_n = i(2n + 1)\pi KT$, $n=0,1,\dots$. The poles with $n < \Delta/(2\pi KT) - 1/2$ are adopted in the contour integral. Recall the first term of equation 3.42, we have:

$$\oint G^r(z)f(z)dz = -2\pi iKT \sum_{z_n} G(z_n) . \quad (3.51)$$

Therefore, the first term of Eq.3.42 is written as:

$$-\frac{1}{\pi} \int_{E_B}^{+\infty} G^r(E)f(E)dE = \frac{1}{\pi} \int_{C_1+C_2} G^r(z)f(z)dz + 2iKT \sum_{z_n} G(z_n) . \quad (3.52)$$

The implementation of the contour integral significantly reduces the calculation cost and improves the precision. Because the spectral function in the complex energy plane is rather smooth, only a small number of energy points are required for the path along contour C_1 . The method of gaussian quadrature is used with high efficiency and accurate calculations.

3.3.5 The NEGF-DFT approach

In Chapter 2, we have reviewed DFT electronic structure calculation. In order to determine the Hamiltonian of nanoelectronic devices at non-equilibrium, DFT is com-

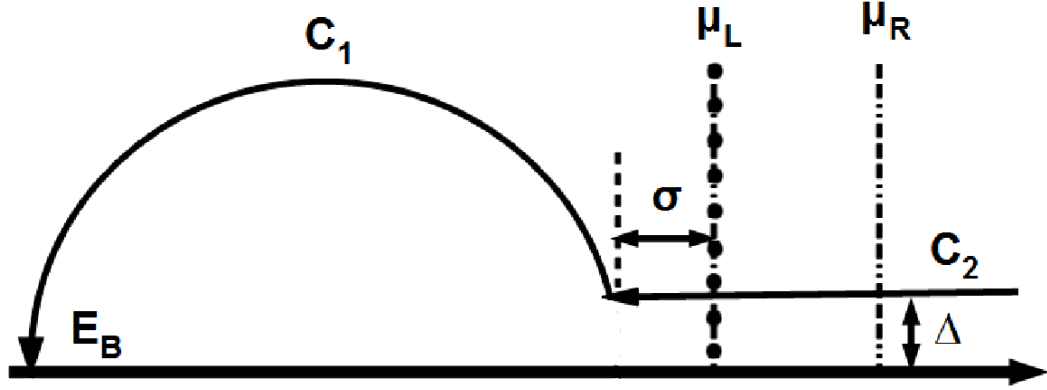


Figure 3.3: Closed contour at finite temperature. For: L ($[\infty + i\Delta, \mu_L - \sigma + i\Delta]$), C, $[-\infty + i0^+, \infty + i0^+]$ and $[\infty + i0^+, \infty + i\Delta]$, the poles (black dots) due to Fermi distribution function are enclosed, they are at $z_n = i(2n + 1)\pi KT$, and n is an integer $0, 1, 2 \dots$. E_B is the bottom of the valence bands.[1]

bined with NEGF[73]. Therefore, our electronic transport calculations are based on carrying out DFT within the framework of NEGF. Practically, a self-consistent loop is shown in Fig.3.4 and the NEGF-DFT approach runs as follows:

- Step 1: Prepare the self-energy due to electrodes, as introduced in Section 3.3.3. In particular, since the electrode is at equilibrium, its Hamiltonian is calculated by standard DFT;
- Step 2: Starting from a trial density, calculate the exchange-correlation potential V_{xc} using the local density approximation or other approximations (please refer to Section 2.2 for details), and calculate the Hartree potential V_H by solving the Poisson equation 3.47;
- Step 3: Construct the Kohn-Sham Hamiltonian \hat{H} and determine the Green's functions G^r by Eq.3.50 and $G^<$ by Eq.3.25;
- Step 4: Calculate the density matrix $\hat{\rho}$ by NEGF Eq.3.31;
- Step 5: Use the newly obtained density matrix $\hat{\rho}$ to go back to Step 2. Repeat the process until \hat{H} and $\hat{\rho}$ are converged.

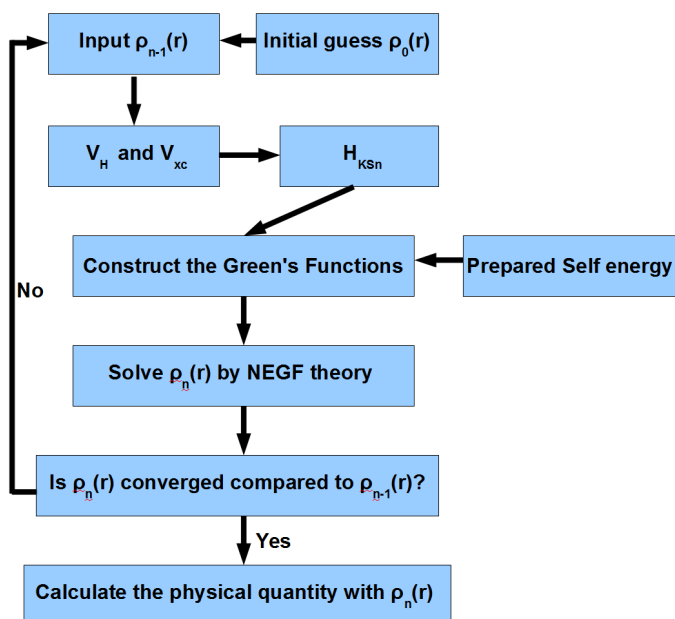


Figure 3.4: Schematic diagram of the self-consistent loop in the NEGF-DFT method.

The NEGF-DFT self-consistent loop is rather similar to that of the standard DFT discussed in Section 2.2 (Fig.2.1). Instead of solving an eigenvalue problem in standard DFT, NEGF-DFT evaluates the density matrix by Eq.3.42 including the nonequilibrium contributions.

3.4 Summary

In this Chapter, we briefly reviewed the electronic transport theory of Landauer. The NEGF formalism provides a mathematical framework for solving the transmission coefficients in the Landauer formula. Combined with DFT, the Hamiltonian of electronic devices can be determined by the NEGF-DFT formalism from atomic first principles without any phenomenological parameters. As a many-body theory, an additional power of NEGF is its capability of handling effects of interactions. For example, the electron-phonon and electron-electron interactions cannot be incorporated easily in the scattering matrix formalism, but can be readily included in the NEGF formalism by appropriate self-energies.

Tunnel Magnetoresistance of molecular wires

As a first application of the NEGF-DFT formalism discussed in Chapter 3, in this Chapter we investigate spin polarized quantum transport in molecular wires.

4.1 Introduction to spintronics

Spintronics is an emerging technology that exploits the intrinsic spin degree of freedom of the electron for electronic device applications. From a fundamental point of view, spintronics deals with magnetic phenomena at the nano-scale. Spintronics includes investigation of spin transport in magnetic tunnel junctions, spin injection from magnetic materials to non-magnetic materials, dilute magnetic semiconductors, and phenomena of spin dynamics and relaxation.

There are several recognizable effects in spintronics. One is the anisotropic magnetoresistance (AMR). The phenomena are notable since the resistance of a ferromagnet is dependent on the relationship between the direction of current flow and the orientation of the magnetization. AMR is more difficult to analyze than conventional charge transport problems since the resistance is now related to the spin degree of freedom. Another active subject is dilute magnetic semiconductors (DMS). These materials are based on traditional semiconductors but are doped with a small amount of transition metal atoms. By annealing the doping profile, the corresponding magnetic property of DMS can be significantly changed even after crystal growth[77]. Understanding the microscopic physics of ferromagnetism in DMS is still an unsettled issue at present. Investigations of spintronics have also revived some old issues in magnetism, for instance the well known but unresolved microscopic origin of the anomalous Hall effect

in magnetic metal has received renewed research from a modern perspective[78]. The earliest research about spin-dependent electron transport in solid devices were reported in the 1980s. The most well-known discovery was due to the work of Albert Fert and Peter Grünberg *et al.* on the giant magnetoresistance (GMR) effect in 1988[79]. Since then GMR has been widely used in devices for magnetic storage and magnetic sensors, as such it made a huge impact on the information technology. In some sense, GMR is responsible for the huge research effort on spintronics today.

In spintronics, spin polarized quantum transport may be the most interesting and practically important topic. Since conventional micro-electronic switching devices (transistors) do not concern spin, it is expected that new generation of devices may arise by combining the conventional system with spin-dependent phenomena. A very large effort has been paid to understand the magnetic tunnel junctions (MTJ)[80]. A MTJ consists of two magnetic layers sandwiching an insulating barrier material. It was found that tunnel current is large when the magnetic moments of the two magnetic layers are in parallel configuration (PC), and it is small when they are anti-parallel (APC). Such a tunnel magnetoresistance (TMR) has attracted increasingly more attention because a MTJ is a digital system having two states coded into the magnetic configuration, and it provides the device principle of the magnetic random access memory (MRAM)[80, 81]. MRAM is already commercial device, but its large-scale application as the RAM in computers has not been achieved so far due to several practical issues which still need to be resolved. Nevertheless, MRAM has a greater data processing speed, a lower energy consumption and a higher integration density. In this Chapter we shall investigate the TMR effect of a molecular scale MTJ.

Compared with GMR, TMR achieves a large impedance to match the circuit electronics. TMR has larger magnetoresistance (about 10 times at room temperature[82]) than GMR. Theoretical analysis has already played very important roles in the TMR research. For instance, in 2001 Butler *et al.* and Mathon *et al.* made a theoretical prediction of a coherent spin filtering effect in Fe/MgO/Fe MTJ which gives rise to the a TMR ratio reaching several thousand percent[83, 84]. Afterward,

the TMR in Fe/MgO/Fe junctions was reported by Parkin, and by Yuasa, which reached over 200% at room temperature [85, 86] and with an even higher TMR 600% (room temperature) - 1100%(4.2K) in CoFeB/MgO/CoFeB junctions depending on the temperatures[87].

Besides the widespread attention to MgO, using molecules as spin transport elements has led to the notion of molecular spintronics, which has attracted considerable attention both experimentally[16, 88, 89, 90, 91, 92, 93, 94] and theoretically[95, 96, 97, 98, 99, 100, 101, 102, 103]. Despite these efforts, molecular spintronics is still in its infancy. Molecules have genuine advantages in spin-dependent quantum transport because they have relatively weak spin-orbital coupling and hyperfine interaction so that spin-coherence can be maintained for a longer extent. Molecular spintronics also exploit chemistry methodologies to control and manipulate quantum transport of spin, in addition to charge. The scope of investigations is down to the single molecule level: a perspective that has not existed before. Theoretically, molecular spintronics requires careful and quantitative investigations to establish a physical picture on many important and general issues. These include what controls spin injection from ferromagnetic contacts to the molecule, what role is played by external bias voltage, how spin transport is related to chemical details and to what extent the state-of-the-art theory can compare with measured data.

To address these important problems, we shall focus on the experimental device of Petta, Slater and Ralph[16] who measured low-temperature quantum spin transport of octanethiolate molecules connected to the outside world by Ni contacts using a nanopore fabrication technique[24]. Using the NEGF-DFT techniques described in Chapter 2 and 3, we have investigated the TMR effects and IV characteristics in the Ni/octanethiolate/Ni molecular junctions. The results are satisfactory in many aspects compared with Ralph's measurements[16].

The organization of this chapter is as follows: in Sec.(4.2), we review the general concepts and properties of tunnel magnetoresistance. In Sec. (4.3), we review the experimental background and other related work. In Sec. (4.4), we describe details

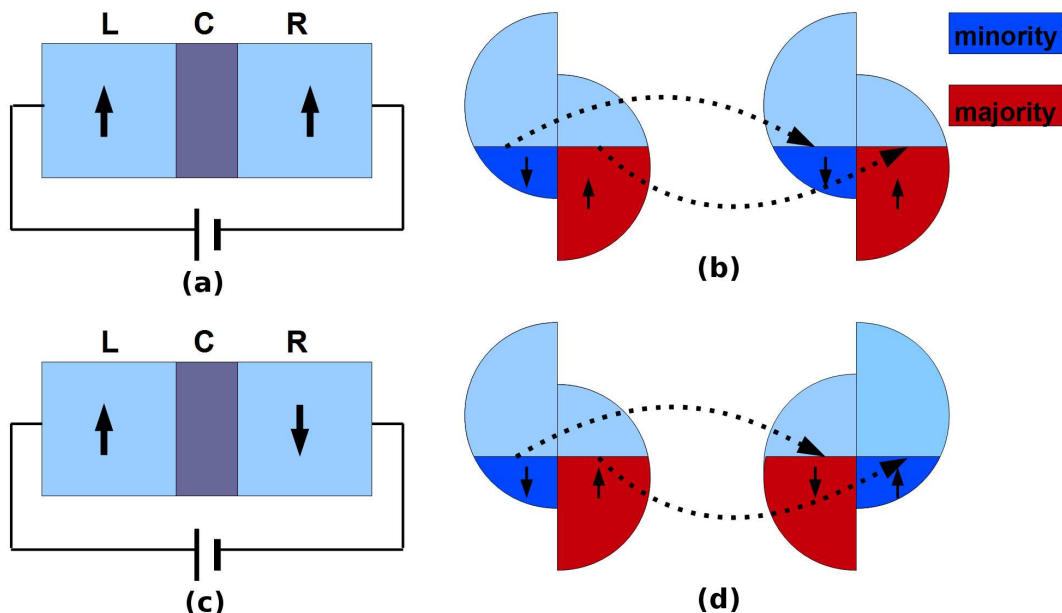


Figure 4.1: Schematic illustration of a typical TMR device: an insulator or molecular layer sandwiched by two ferromagnetic leads. (a) Parallel (PC) and (c) antiparallel configurations (APC) of spin polarization in the left/right ferromagnetic leads. The corresponding spin-resolved density of the states in ferromagnetic metals are also shown in (b) and (d), in which the blue block represents the minority-spin subband while the red block is the majority-spin subband.

of the NEGF-DFT calculation for Ni/octanethiolate/Ni junctions. We also give the analysis of calculated results and discuss the underlying physics. In Sec. (4.5) we summarize the work in this Chapter.

4.2 Tunnel Magnetoresistance

A typical TMR device consists of two ferromagnetic electrodes separated by a thin insulator (F/I/F) layer. The insulating layer is usually thin enough (typically within a few nanometers) for electrons to tunnel through from one ferromagnetic electrode to the other. Therefore, the TMR phenomenon is best explained by quantum mechanics. A typical TMR device is shown in Fig4.1. A thin insulating layer is sandwiched between two ferromagnetic films. Applying an external magnetic field, the direction of the magnetization of the left/right ferromagnetic film can be switched independently.

In terms of the terminology of magnetism, the larger spin population in a ferromagnet is referred as “majority spin channel”, while the one with smaller spin population is the “minority spin channel”. If we specify that the direction of the magnetization points to the “+z” in Cartesian coordinates, we can label the majority-spin as up-spin (\uparrow) and minority-spin as down-spin (\downarrow). The two simplest and most typical configurations are shown in Fig4.1, namely, parallel configuration (PC) and antiparallel configuration (APC). Let us use the symbol of $\uparrow\uparrow$ for PC and $\downarrow\downarrow$ for APC for simplification of notation. As already mentioned in the last section, usually it is easier for electrons to tunnel through the insulating layer in PC than in APC. Therefore, two states of electrical resistance arise by simply adjusting the orientations of magnetization in the left/right ferromagnets.

Conceptually, we can understand the TMR phenomenon as follows. Let us consider a MTJ whose left and right leads are made of the same magnetic metal. For PC, the electrons in the majority spin channel from the left lead tunnel through the barrier and enter the right lead which is in the same majority state. This process has relatively large tunnelling probability. For APC, on the other hand, the electrons with majority-spin from the left will enter the right ferromagnet which is in the minority-spin state. Hence the electrons should overcome an extra spin flipping barrier[104]. If we define it as Δ_{ex} , the resistance of APC is thus increased due to Δ_{ex} . The corresponding TMR in a F/I/F type MTJ is:

$$TMR = \frac{R_{\uparrow\downarrow} - R_{\uparrow\uparrow}}{R_{\uparrow\uparrow}} = \frac{G_{\uparrow\uparrow} - G_{\uparrow\downarrow}}{G_{\uparrow\downarrow}} = \frac{I_{\uparrow\uparrow} - I_{\uparrow\downarrow}}{I_{\uparrow\downarrow}} \quad (4.1)$$

where $G = 1/R$ is the conductance of the junction. In 1975, Julliere proposed a simple model for the tunneling behavior of MTJ[105]. In this model, the tunneling current through the insulating layer is proportional to the density of states at the Fermi level of the electrodes on both sides of the tunnel barrier. Hence,

$$I_{\uparrow\uparrow} \propto D_1^\uparrow(E_f)D_2^\uparrow(E_f) + D_1^\downarrow(E_f)D_2^\downarrow(E_f) \quad (4.2)$$

$$I_{\uparrow\downarrow} \propto DD_1^\uparrow(E_f)D_2^\downarrow(E_f) + D_1^\downarrow(E_f)D_2^\uparrow(E_f) \quad (4.3)$$

where $D_{1/2}^{\uparrow/\downarrow}(E_f)$ is the density of states (DOS) of the left/right ferromagnetic leads,

respectively. If we define the spin polarization factor as:

$$P = \frac{D^\uparrow(E_f) - D^\downarrow(E_f)}{D^\uparrow(E_f) + D^\downarrow(E_f)} \quad (4.4)$$

TMR of the Julliere model[105] can be rewritten as:

$$TMR = \frac{P_1 P_2}{1 - P_1 P_2} \quad (4.5)$$

The Julliere model highly simplifies the complicated spin coupling in TMR to the bulk property of the left/right ferromagnetic leads. Although the detailed spin tunneling process is completely neglected in this simple model, it points to an important outcome: the TMR is sensitive to the spin-polarization factors at the Fermi level of the two ferromagnetic layers. Ideally, if the two ferromagnetic layers are 100% spin polarized ($P_1 = P_2 = 1$), TMR will be infinite. In such a case, the TMR junction becomes a perfect electric switch under the adjustment of magnetization direction. A low and an infinite resistance is obtained in PC or APC, if the MTJ is built with such perfectly polarized materials. This kind of $P = 1$ material is called a half metal. As a result, the search for half metal materials has become an active field. Several materials such as NiMnSb, CrO₂, La_{0.7}Sr_{0.3}MnO₃, and Fe₃O₄ were reported to show half metallic behaviors[106, 107, 108, 109].

Due to the lack of details for spin tunneling and electronic coupling at the ferromagnet/insulator interface, the Julliere model fails in making quantitative predictions in the MTJ. In order to understand the TMR effects better, higher level theoretical techniques are necessary.

4.3 *Experimental and theoretical background*

In 2004, Ralph's group in Cornell University measured the electronic transport in Ni / octanethiolate / Ni molecular magnetic tunnel junctions[16]. They fabricated these junctions using a nanopore technique[24] where an octanethiolate monolayer was sandwiched by two Ni contacts. The transport properties of octanethiolate molecule have been extensively investigated using non-magnetic leads[110, 111, 112, 113] where electronic transport is found to be dominated by tunneling through σ -bonds of the

alkane-chain. Since σ -bonds give rise to very large resistance, alkane molecules make a good tunnel barrier for magnetic tunnel junctions. As shown in the experiment[16], the TMR value for Ni/octanethiolate/Ni junctions can reach up to 16%. The TMR is sensitive to the applied bias. In particular, the TMR quickly decays as bias is increased. It decays to zero at bias 40 mV. In addition, the TMR shows an asymmetric dependence on the bias.

The experiment of Ref.[16] has inspired many theoretical works on molecular spintronics[96, 97, 98, 99, 100, 101, 102, 103] at a qualitative level where various phenomenological parameters were adjusted to fit the experimental data. A challenge to theory is to be able to make parameter-free quantitative predictions that can be compared directly to the experimental data. In this regard, a recent calculation[101] for octanethiolate produced a TMR ratio that is many times larger than the experimental data, and it does not decay with bias voltage as observed in the experiment[16]. The reason for the discrepancy was unknown[101].

In the rest of this Chapter, we shall apply our first-principles NEGF-DFT method to the Ni/octanethiolate/Ni molecular MTJ. We emphasize several key points in order to accurately analyze quantum spin transport in realistic molecular junctions,

- Calculations should be *ab-initio* in order to properly address the specific chemical properties of molecules. Although a tight-binding model with semi-empirical parameters may provide some insights into this problem, it is very difficult, if not impossible, to obtain the correct charge transfer and spin polarization of the magnetic junctions.
- The leads of the device should be modeled to have a three-dimensional (3D) geometry so that bulk properties of ferromagnetic materials can be reproduced. It is well known that magnetism is strongly depending on dimensionality and it is questionable to use quasi-1D leads to simulate magnetic junctions as was done in the literature[101]. Due to the 3D leads, very careful k-sampling must be done to obtain accurate results.

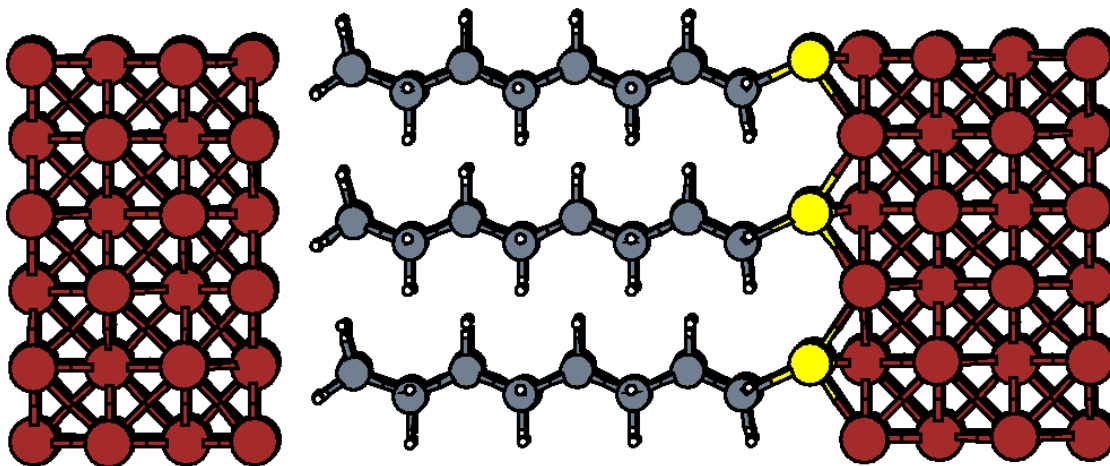


Figure 4.2: Schematic diagram of the device(Ni/octanethiolate/Ni junctions). The scattering central region consists of octanethiolate molecules and four Ni(100) buffer layers connected to each side of the molecules. As shown, the structure is asymmetric.

- The Hamiltonian should be calculated self-consistently at finite voltages for the purpose of voltage-dependence analysis. One can not simply assume that the applied bias voltage drops linearly along backbone of the molecule due to the complicated metal-molecule interactions. There is no priori knowledge about how much voltage drops at the contacts and how much on the molecules, therefore the Poisson equation and the charge density must be solved self-consistently.

The non-equilibrium Green's function combined with DFT (NEGF-DFT) and applying the local spin density approximation (LSDA) introduced in Chapters 2 and 3 covers the above points. It will be used in our analysis.

4.4 Calculation details

The molecular device we consider consists of two semi-infinite Ni(100) slabs sandwiching a 8-octanethiolate, $C_8H_{17}S$, as shown in Fig.4.2. The Ni slabs extend to $z = \pm\infty$ along the transport direction z . The system extends periodically in the transverse x, y directions with a super-cell cross section of $3.52 \times 3.52 \text{ \AA}$. We divide the

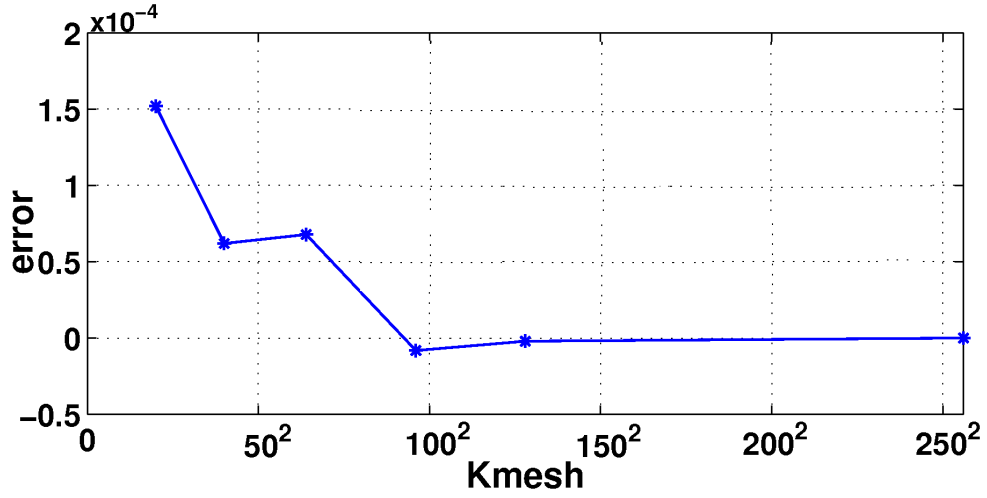


Figure 4.3: Convergence of Green's function with respect to size of k-mesh. Vertical axis: error $\equiv Tr(|G^r|)/Tr(|G^r(256^2\text{k-mesh})|) - 1$. For 96×96 or greater k-mesh, the result converges.

Ni/octanethiolate/Ni device into three regions: a scattering region consisting of the molecule and four layers of Ni atoms on either side, and left/right Ni leads. The atomic structure of the scattering region is relaxed using the total energy DFT electronic package SIESTA[53], where the outermost layer of Ni atoms are fixed at their bulk positions. The relaxed scattering region is then connected to the periodic Ni leads for two-probe NEGF-DFT analysis. In NEGF-DFT calculations, we adopt double-zeta-polarized basis for C, H and S, and single-zeta-polarized basis for Ni atoms. All the basis sets used in the calculation are generated following the scheme described in Appendix A and B. The exchange-correlation is treated at the local spin density approximation level[42]. As a check, we verified that the calculated band structure, density of states (DOS) and spin splitting for bulk Ni are in excellent agreement with large basis DFT methods such as the LSDA-PAW in VASP[54, 55, 56, 57, 58] and LSDA-LAPW in WIEN2K[59].

A major difficulty in calculating transport of Ni/octanethiolate/Ni is the enormous number of k-points necessary for sampling the two-dimensional (2D) Brillouin zone (BZ). Recalling the NEGF-DFT self-consistent analysis introduced in Chapter 3, the non-equilibrium density matrix is calculated by NEGF, $\hat{\rho} = \int_{BZ} dk_{\parallel} \hat{\rho}_{k_{\parallel}}$ with $\hat{\rho}_{\parallel} = \int dE G_{k_{\parallel}}^<(E)$. Here $k_{\parallel} \equiv (k_x, k_y)$ samples the 2D BZ of the Ni leads. All the

physical quantities will be evaluated after the integration of NEGF($G^<$) over k_{\parallel} . For the Ni/octanethiolate/Ni system, the fine electronic structures in the BZ of the Ni surface and the sharp transmission resonances require very careful examination of the k-sampling in order to calculate the $G^<$ to high accuracy. Since it is unclear how to reduce the k-points due to lack of symmetry, we apply an adaptive sampling technique with a very fine k-mesh. To find out how fine it should be, we calculated the retarded Green's function $G_{k_{\parallel}}^r$ with a k-mesh of 256×256 k-points and use this as a benchmark. We then reduce the k-mesh: the difference of $|G_{k_{\parallel}}^r|$ for smaller k-mesh and the benchmark is shown in Fig.4.3. It shows that a k-mesh of at least 96×96 is necessary to converge the BZ integration of the density matrix $\hat{\rho}$. A smaller mesh does not give sufficiently accurate results. In Fig.4.3 the difference of $|G^r|$ by smaller k-mesh to the benchmark is 10^{-4} . Although this appears to be small, it translates to a larger error in the density matrix and influence quantitative transport results. The reason is that the error due to small k-mesh is not uniformly distributed in matrix elements of G^r . Therefore we fix the k-mesh to be 96×96 in all our calculations, which means that for each iteration step toward self-consistency, 96^2 independent NEGF-DFT calculations must be performed for each energy E (up to 110 E-points) to converge the density matrix, and this is repeated for each bias voltage. After the self-consistent NEGF-DFT procedure is converged, we calculate the total transmission coefficient for spin channel σ by a second BZ integration using the same k-mesh:

$$T_{\sigma}(E) = \int_{-\pi}^{\pi} \frac{dk_{\parallel}}{(2\pi)^2} \tilde{T}_{\sigma}(E, k_{\parallel}) \quad (4.6)$$

where the $\tilde{T}_{\sigma}(E, k_{\parallel})$ is the BZ resolved transmission function for a given k_{\parallel} . It is obtained by :

$$\tilde{T}_{\sigma}(E, k_{\parallel}) = Tr \left[G_{k_{\parallel}}^r \Gamma_{L, k_{\parallel}} G_{k_{\parallel}}^a \Gamma_{R, k_{\parallel}} \right] \quad (4.7)$$

where all quantities on the right hand side are functions of energy E .

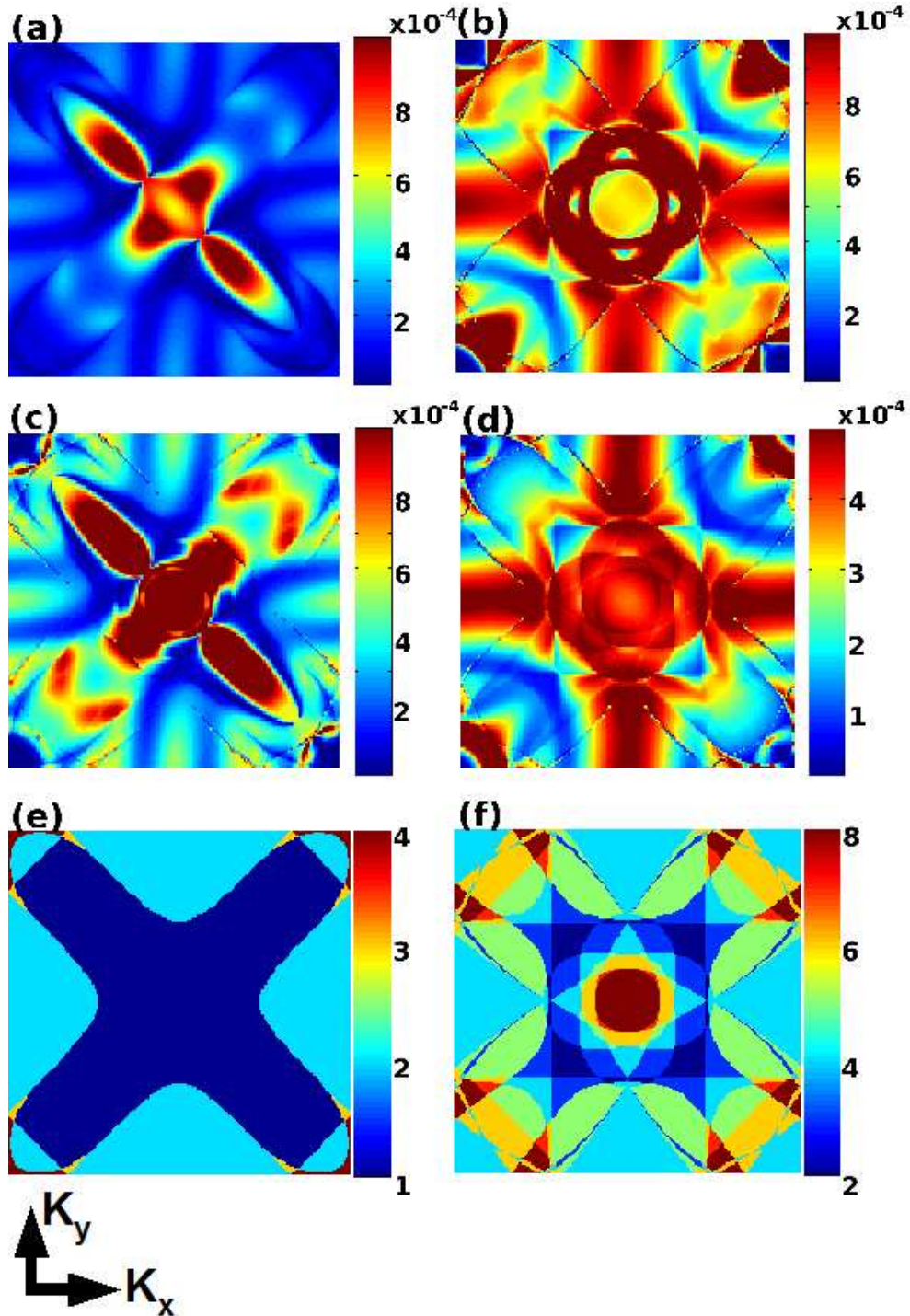


Figure 4.4: (a)-(d): Zero bias transmission coefficient at E_f in the 2D Brillouin zone. (a) Spin-up channel for PC; (b) spin-down for PC; (c) spin-up for APC; (d) spin-down for APC. Note the different transmission scales indicated by the vertical bar. (e) and (f): Number of incoming channels in the Ni-lead at E_f in 2D BZ. Note spin-up electron is majority carrier but has less DOS at E_f . For this reason the number of conducting channel of spin-up, (e), is less than that of spin-down, (f).

4.5 Calculation results

Fig.4.4a-d plot the k -resolved quantity $\tilde{T}_\sigma(E, k_{||})$ versus $k_{||} = (k_x, k_y)$ when magnetic moments of the Ni leads are in parallel or anti-parallel configurations (PC or APC, respectively). Let us call these T-maps. The T-map is obtained at zero bias by fixing $E = E_f$, the Fermi energy of the Ni leads (shifted to $E_f = 0$ in all our plots). The main impression is the “hot spots” in the BZ where $\tilde{T}_\sigma(E, k_{||})$ has very sharp resonance features at various points of $k_{||}$, indicated by high values of \tilde{T}_σ (hot colour) on top of a rather smooth background value (cold colour). Hot spots are known to exist in conventional magnetic tunnel junctions[114]. For the molecular junction here, we find that the smooth background of $\tilde{T}_\sigma(E, k_{||})$ is largely due to transmission channels in the Ni leads that tunnel through the molecular layer, while the hot spots are due to resonance transmission which is sensitive to $k_{||}$. To understand the smooth background value (cold colour regions) of $\tilde{T}_\sigma(E, k_{||})$, Fig.4.4e,f plot the BZ resolved number of conducting channels in the Ni lead at E_f : the spin-up channel is of a 4-petal pattern with channel number 1 to 4; the spin-down channel is a complicated pattern with channel number 2 to 8. These patterns are rather similar to cold colour regions of Fig.4.4a,b for PC situation. For APC, Fig.4.4c,d are a combination of both spin-up and -down channel patterns: this is expected because APC involves both up and down magnetic configurations of the leads.

To understand the sharp hot spot features on top of the smooth background in T-map, we have calculated the real space scattering wave function at various $k_{||}$. When $k_{||}$ is not at a hot spot, the modular of wave function essentially decays exponentially along the molecule; but when $k_{||}$ is on a hot spot, the wave function oscillates which indicates a resonance in transmission. For a given k -point, one can obtain a quasi-1D Hamiltonian, $H_{k_x, k_y} = \sum_{I_x I_y} H_{I_x I_y} \exp [i(I_x k_x + I_y k_y)]$, where $H_{I_x I_y}$ is the Hamiltonian matrix between the unit cell indexed by $I_x I_y$ and the unit cell indexed by 00. With the k -dependent Hamiltonian, the scattering problem can be solved analogous to a 1D δ -barrier problem. Figure4.5 shows the real space scattering wave functions at two typical k -points k_1 and k_2 . k_1 corresponds to the point of hot spots while k_2 is

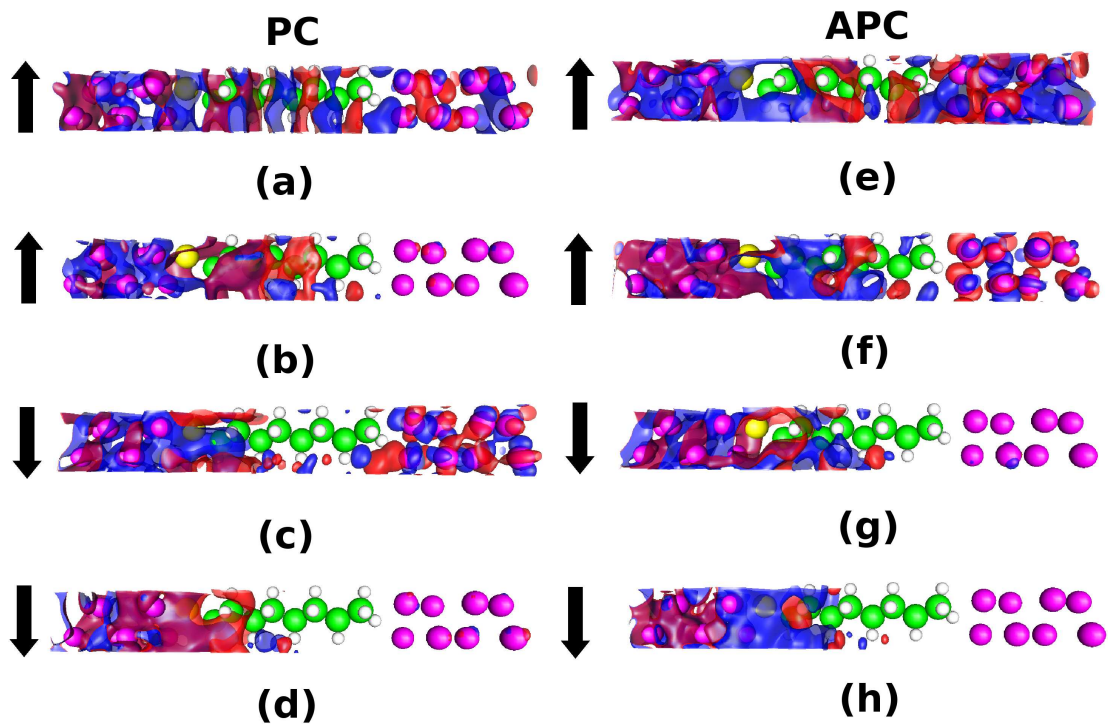


Figure 4.5: (a) k_1 for spin up of PC, $T = 1.1 \times 10^{-3}$ (b) k_2 for spin up of PC, $T = 1.02 \times 10^{-4}$ (c) k_1 for spin down of PC, $T = 8.7 \times 10^{-3}$ (d) k_2 for spin down of PC, $T = 6.3 \times 10^{-4}$ (e) k_1 for spin up of APC, $T = 3.8 \times 10^{-3}$ (f) k_2 for spin up of APC, $T = 2.5 \times 10^{-4}$ (g) k_1 for spin down of APC, $T = 1.2 \times 10^{-3}$ (h) k_2 for spin down of APC, $T = 1.9 \times 10^{-4}$

Parallel (10^{-5})					Anti-Parallel (10^{-5})				
$L \setminus R(\uparrow)$	s	p	d_1	d_2	$L \setminus R(\uparrow)$	s	p	d_1	d_2
s	89	42	58	37	s	50	24	309	208
p	43	25	30	17	p	24	14	163	121
d_1	65	32	84	32	d_1	38	16	288	203
d_2	38	17	29	19	d_2	17	8	126	81
$L \setminus R(\downarrow)$	s	p	d_1	d_2	$L \setminus R(\downarrow)$	s	p	d_1	d_2
s	16	50	84	43	s	20	8	20	8
p	6	5	40	29	p	10	6	10	5
d_1	145	65	103	663	d_1	233	177	268	116
d_2	61	42	558	544	d_2	141	94	143	72

Table 4.1: Values of partial transmission P_{AB} in Γ -point from left to right lead. First column indicates for partial wave labels of left lead (incoming), first row is for right lead (out-going). Arrows indicate spin channel. Some values are much larger than others, indicating those scattering channels are dominating.

adopted with the smaller transmission values. One can clearly see that the scattering wave functions decay at different rates. For the points at the hot spots, the wave functions decay much more slower than the other ones. One can also find clear resonance features for these points at the plots of scattering wave functions(Fig4.5 a,c,e,g). Such oscillations superposed on the wave functions is due to atomic details of the interaction among the magnetic leads and the molecules. The transmission of the resonant cases is an order larger than the decaying cases. The above scattering states analysis reveals that the smooth background in the T-maps is contributed by the decaying waves, while the sharp hot spots are due to the resonant states. We should emphasize again that it is crucial to have proper BZ k-sampling in order to accurately capture these detailed but important features so that one can compare with measured data.

4.5.1 Analysis of spin injection

The chemical properties of octanethiolate are found to affect spin transport in substantial ways and determine how spins are injected. The main contribution to the DOS of bulk Ni at E_f is due to the spin-polarized d-waves. Octanethiolate is composed of CH_2 units connected by σ -bonds which are sp_3 hybridized orbitals. Therefore, the p-wave is more likely to propagate along the linear chain. For analysis purposes, we may consider that the interfaces between molecules and leads serve as scatterers that connect d- to p-waves. Quantitatively, we define a spin resolved *partial transmission* from Eq.(4.7), $P_{AB} \equiv \sum_{A,B} G_{b_1 a_1}^r(\Gamma_L)_{a_1 a_2} G_{a_2 b_2}^a(\Gamma_R)_{b_2 b_1}$ where A and B are wave labels of s, p, d_1 , d_2 , here $d_1 = d_{xy}, d_{yz}, d_{xz}$ and $d_2 = d_{x^2-y^2}, d_{r^2-3z^2}$. $a_{1,2} \in A$ are orbital indices for the left lead with label A ; $b_{1,2} \in B$ are for right lead with label B . The quantity P_{AB} measures the probability of an A -type wave in the left lead propagating to a B -type wave in the right traversing the molecule. To resolve this feature better, we choose the characteristic Γ -point, in which the transmission is one order larger than the average transmission over the whole BZ. Table 4.1 shows P_{AB} in Γ -point of our device where data larger than 30% of the maximum are highlighted in boldface. In PC, spin-up electrons are actually the minority carriers at E_f for Ni, their P_{AB} values are distributed into all types of orbitals, see upper-left block of the table. In clear contrast, the spin-down channel is dominated by the d-wave transmission, shown in lower-left block, corresponding to tunneling processes of majority d-waves. In APC, spin-up electrons are minority carriers for the left lead and majority carrier for the right. The contribution to the spin-up transport channel comes from all different waves in the left lead scattered into d-waves of the right lead, shown in upper-right block. The spin-down channel is given by majority (left) to minority (right) scattering, hence we observe d-waves from left scattering into all other waves of the right(see lower-right block).

These scattering processes suggest that spin injection can be tuned and controlled chemically through the molecules in the middle. The understanding of the nature of the molecule, the control of contact geometries, and the change of end-group might

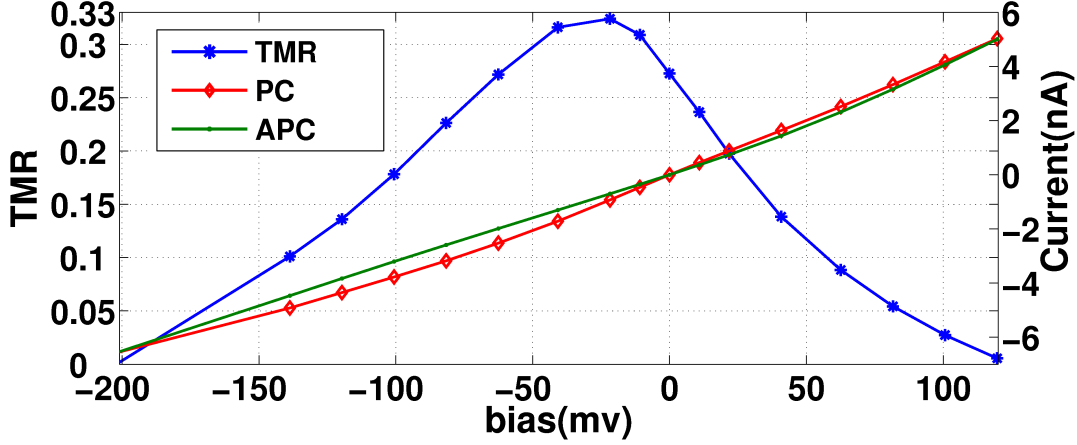


Figure 4.6: I-V curves (right axis) and voltage dependence of TMR (left axis). The solid line with diamond (red) and solid-dot (green) are I-V curves for PC and APC. The TMR-V curve (blue line with solid-star) peaks at -20mV with 33% and decays to zero at -200mV and $+120\text{mV}$.

all lead to great variabilities of spin-based transport properties in molecular MTJ. For instance one can imagine choosing molecular linkers so that d-waves are more efficiently scattered into p-waves. One of our recent unpublished results is based on this idea: in that work we investigated two different molecular MTJ, Fe/octane-dithiolate/Fe and Fe/octane-thiolate/Fe, respectively. With dithiolate end-groups, the MTJ produces a much larger TMR ($> 100\%$) than the one with thiolate end-group[29]. We are not going to discuss too much about the calculation of this system since the details are quite similar to the study of Ni/octanethiolate/Ni above. In some sense, the work introduced in this chapter will set a benchmark to make prediction of transport properties in molecular MTJs.

4.5.2 Spin polarized current and TMR

Using Eq.(4.6) we obtain the spin polarized current

$$I_{\sigma}(V_b) = \frac{e}{h} \int_{\mu_L}^{\mu_R} T_{\sigma}(E, V_b)(f_L - f_R)dE \quad (4.8)$$

where $\mu_{L,R}$ are electrochemical potentials of the left/right leads and $\mu_L - \mu_R = eV_b$, and $f_{L,R} \equiv f(E - \mu_{L,R})$ are the Fermi functions. We also explicitly indicated that T_{σ}

of Eq.(4.6) is actually a function of bias V_b . The total charge current is given by $\sum_{\sigma} I_{\sigma}$. Fig.4.6 shows the calculated I-V curve for PC and APC as well as TMR defined by the total currents. Recalling Eq. (4.1), $\text{TMR}=(I_{PC} - I_{APC})/I_{APC}$. At $V_b = 0$ when all the currents vanish, we compute TMR by the equilibrium transmission coefficient.

For our device, $I_{PC} > I_{APC}$ for the entire bias range $-200mV < V_b < +120mV$ we examined, giving rise to positive TMR versus V_b . TMR is asymmetric with respect to the polarity of V_b , in agreement with the experimental observation[16]. This asymmetry is due to the asymmetric atomic structure of the device: only one side of the molecule has the thiolate group. In fact, the effect of asymmetry is already seen in Fig.4.4c,d: if the system were symmetric, then for APC at zero bias, the spin-up and -down channels would have exactly the same transmission. The fact that Fig.4.4c,d are very different is an indication for the lack of symmetry. Quantitatively, we obtain a maximum TMR of 33% at $V_b = -20mV$. The experimental data shows a maximum TMR about 12% to 16%, at -15mV to -5mV (Fig.4c of Ref.[16]). The calculated TMR decays as a function of V_b asymmetrically: it vanishes at $V_b < -200mV$ or at $V_b > +120mV$ (see Fig.4.6). Experimentally[16], TMR also decays with bias asymmetrically but with voltage scales somewhat smaller than our theoretical values. Given the possible differences of atomic structure used in our theory and that in the experimental device, this level of quantitative consistency is, indeed, very satisfactory.

To understand why TMR decays with bias, we plot total transmission $T(E) = \sum_{\sigma} T_{\sigma}(E)$ versus energy E at four different values of V_b in Fig.4.7. The vertical lines indicate the bias window, *i.e.* integration range of Eq.(4.8). It is very clear that for small V_b , $T(E)$ for PC and APC are rather different in the bias window, see Fig.4.7a and Fig.4.7b. As $|V_b|$ is increased to larger values, the difference is reduced as shown in Fig.4.7c,d. Such a reduction is related to the DOS of Ni leads, it causes TMR to reduce with V_b . It is well known that there is a sharp peak in minority DOS (spin-down) near the E_f of Ni, see inset of Fig.4.7b. At low bias, this DOS peaks of left/right leads align, leading to a larger total transmission for PC than for APC, hence a larger TMR. As $|V_b|$ is increased, the DOS peaks of leads are shifted away

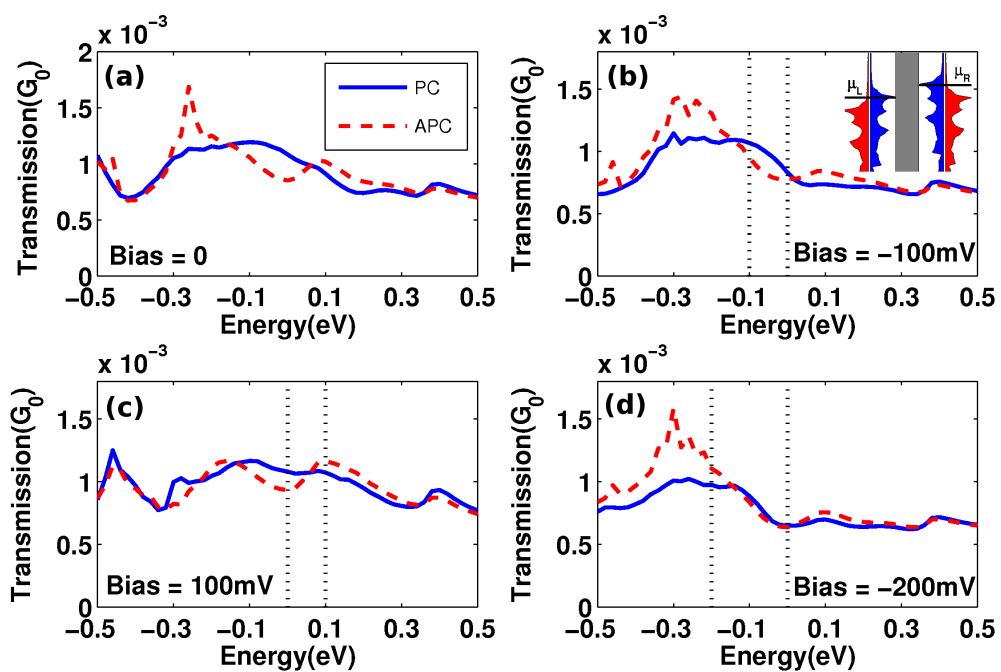


Figure 4.7: The four panels are total transmission $T(E)$ versus energy E for PC (solid blue line) and APC (dashed red) for four different V_b . The difference of PC and APC transmission within the energy window (marked by two dotted vertical lines) reduces for increasing $|V_b|$. Inset in (b): DOS of the Ni leads.

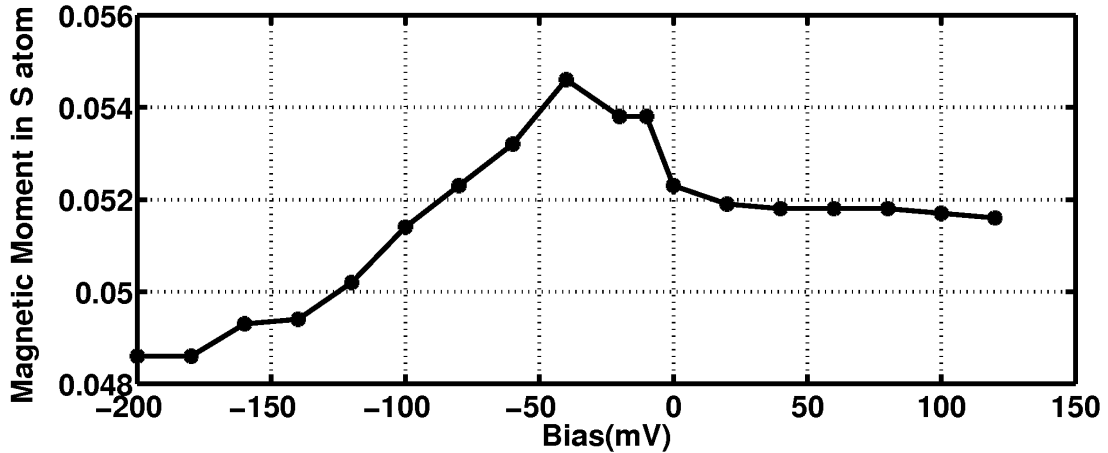


Figure 4.8: The bias-dependent magnetic moment(= $Charge_{\uparrow} - Charge_{\downarrow}$) in sulphur atom of Ni/alkanethiolate/Ni junction for parallel configuration. It shows the proximity effect to the magnetic leads.

from each other so that the difference of transmission in PC and APC is reduced. $T(E)$ in the bias window has a major difference in terms of polarity of V_b . Namely, at $V_b = +100\text{mV}$ the PC and APC difference is already very small; but at $V_b = -100\text{mV}$ this difference is still substantial. This gives the asymmetrical TMR versus V_b . As discussed above, the asymmetry versus V_b is due to asymmetry of the device: the left has Ni-S chemical bond while the right does not. Our calculation reveals that due to proximity effect, the S atom develops a small magnetic moment variation in the range of a few percent of a Bohr magneton. As shown in Fig.4.8, the induced magnetic moment of S has a bias dependence similar to that of the TMR curve in Fig.4.6 and clearly affects spin transport.

4.6 Summary and outlook

In this chapter, we presented a brief review of spintronics. Concepts related to spin transport such as magnetoresistance are introduced in detail. As the overlap of spintronics and molecular electronics, molecular spintronics calls for attention both experimentally and theoretically. A NEGF-DFT based first-principles calculation showed its ability to make quantitative predictions that can be directly compared with exper-

imental measurements. Due to our very careful analysis in terms of the k-sampling, basis sets, and atomic structures, our results in this chapter provide a benchmark for further theoretical calculations. The transport properties of molecular spintronics depends sensitively on the chemical details of the molecule and, in our case, on how d-waves from a Ni lead are scattered into p-waves of the molecule before exiting to the second Ni lead. At the present stage of molecular spintronics research, we believe our quantitative consistency in many aspects with the measured data is rather satisfactory and provides a starting point to resolve the remaining differences. For example, more accurate functionals such as PBE[44] can be used to recalculate the electronic structures and transport, and compare with our data presented here. More careful treatments of the contact structure will tell us how sensitive the spin-dependent transport is related to the atomic details there. In a larger picture, our technique used here is actually very general and can be applied to study other kinds of MTJs such as the more conventional solid state MTJs[115].

Transport in molecular wires: the role of contacts

Due to the phenomenal growth of experimental efforts in molecular nanoelectronics[9, 26, 116, 117], it has now been well established that electric conduction on the molecular scale is sensitively related to the atomic properties of the nano-structure: small variations of these properties can give rise to significant changes of conductance[118]. For some reason systematic theoretical studies of the role of atomic contact structures in molecular junctions have not been done to any satisfactory fashion. Perhaps there are simply too many possibilities that might influence electronic transport in molecular junctions and investigating contact structure is tedious, time consuming and theoretically less “glorious”. Indeed, if a serious discrepancy between theory and experiment is found, many of us are inclined to consider what has been missing in the theoretical formalism, for instance the intrinsic limitation of practical DFT, the lack of self-interaction correction (SIC), the absence of image potential, and the approximation associated with the exchange-correlation terms. These issues are more interesting to pursue from a theory point of view.

Therefore, there have been considerable efforts in the literature to create sophisticated “beyond DFT” calculation methods for molecular electronics[119, 120]. Unfortunately, due to complicated technical issues, different approximations and/or even adjustable parameters must be introduced in these beyond-DFT methods. For instance, the SIC method[119] involves an adjustable parameter whose value depends on the research problem and is an input to the calculation; the configuration interaction (CI) method[120] involves some rather *ad hoc* treatment of the device leads as

well as the coupling of the device to the leads. By adjusting some parameters or tuning the model, one may be able to narrow down the theory-experiment discrepancy in one particular case, but usually the parameters need re-adjustment when moving to a new problem. This is not very satisfactory at all. Still, we fully recognize that these are important efforts for the theory community to repair some of the approximate issues of the NEGF-DFT formalism and they may lead to future developments and breakthroughs.

Going back to the literature[119, 120], we discover that the main motivation for developing the beyond-DFT methods was the huge discrepancy between calculated and measured conductance of the Au/BDT/Au molecular wires. Here BDT stands for the molecule benzenedithiol. Indeed, even though the NEGF-DFT formalism has achieved a lot of successes in quantitative predictions of quantum transport in molecular electronics, it failed spectacularly when applied to predict conductance of the Au/BDT/Au. In particular, existing NEGF-DFT calculations predicted a conductance that is at least 50 times larger than the measured one. This problem has caught a wide theoretical attention [119, 120, 121, 122, 123, 124, 125], but the reason for the failure was unclear up to now.

It is puzzling why NEGF-DFT fails at the seemingly simple Au/BDT/Au device while it worked well for many other more complicated systems. We therefore believe there should be a simple reason which has escaped attention of the theorists. Hence, before making a judgement whether or not there is an important missing ingredient in the NEGF-DFT formalism such that one should go-beyond it for this problem, we believe it is prudent to first seriously consider what is the most basic issue. In our view, atomic structures, especially the contact structures, are the most basic issues since they play important roles in electronic conduction.

In this Chapter, we will investigate the contact formation and electronic transport in various molecular junctions including the Au/BDT/Au, Au/benzene-diamine(BDA)/Au, Au/amine-benzene-thiol (ABT)/Au. The Chapter is organized as follows. First, we shall focus on the system of Au/BDT/Au and Section 5.2 reviews the experimen-

tal and theoretical efforts on this device. The details of our systematic studies are presented in Section 5.3. According to our extensive first-principles total-energy calculations, it was found that a BDT molecule prefers to attach to ad-atoms when it is bonded to Au(111) and, much more importantly, the hydrogen atoms on the thiol groups of a BDT do not dissociate after the formation of the device contacts. Essentially all previous calculations in the literature followed a well established perception that hydrogen is dissociated from the -SH group of the thiol after BDT is adsorbed to Au(111) surface, namely the contact structure of the BDT on Au(111) has always been assumed to be hydrogen-dissociated (HD-model). It is striking to find that the old perception of dissociation of H from -SH bond of BDT at the Au/BDT interface is questionable. The total energy calculation clearly shows that the non-dissociated H in -SH bond is energetically more stable than the H-dissociated model. In order to further check the validity of this new contact structure where the hydrogen is non-dissociated (HND-model), we have also calculated the break-down force and bonding-energy of the Au-SH (Au-S) bond. We found that results from the HND-model achieve satisfactory consistency to experimental measurements while those from the HD-model do not. In particular, the HND-model gives a conductance that is as close as a factor of 2 to the measured data, while that from the HD-model is at least one order of magnitude larger than the experimental data. Further analysis of scattering states provides a clear understanding to the mechanism of electron transport through the Au/BDT interface. Our results strongly suggest that the newly discovered HND-model most likely describes the contact structure of the Au/BDT/Au devices.

There is an experimental possibility[2] that during the contact formation process, the proton in the hydrogen atom of the SH-group will dissociate leaving a negative charge on the S atom. To investigate such an ionic-type contact, in Section 5.4 we calculate transport properties of Au/BDT/Au junctions with charged bonding structure. After introducing the ionic-type atomic configurations of S and H in the -SH bond, the physical picture of charge transfer in these systems shows consistency with

the HD/HND models. The calculated results on the charged systems also strongly suggest that the HND-model is the most likely one to explain the present experimental measurements[2, 25, 126].

In Section 5.5 we shall further explore the idea established in Section 5.3 to a series of molecular junctions. Again, the results clearly demonstrate the important role played by contact structures for electron transport in molecular wires.

5.1 *The Au/BDT/Au: background*

As already mentioned above, it has been quite puzzling why theoretical predictions of the conductance of Au/BDT/Au device are much larger than the experimentally measured values. In this Section we review the existing literature on this problem.

5.1.1 *Experimental measurements*

Measurements of conductance of single molecules require a good control over the microscopic contact structures between the molecule and electrodes. This poses a substantial challenge to the experiments. In the past decade, several techniques have been employed to fabricate metal-molecule junctions.

Mechanically Controllable Break Junctions (MCBJ). In 1997, Mark Reed and his colleagues measured the conductance of Au/BDT/Au junctions using the MCBJ technique[23]. The measured conductance was rather small: $6 \times 10^{-4}G_o$ where $G_o = 2e^2/h$ is the conductance quantum. It was the first time that conduction of a single molecule was measured. In the MCBJ technique, a metallic wire is stretched and broken by bending the substrates underneath the wire, forming two gold contacts. BDT molecules flowing around in the system may stochastically attach to the gold surface and form a self-assembled monolayer (SAM) of BDT. The two gold contacts are then moved toward each other until the onset of conductance happens. Even though the Au-Au gap in the MCBJ can be controlled experimentally, it is impossible to control the detailed atomic structure at the molecule-lead contact and it is difficult to discern how many molecules, or even if there are any molecules there to bridge

the Au-Au gap. When a conductance is measured, it is impossible to know if the quality of the molecule-lead coupling is good or not. For these reasons, the reported results[23] were not reproduced by other groups. Finally, in 2008, a group in Germany reported the measurement of a Au/BDT/Au junction by MCBJ, obtaining even lower conductance of $5 \times 10^{-5}G_o$ [127]. Since the BDT molecule has an extended electronic π state and the Au-S bond is very strong, one would expect much larger conductance. Hence, so far these very small conductances were not really understood and have been theoretically attributed to strong Coulomb repulsion[119, 120].

STM break junctions. Motivated by the earliest measurement of single molecule conduction, Tao *et al.* reported an experimental investigation of electron transport of the BDT device[2] in 2003 using a STM break junction technique. In their experiments, a gold scanning tunneling microscope (STM) tip was repeatedly moving into and out of contact with a gold substrate, creating a nano-scale Au-Au gap. Stochastically, BDT molecules may move into the gap and bond to the two Au surfaces forming a Au/BDT/Au molecular wire. By creating and measuring thousands Au/BDT/Au transport junctions, the mean equilibrium conductance was found to be $0.011G_o$ [2]. Even though the statistical width surrounding the mean was rather large, several peaks were clearly identified in the statistical spectra of the measured conductance ensemble[2], and these peaks were at integer multiples of the fundamental mean value $0.011G_o$. The interpretation is that multiple BDT molecules bridging the Au-Au gap should give multiple values of the single molecule conductance which is taken to be $0.011G_o$. This value is much larger than those measured by the MCBJ technique[23, 127], presumably because STM controls the Au-Au gap better than the MCBJ technique.

Lithography and electromigration. Most recently, another novel method combining electron-beam lithography (EBL) and electromigration (EM) to fabricate metallic electrodes with nanometer separation, was used to measure the conductance of BDT[25]. In the experiment[25], a gold wire was broken by electromigration to produce a nano-meter gap in the wire. A molecule such as BDT may bridge the gap and

Method	Environment	Conductance	Time
MCBJ	Vaccum	$6 \times 10^{-4} G_o$ [23]	1997
STM tip	Solution	$0.011 G_o$ [2]	2003
STM tip	Solution	$4 \times 10^{-3} G_o$ [129]	2006
EBL& EM	Vaccum	$0.01 G_o$ [126, 128]	2006,2008
MCBJ	Vaccum	$5 \times 10^{-5} G_o$ [127]	2007
EBL& EM	Vaccum	$0.013 G_o$ [25]	2009

Table 5.1: Experimental measurements of Au/BDT/Au junction.

form an Au/BDT/Au single molecule transport junction. This method shows good electrical and mechanical stability. The equilibrium conductance was measured[25] to be $0.01 \sim 0.015 G_o$, giving an average value of $(0.0132 \pm 0.0021)G_o$. Using a similar electromigration technique, a Japanese group also reported the conductance of Au/BDT/Au junction to be around $0.01 G_o$ [126, 128]. This newly-measured conductance therefore confirms the value obtained by the STM method of Tao *et al.*[2].

In Table 5.1, we list the representative experimental measurements of the conductance of Au/BDT/Au in the past decade. The measured conductance shows consistency around $0.01 G_o$. Such a consistency on devices fabricated by totally different methods and environments indicates that a long-standing goal of achieving experimental data convergence for the most well known molecular device, Au/BDT/Au, is likely reached. This is important because it indicates that, finally, reproducible data can be obtained in single BDT molecule devices. The experimental convergence of transport data for the Au/BDT/Au device provides a timely opportunity to qualitatively and quantitatively understand the physics of the electronic transport in this type of molecular junctions.

5.1.2 Theoretical analysis

Quantitative analysis of the Au/BDT/Au system have so far produced controversial results and failed to reach a consensus: the calculated conductance spread over one to

Method	Conductance	Time
Jellium model	$0.03G_o$ [130]	2000
NEGF - DFT	0.01-0.5 G_o , using 1-D lead[121]	2003
Jellium model	0.003-0.058 G_o , different adsorption sites[131]	2004
NEGF - broading DOS	0.01-0.04 G_o depending on basis[132]	2004
Wigner function + CI	$6.5 \times 10^{-4}G_o$ [120]	2004
NEGF - DFT	0.002-0.8 G_o , different configurations[122, 123, 124]	2004,05,07
NEGF - HF, Au cluster leads	$4 \times 10^{-4}G_o$ [133]	2005
NEGF - DFT	0.04-0.6 G_o different configurations[134]	2006
NEGF - DFT	0.2-0.8 G_o for different Au-S distance[135]	2006
NEGF - LDA+(SIC)	0.11-0.7 G_o (LDA), 0.03 – 0.1 G_o (LDA+SIC)[119]	2007
NEGF - extended Huckel	$0.008G_o$ [136]	2008
NEGF - DFT(PW)	$0.28G_o$ [125]	2008

Table 5.2: Theoretical calculations of the conductance Au/BDT/Au/ junctions.

two orders of magnitude depending on the atomic models and/or theoretical methods, as shown in Table 5.2. In particular, even though the NEGF-DFT first principles formalism was able to make many satisfactory predictions to quantum transport which were favorably compared with experimental data[26, 28, 137, 27, 138], it failed when applied to the Au/BDT/Au devices.

In our view, the atomic structures of the fabricated molecular devices were actually unclear. In particular, the most important structural information - the metal-molecule contacts, is at best ambiguous for essentially all single molecule transport junctions investigated in the literature. In theoretical analysis of molecular devices, one usually assumes an initial metal-molecule contact structure - guided by intuition or by experiments, and then relaxes the structure. However, experimentally when a molecule is brought to contact with the metal leads, a contact formation occurs where chemical reactions may give rise to dissociation or formation of atomic groups from the original molecule. Such a process is likely lost when an initial atomic configuration is *assumed* without carefully considering it from *ab-initio* point of view. Full molecular dynamics simulations may capture the formation process, it is, however, prohibitively expensive

for computation due to the relatively long time-scales of contact formation process and large system sizes. As a result, the formation process has not been subjected to systematic investigations so far and, as we show in this thesis, it is a crucial effect that controls the interface transparency to charge flow. In particular, it determines the value of conductance for a Au/BDT/Au device.

The electronic transport through a molecular junction includes three regions: the left/right interface and the molecule itself. The total transmission coefficient T of the system can be thought of as composed by transmissions T_L/T_R of the left/right interface and T_m of the molecule. Clearly, for systems with large T_m , the interface contributions T_L/T_R become important. But for systems having very small T_m , the contact transparency becomes less important in determining the overall conductance of the device. For instance, the popular Au/alkanedithiol/Au molecular wire has a very small T_m because transport is dominated by electronic tunneling through the localized σ -bonds of the alkane[110, 111]. In other words, the huge resistance (typically tens or hundred mega-Ohms) of Au/alkanethiol/Au is dominated by the length of the alkane molecule and not by the Au/alkanthiol interface. Therefore theoretical calculations of the Au/alkanethiol/Au are generally comparable to experimental measurements within the same order of magnitude[26] even though one may not have treated the contact region most carefully. The situation of the Au/BDT/Au device is very different from the Au/alkanedithiol/Au. The benzene ring in BDT consists of a non-local π -bond system which is more transparent to electron conduction than the σ -bond of alkane-molecules. Therefore, the conductance of Au/BDT/Au junctions should be much more sensitive to the contacts, particularly, to the bonding structure at the Au/BDT interface[118]. We therefore believe a careful study of the Au/BDT interface should be a good starting point.

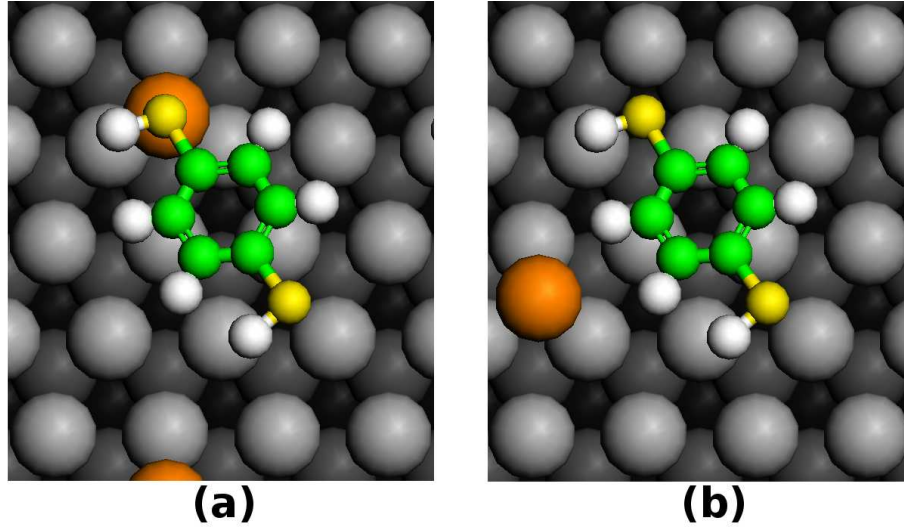


Figure 5.1: Top view of the configuration of BDT adsorption to the Au(111) surface. (a) BDT attaches to the surface via the Au adatom. (b) BDT attaches to the surface directly while a Au adatom is also on the surface but sitting aside.

5.2 Calculation of the Au/BDT/Au junction

5.2.1 Total energy structural relaxation

We use a standard DFT-PAW method with the Perdew-Burke-Ernzerhof 96 functional (GGA-PBE)[44] as implemented in the electronic structure package VASP[58] to determine the atomic structure. A $c(4 \times 3)$ super-cell consists of six layers of Au atoms separated by a vacuum layer of 15 \AA was adopted to model the surface in Au/BDT interface, as shown in Fig.5.1. All atoms except the three bottom Au layers were fully relaxed with a force criterion of 0.02 eV/\AA applied for every atom. A planewave cutoff of 400 eV and a k-mesh of $4 \times 4 \times 1$ were applied, and we further checked them by a cutoff of 500 eV and a mesh of $8 \times 8 \times 1$ to ensure the convergence to 1 meV/atom . The cross-section in our two-probe device calculation is the same as in the interface calculations, shown in Fig.5.7.

As suggested by a recent STM experiment[139], thiol molecules prefer to attach to a Au(111) surface through Au ad-atoms. We have therefore calculated BDT absorption on Au(111) with and without Au ad-atoms. Particularly, we calculated two different cases as shown in Fig5.1. In one case (case-1), BDT is absorbed to the

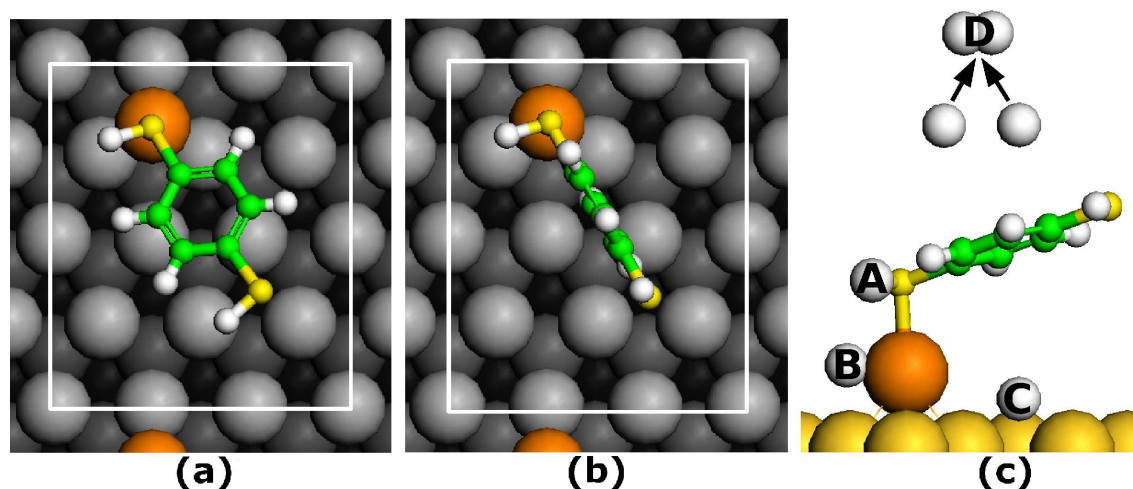


Figure 5.2: Top views of examples for (a) parallel and (b) perpendicular configurations. (c) Four positions of H have been considered for each configuration at several orientations: (A) is for non-dissociated H; (B,C,D) are for dissociated H which attaches to the (B) ad-atom, (C) the surface, or (D) escapes into vacuum forming an H_2 molecule.

surface directly while the adatom is on the surface. In another case (case-2), BDT is absorbed to the surface via the adatom. The total energy calculation shows that the structure in case-2 is energetically more stable than in case-1. The difference of bonding energy is at least 0.4 eV per molecule. Based on the fact of adatom preference suggested by the STM experiment[139] and our total energy calculation above, in the next step, we investigated a series of representative atomic configurations with BDT molecules absorbed on Au(111) surface via Au ad-atoms. Figure 5.2(a,b) plot two initial structures of the BDT attached to Au(111) via an ad-atom, these initial structures where the molecule is parallel or perpendicular to the Au(111), are used for structural relaxation. According to the C3 rotational symmetry of Au(111), another two sets of these structures with a rotation angle of -30° or 30° were also considered. Together these should cover most of the initial likely configurations. For contact formation, we consider three cases for the hydrogen dissociative (HD) configuration: the dissociated H atom attaches to the ad-atom (HD-adatom), to the surface (HD-surface), or escapes to vacuum to form an H_2 molecule (HD-vacuum), as shown in Fig. 5.2(c). Note that in the HD-vacuum case, the total energy should count in the formation energy of an H_2 by two escaped H atoms since it is much more stable

	parallel			perpendicular		
	0 ⁰	30 ⁰	60 ⁰	0 ⁰	30 ⁰	60 ⁰
HND	0.00	0.09	0.08	0.06	0.06	0.06
HD-adatom	0.28	0.25	0.61	0.53	0.54	0.42
HD-surface	0.41	0.40	0.42	0.40	0.41	0.41
HD-vacuum	0.24	0.25	0.26	0.25	0.25	0.24

Table 5.3: The difference of total energies (units eV) compared to the the most stable structure (the parallel 0⁰) for typical configurations of Au/BDT interface. For all situations, the H-non-dissociative structures have lower energies.

than a sole hydrogen atom. The calculated total energies are summarized in Tab. 5.3. It is striking to find that configurations with non-dissociated S-H bonds, (first row in Table 5.3) are always energetically more stable than the other H-dissociated structures by at least 0.2 eV per BDT for all the investigated systems. In fact, the non-dissociative S-H bond in thiol group absorbed on a perfect Au(111) surface was experimentally observed by Yates *et al.*[140] and more recently confirmed by *ab-initio* calculations[141].

These results strongly suggest that an H-non-dissociative (HND-model) structure should provide a more realistic model in terms of transport modeling of the Au/BDT/Au devices. Nevertheless, we caution that for discussions of thermal stability, one should use the Gibbs free energy instead of the total energy as we have done so far. Gibbs free energy includes the internal energy (total energy obtained from DFT), the entropy, and the mechanical work. How much the latter two factors will contribute to thermal stability is ambiguous. In this sense, both HND-model and HD-model are probably possible in real Au/BDT/Au molecular junctions, although the HND-model is energetically more stable by 0.2 eV according to the calculated total energy. Additional theory-experiment comparisons are, therefore, valuable in showing the preference between these two models, as shown in the next two subsections.

5.2.2 Junction breakdown force

Having established that the total energy of the HND-model is lower than HD-models, in this subsection we investigate the junction breakdown forces. In the original experiment of Tao *et al.*[2], an Au tip was retracted after contacting the Au(111) surface in order to form the Au/BDT/Au junction. Tao *et al.* further measured the junction breakdown forces of the formed Au/BDT/Au structures[142]. Since the S-Au bond is much stronger than the SH-Au bond, by calculating the junction breakdown forces and comparing with the measured data, we can distinguish which bond is more likely. This provides an additional consistency check of the total energy results of Section 5.2.1.

Our calculation includes three parts: (i) Contact evolution in the HND-model; (ii) Breakdown force in the HND-model; (iii) Breakdown force in the HD-model. Here, (i) involves a first-principles modeling of structural evolution by elongating the Au/BDT/Au junction from a compressed configuration to the final one where the junction is just broken-down. (ii) calculates the breakdown force in the HND-model. (iii) the same as (ii) but on the HD-model and results compare to that of the HND-model. Our calculated breakdown force in comparison to the experimentally measured value, strongly suggests that the HND-model gives a more reasonable description for the contacts in Au/BDT/Au, consistent to the total energy analysis of Section 5.2.1.

Structural evolution in the HND-model

A series of HND-model Au/BDT/Au junctions having different junction lengths shown in Fig. 5.3, are considered. The junction length L in Fig. 5.3 is defined by the gap between the surfaces of the left and right leads at their initial configuration. The positions of the adatoms along the transport direction (z direction) at left and right leads is denoted by L_L and L_R respectively, which are determined after the atomic coordinates are fully relaxed. Both L_L and L_R are measured from the adatom to the third layer Au counted from the lead surface, as shown in Fig. 5.3(a). The third Au layers of the left/right leads and the layers beyond them are fixed during structural relaxation which provides a good reference for evaluating L_L and L_R . The

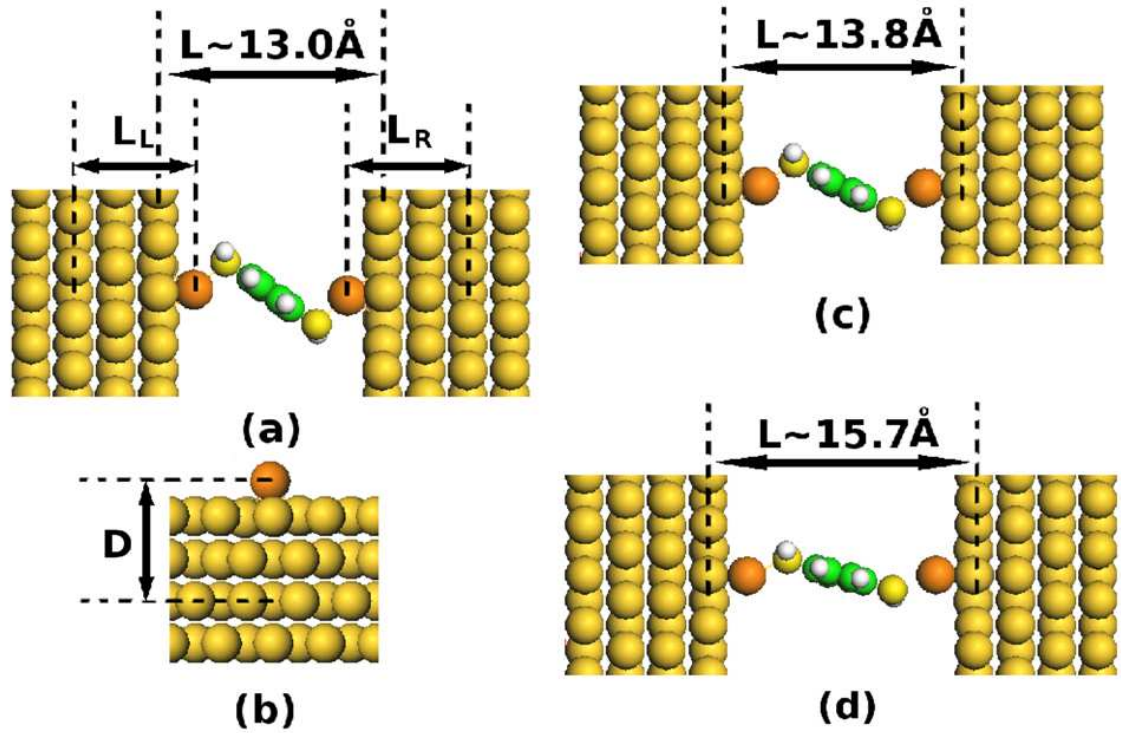


Figure 5.3: Fully relaxed configurations for H-non-dissociative junctions: (a) at $L = 13.0 \text{ \AA}$, in which $L_L = 6.846 \text{ \AA} \approx L_R = 6.849 \text{ \AA}$, very close to the D value of an adatom on a bare surface; (b) a surface that an adatom attaches to a bare Au(111) surface, where $D = 6.846 \text{ \AA}$; (c) the junction is at its equilibrium, when $L = 13.8 \text{ \AA}$, in which $L_L = 6.935 \text{ \AA} \approx L_R = 6.933 \text{ \AA}$; (d) the junction starts to break at $L = 15.7 \text{ \AA}$, $L_L = 7.101 \text{ \AA}$, $L_R = 7.052 \text{ \AA}$.

distance D (see Fig.5.3(b)) has a similar definition as that of L_L or L_R , but it is for a single surface - not a surface inside a two-probe junction.

The initial structures shown in Fig. 5.3 were relaxed by DFT total energy calculations. The positions of all ions, except the four outermost layers (two in left and two in right leads), are fully optimized until the net force acting on them is less than 0.01 eV/Å, using the same method as in Section 5.2.1, i.e. PAW-PBE implemented in the VASP package[58]. During the stretching of the two-probe junction, one Au lead was moved step by step with a minimum step length of 0.1Å. A total of 22 configurations have been calculated from $L=12.7$ Å to 15.8 Å which covers the length ranging from the compressed to the breakdown junctions.

The calculated total energy of the two-probe junction versus junction length L is shown in Fig. 5.4(a). It becomes lower as the junction is stretched further and reaches a minimum value at around $L = 13.8$ Å. This value of L is regarded as the equilibrium length of the junction. The equilibrium geometry is shown in Fig. 5.3(c) in which the Au-SH bond length is 2.43Å and the L_L (L_R) is 6.94 Å. Close to $L = 15.7$ Å (structure shown in Fig. 5.3(d)), the junction starts to break which can be identified from either geometric or energetic points of view. In terms of energetics, the total energy essentially remains constant from 15.7Å to 15.8Å indicating the junction is breaking.

Table 5.4 shows that L_L and L_R are fairly similar before L reaches 15.6 Å. However, an appreciable difference of 0.05 Å between them becomes observable at $L=15.7$ Å, and it becomes 0.08 Å for $L=15.8$ Å. Both the Au-S bond length (left lead) and the L_R value start to decrease at $L=15.7$ Å. These geometrical changes are consistent with the features of a junction breaking down, consistent with the energetic behavior.

It is remarkable that the values of L_L (6.846Å) and L_R (6.849Å) in the configuration for $L = 13.0$ Å are quite close to that of a bare single surface, denoted as D (6.846 Å). It implies that the absolute tension applied to the adatom in the z direction should be the smallest (close to zero) when the junction length is around 13.0 Å.

L	12.7	12.8	12.9	13.0	13.1	13.2	13.5	13.6	13.7	13.8	13.9
L_L	6.823	6.834	6.841	6.849	6.854	6.866	6.903	6.915	6.930	6.935	6.946
L_R	6.817	6.833	6.838	6.846	6.857	6.874	6.900	6.910	6.917	6.933	6.942
Au-S(L)	2.426	2.426	2.422	2.420	2.418	2.419	2.422	2.421	2.423	2.425	2.429
Au-S(R)	2.430	2.429	2.425	2.422	2.421	2.422	2.422	2.421	2.423	2.427	2.429
L	14.0	14.1	14.2	14.7	15.2	15.3	15.4	15.5	15.6	15.7	15.8
L_L	6.958	6.968	6.979	7.030	7.078	7.087	7.094	7.095	7.101	7.101	7.103
L_R	6.953	6.965	6.977	7.035	7.078	7.093	7.098	7.100	7.093	7.052	7.023
Au-S(L)	2.431	2.434	2.439	2.474	2.535	2.543	2.562	2.567	2.568	2.539	2.534
Au-S(R)	2.434	2.435	2.442	2.476	2.534	2.572	2.592	2.638	2.704	2.886	3.017

Table 5.4: Changes of L_L , L_R , and Au-SH bond lengths at the left (Au-S(L)) and right (Au-S(R)) leads in the HND-model. All values are in Angstrom. Here L , L_L , L_R are defined in Fig 5.3. L is defined by the gap between the surfaces of the left and right leads at their initial configurations. L_L/L_R are defined by the distance of left/right adatom to the the third layer of the left/right Au surface.

The breakdown force of HND-model

The junction breakdown force is defined as the difference of the measured forces acting on one lead of the junction just before the breakdown starts and after the breakdown completes. The forces were experimentally recorded from atomic force microscope (AFM) tips in the AFM-Molecule-Surface setup for the Au-S linkers[142].

In our calculations, two methods were employed to determine the changes of tension with respect to the junction elongation. These two methods are: (i) We derive the force from total energy of the elongating junction and, (ii) we directly calculate the force according to the shift of the Au adatom. In the first method, the tension of the junction is derived by $F_{Junction} = dE/dL \approx \Delta E/\Delta L$. Figure 5.4(b) plots the calculated $F_{Junction}$ versus L , where its value at $L=13.8 \text{ \AA}$ (the equilibrium junction length) is zero. The largest positive value of this force is shown in the figure, i.e. 0.76 nN, but the lower limit of negative forces is somewhat ambiguous. As discussed in the last section, when $L = 13.0 \text{ \AA}$, the values of L_L and L_R are very close to that of D (of a single surface) at equilibrium. It is therefore quite reasonable to use that junction length as a reference in estimating the lowest negative force. The force of the junction with $L = 13.0 \text{ \AA}$ is -0.34 nN as shown in Fig. 5.4(b), we thus obtain a

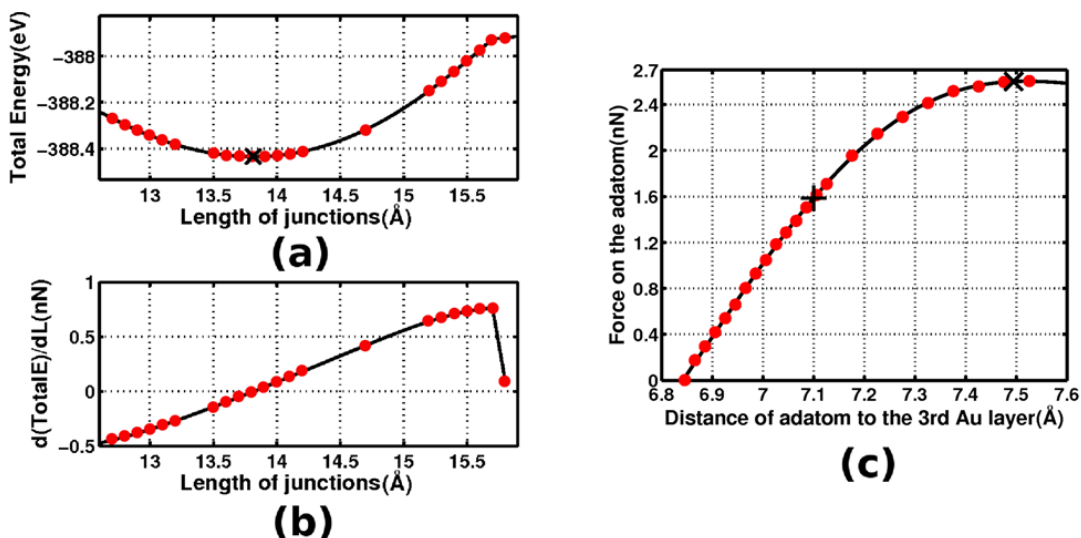


Figure 5.4: Calculated (red dots) and fitted (black lines) data for H-non-dissociative junctions of: (a) total energies of the junction with different lengths, the cross indicates the equilibrium position; (b) derived force from (a) according to equation $F_{\text{Junction}} = dE/dL \approx \Delta E/\Delta L$; (c) calculated force (by the second method) which is acted on the adatom at non-equilibrium positions in the transport direction, the largest likely D value obtained from the H-non-dissociative junction elongation is marked by a plus sign; that from the H-dissociative junction elongation is marked by a cross sign.

breakdown force of 1.10 nN.

The second method is to compute the force according to the vertical position of an adatom on a bare single Au surface. After breakdown of a two-probe junction, the adatom of the left or right surface (without molecules attached) is retracted from its longest stretching position to its equilibrium position on the two surfaces. At the equilibrium position, the tension is zero by definition; while at the longest stretching position just before breakdown starts, i.e. at $L = 15.6 \text{ \AA}$ from Table 5.4, the force can be directly evaluated. The breakdown force is thus equal to the acting force directly calculated from the adatom on a bare surface in the z direction, in which the D is increased to match L_L or L_R of the junction at $L = 15.6 \text{ \AA}$. Table 5.4 shows that $L_L \approx L_R \approx 7.10 \text{ \AA}$ at that L , our calculation gives a value of breakdown force of 1.58 nN with $D = 7.10 \text{ \AA}$, as shown in Fig. 5.4(c).

The two methods for calculating breakdown force introduce some small uncertainty either to the minimum or to the maximum tension due to the HS-Au bonding (e.g. charge redistribution), but in different ways. For the first method, the calcu-

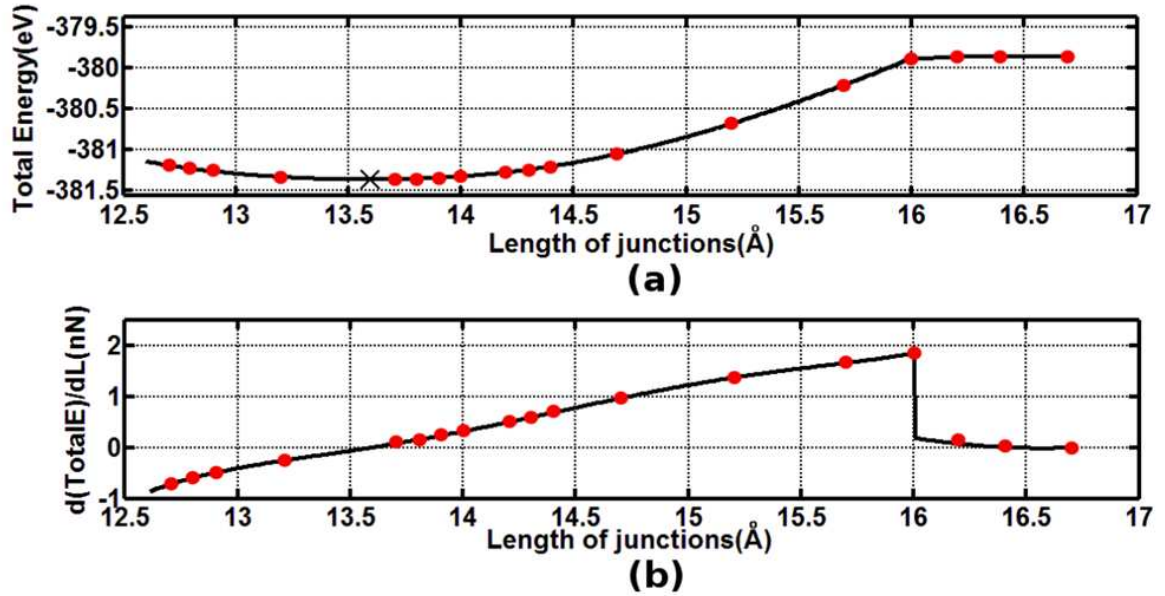


Figure 5.5: Calculated (red dots) and fitted (black lines) data for H-dissociative(HD) junctions of: (a) total energies of the junction with different lengths, the cross indicates the equilibrium position; (b) derived total energy (presenting force) according to equation $F_{\text{Junction}} = dE/dL \approx \Delta E/\Delta L$;

lated tension before the junction breakdown is exact within the DFT technique; but this tension is underestimated after the junction breakdown because the first method included the HS-Au bonding that tends to somewhat lower the breakdown force. For the second method the situation is opposite, namely it overestimates the breakdown force without considering the influence of HS-Au bonding at the longest stretching position before the breakdown. These considerations imply that the correct theoretical value should be in between the values obtained by our two methods, i.e. in the range between 1.10 nN to 1.58 nN. This result is consistent with the experimental value, i.e. 1.6 ± 0.2 nN, of another molecule (alkanedithiol) connected to Au leads through the same thiol linker[142].

The breakdown force of HD-model

We also evaluated the breakdown force of the H-dissociative model, following the same procedure. Figure 5.5(a) shows the evolution of total energy as a function of junction length (L) in an elongation process of the HD-model junction. Its derivative

curve, representing the tension of the junction ($F_{\text{Junction}} = dE/dL \approx \Delta E/\Delta L$) as a function of L , is shown in Fig.5.5(b). The zero value of the tension locates at $L=13.6$ Å, while the largest positive value is clearly shown in the figure as 1.85 nN. The lowest negative force was determined using the same idea adopted in the last subsection. The values of L_L and L_R are very close to that of D (of a single surface) at equilibrium, when $L = 12.8$ Å. At that L , the force is found to be -0.59 nN as shown in Fig.5.5(b). Therefore, a breakdown force of $1.85 \text{ nN} + 0.59 \text{ nN} = 2.44 \text{ nN}$ is obtained for the HD-model. The adatom-to-surface distance at the longest stretching position (at $L = 16.0$ Å), just before breakdown starts, must be ascertained so that the breakdown force can be estimated using the second method discussed in the last subsection. It was found that, according to the fully relaxed atomistic structure, $L_L \approx L_R \approx 7.495$ Å at that L (16.0 Å). The force calculated using the second method discussed above is 2.60 nN when $D = 7.495$ Å, as shown in Fig. 5.4(c) indicated by a cross.

In summary, the calculated breakdown force for the HD-model junctions, in the range from 2.44 nN to 2.60 nN, is significantly higher than the experimentally measured value of the thiol-gold linker[142] which is 1.6 ± 0.2 nN. On the other hand, the calculated breakdown force for the HND-model junctions are found in between 1.10 nN and 1.58 nN which is more consistent with the measured value. These results suggest that the HND-model gives a more reasonable description of the contact formation in Au/BDT/Au experiments[2, 25, 126, 128].

5.2.3 Bond Energies

As another important support to the HND model, we calculated the bond energies of Au bonded to -SH (or -S) and -NH₂ groups. The idea of this calculation is motivated by a recent experiment[143] which reported a measured conductance of Au/BDT/Au junction to be $0.01G_o$ [126, 128]. They measured three different types of molecular junctions with Au electrodes: amine-benzene-thiol(ABT), BDT, and benzene-diamine(BDA), using lithographically defined MCBJ techniques. By comparing the contact stability of these three junctions, they have evaluated the bond energies of Au-SH (or -S) and Au-NH₂. The bond energy of Au-NH₂ is 0.69 eV which

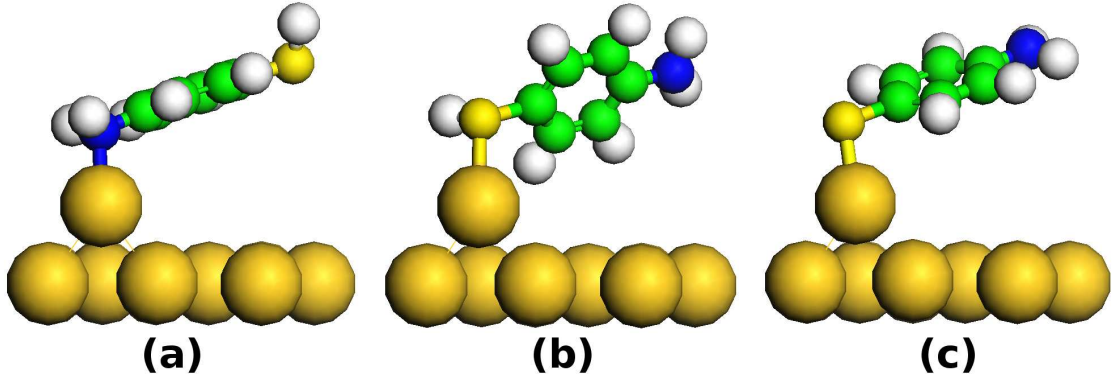


Figure 5.6: The molecule NH_2 -benzene-SH attaches to the Au(111) surface via (a) $-\text{NH}_2$ group (b) $-\text{SH}$ group (c) $-\text{S}$ group, the hydrogen atom in $-\text{SH}$ group is considered to be dissociated via the adsorption.

is about 0.3 eV weaker than the contact bonding in the Au/BDT/Au junction.

We have calculated the bond energies to directly compare with the experimental data[143] using the same total energy method in Section 5.2.1, for the metal-molecule interface of an ABT molecule attaching to the Au(111) surface (with cross-section $c(4\times 3)$) via an Au adatom. As shown in Fig.5.6, ABT attaches to the surface through the $-\text{SH}$ (denote the thiol group side) or $-\text{NH}_2$ (denote the amine group side). Considering rotational symmetry, we have adopted different configurations using a method similar to that of Section 5.2.1. The difference of total-energy E_{total} for these configurations of Au-ABT systems gives the different bond energies of adsorption. The bond energy calculated from the most stable configuration is adopted to compare to the experimental bond energy. The formula of evaluating the bond energy E_B is:

$$E_B = E_{AuSurface} + E_{IsolatedMolecule} - E_{Au-ABT} \quad (5.1)$$

Here, $E_{AuSurface}$ is the total energy of a bare $c(4\times 3)$ Au(111) surface with an adatom on it. $E_{IsolatedMolecule}$ is the total energy of the isolated SH-benzene- NH_2 or S-benzene- NH_2 , and E_{Au-ABT} is the total energy of the $c(4\times 3)$ Au(111) surface with the adsorption of ABT molecule.

The calculated results are listed in the Table 5.5. We highlighted the bond energies calculated from the most stable configurations in Tab. 5.5 as the predicted theoretical value. If the ABT attaches to the Au surface through amine group, the bond energy

System	0^0		60^0	
	E_{total}	E_B	E_{total}	E_B
Au Surface + Au adatom	$E_{total} = -230.20$			
Isolated SH-benzene-NH ₂	$E_{total} = -91.93$			
Isolated S-benzene-NH ₂	$E_{total} = -87.58$			
Au-NH ₂	-322.66	0.53	-322.72	0.59
Au-SH(HND)	-322.85	0.72	-322.98	0.86
Au-S(HD)	-319.39	1.61	-319.49	1.71

Table 5.5: The total energies E_{total} of ABT adsorption and the bond energies E_B . Au-NH₂ is corresponding to the case that ABT attaches to the Au surface via NH₂ group, Au-SH and Au-S are corresponding to the cases of ABT attaches to the Au surface via -SH group but with hydrogen non-dissociated or hydrogen dissociated model. The angles 0^0 and 60^0 are used to cover the configurations in case of rotational symmetry of the system. Energies are in unit of eV.

is found to be 0.59eV which is close to the measured[142] 0.69 eV. If the ABT attaches to the Au surface through a thiol group, we have considered both the HD- and HND-model. For the HD-model, the calculated bond energy of Au-S is as high as 1.71 eV which is consistent with known Au-S bond of 1.60 eV[142]. Importantly, for the HND-model, the calculated bond energy of Au-SH is 0.86 eV, namely 0.27 eV higher than the bond energy 0.59 eV of Au-NH₂, while the experiment measured the difference to be around 0.3 eV[143]. Therefore, the HND-model, once again, shows an amazing agreement with the experimental measurement.

In the old perception of the HD-model, the breakdown of Au-thiol type junctions such as Au/BDT/Au was considered to happen during the rupture of Au-Au bonds. The reason is that the bond energy of Au-S, 1.6eV (or 1.71 eV predicted by our calculation), is much larger than the reported bond energy of 1.0 eV of Au-Au[142]. It was thus hypothesized that a gold chain might be dragged out from the Au surface while stretching the Au/BDT/Au junctions. However, based on our new HND-model, the bond energy of Au-SH is about 0.86 eV which is smaller than but close to the bond energy 1.0 eV of Au-Au bond. This result suggests that the hypothesis of a gold chain in the junction might not be true. The breakdown always happens in

the Au-molecule interface since the Au-SH bond is weaker than the Au-Au bond. This understanding helps us to set up the appropriate atomic model for transport calculations (see Section 5.2.4).

Our first-principles calculation based on the HND-model gives satisfactory bond energies of Au-NH₂ and Au-SH in comparison to measured data for junctions of Au/BDT/Au, Au/ABT/Au and Au/BDA/Au. The HD-model, on the other hand, fails to explain the experiments[122, 123, 124, 125, 134, 135]. This fact, once again, suggests the newly found HND structure is most suitable for modeling the Au/BDT/Au molecular wires.

5.2.4 Conductance

Having presented several consistent checks on the Au/BDT contact structure, we establish that the HND-model is likely to be the most suitable one for describing the Au/BDT/Au device. On the other hand, previous calculations of conductance for this device were almost all based on the HD-model[120, 122, 123, 124, 134, 135, 125, 119]. Here, we shall compare the results between the HND- and HD-models and, importantly, compare them to the experimental data[2, 25, 126].

Our transport analysis is based on the NEGF-DFT formalism introduced in Chapter 3. In the NEGF-DFT self-consistent calculation of the density matrix and Hamiltonian, we use double- ζ plus polarization (DZP) linear combination of atomic orbitals (LCAO) basis sets for all the atoms, GGA-PBE for the exchange-correlation potential[44], and define atomic core potentials using standard norm conserving pseudo-potentials[144]. All the pseudo potential and basis sets are generated following the procedures of Appendix A and B.

Figure 5.8 shows the calculated transmission(T) spectra of Au/BDT/Au device versus energy E , in an energy range of -3.0 eV to 3.5 eV. For the HND-model, the equilibrium conductance (the value of T at Fermi level) was found to be $0.054G_o$ for a junction at its equilibrium junction length ($L = 13.8$ Å). This conductance decreases when stretching the junction, and finally reaches $0.020G_o$ for $L \approx 15.7$ Å, at which the junction starts its mechanical breakdown (see Section 5.2.2). The inset of

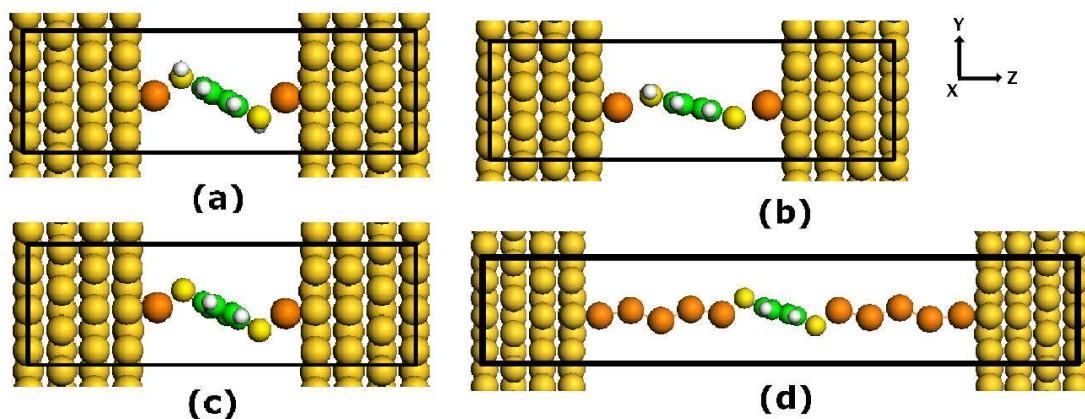


Figure 5.7: Upper panels are for H-dissociative junctions: (a) BDT linked to Au(111) via ad-atoms; (b) BDT linked by Au chains of various lengths. Lower panels are for H-non-dissociative junctions: (c) BDT linked by ad-atoms; (d) as as (c) but with mechanical stretching of the junction.

Fig. 5.8 plots conductance versus L . This range of conductance is within the same order of magnitude as, but roughly a factor 2-5 larger than, the experimental value of $0.011G_o$ [2] to $0.0132G_o$ [25]. On the basis of HND structure, it is also expected that applying post-DFT correction such as quasi-particle or self-interaction correction, can improve the theoretical predictions to be even closer to the experiment values. In comparison, our calculated conductance of all HD-models (Fig. 5.7(c,d)) with or without stretching are much higher, in a range of $0.38 - 0.86G_o$. These high values are consistent with previous *ab initio* calculations [119, 122, 125] which assumed HD-models. Therefore, the HND-model of the Au/BDT/Au junction which is energetically more stable, has conductance values much closer to the experimental data - by at least one order of magnitude, than the HD models.

5.2.5 Scattering states

The transport results clearly suggest that the hybridization of electronic states from Au electrodes and the molecule is significantly different for HND- and HD-models. To understand why, we have analyzed the scattering states near the Fermi level for both models, as shown in Fig. 5.9. When the H is dissociated from a SH group, an electron of the S atom becomes unpaired which has an overwhelming tendency to attract an additional electron to make a pair. This additional electron is most

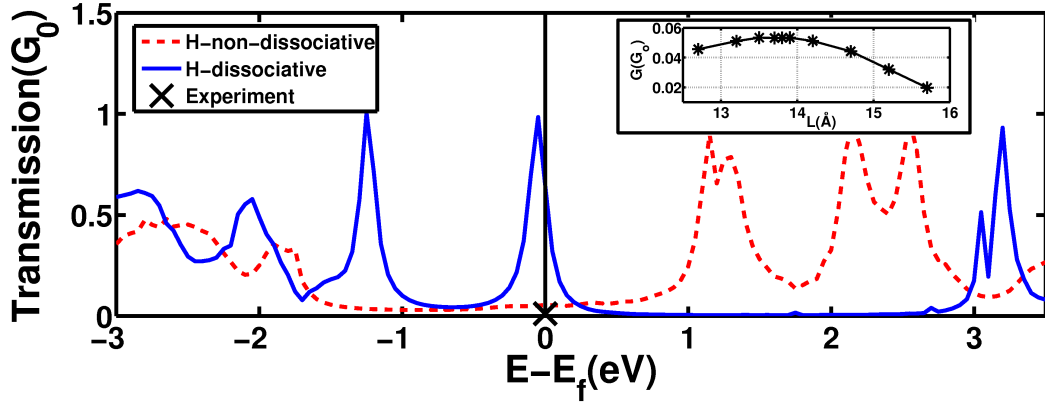


Figure 5.8: Transmission of H-dissociative (solid blue) and H-non-dissociative (dashed red) models versus energy without junction stretching. The cross denotes the experimental value $0.011G_0$ [2]. Inset: conductance (G_0) versus junction length (\AA) under mechanical stretching (Fig. 5.7b) for H-non-dissociative model.

likely contributed by the s -electrons of Au leads, resulting in the charge transfer from leads to the molecule. This transferred electron dopes into the lowest unoccupied molecular orbital (LUMO) of the BDT and pushes down the s -LUMO bonding state to just below the Fermi level, as found in a similar system[145]. The s -LUMO bonding states are expected to be very delocalized, since they were composed of a delocalized LUMO and a delocalized s state. We thus plot the scattering states around the Fermi level, as shown in Fig. 5.9(a). It was found that the conductance around the Fermi level is indeed dominated by a delocalized s -LUMO state as expected. The plot shows the scattering states nicely passing through the junction, giving rise to a high conductance that is at least one order of magnitude larger than the experimental value as discussed above.

On the other hand, for the H-non-dissociative model, the above charge transfer can not happen since all electrons are paired already. Hence the hybridized s -LUMO state around the Fermi level disappears. The bonding picture then switches to that of a lone pair of the S atom donating to the partially unfilled s -band of Au leads. The lone pair is rather localized, like a σ -type orbital. The probable hybridization between the lone-pair and Au leads is therefore somewhat localized, resulting in a tunneling mechanism for electrons going through the junction at low bias: a much

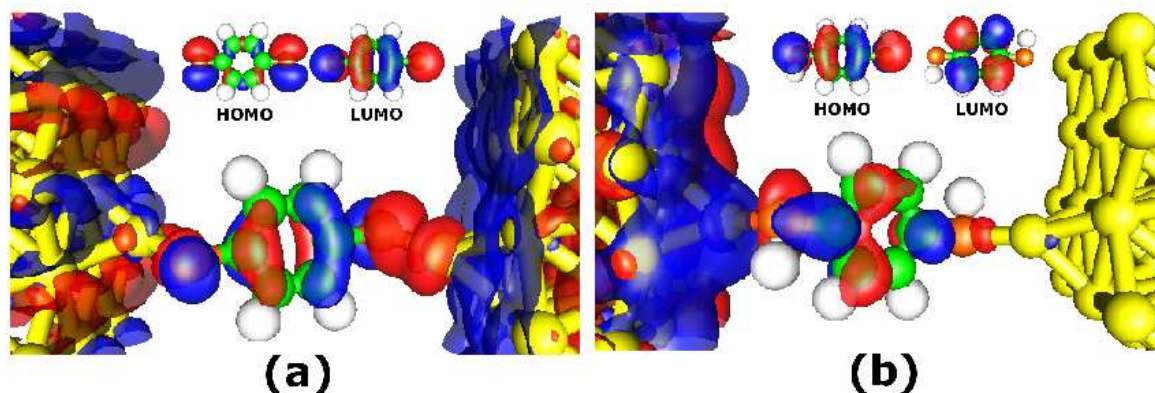


Figure 5.9: Scattering states of: (a) H-dissociative; (b) H-non-dissociative models. Insets are the HOMO and LUMO of the corresponding molecule 1,4-benzenedithiolate and 1,4-benzenedithiol.

smaller conductance is therefore expected. Indeed, as shown in the plot of scattering states in Fig. 5.9(b), very few incoming scattering states can pass through the HND-model junction. In this case, the conductance is mainly contributed by the HOMO of the BDT.

5.3 Charged systems

In previous Sections, we presented a new bonding picture which is the HND-model for the Au/BDT/Au junction. We have confirmed the HND-model using the total energy calculation, direct comparison to experimental measurements of the breakdown force[142] and bond energies[143], and finally direct comparison with the experimental conductance[2, 25, 126]. All these results consistently support the validity of the HND-model. A physical picture of charge transfer discloses the important role of contact structure for electronic transport. In general, our idea should be applicable to Au-thiol type junctions with broad interests.

Considering different experimental environments in the measurement of Au/BDT/Au junctions (vacuum, solution, solid state, etc.), the HND-model still may not cover all the possibilities, and this is especially possible in solutions. Some chemists believe that ionization commonly happens when junctions are put into solution. It means that the proton of the hydrogen atom is possibly dissociated from the -SH bond leav-

ing an electron behind so that the contact becomes Au-S⁻. An interesting question is thus raised: whether or not the proton dissociation will influence conductance of the Au/BDT/Au junction dramatically. More importantly, such a topic might be associated with a more general study of interface charging in molecular junctions. To our knowledge, the relationship of electronic transport and interface charging has never been investigated so far. In the following we carry out a study of interface charging in Au/BDT/Au junctions. By doping external charge at the Au/BDT interface, the charge transfer at the junction interfaces dramatically changes, which in turn significantly influences the conductance in the molecular wires. On the other hand, conductances calculated by HD- and HND-models are nicely bridged to each other by adjusting the interface charging. It provides a higher-level understanding of conductance in the Au/BDT/Au devices from the point of view of charge transfer.

5.3.1 Two charged models

We first define a charged Au/BDT/Au junction. There are two possibilities.

Case-1: H is dissociated as a proton from the -SH bond.

In this case, we adopt the structure of the HD-model as shown in Fig.5.7(a). However, now the S atom acts as an anion such as S⁻. Different from the calculation on the HD-model, here we have to treat the two sulphur atoms in the BDT as ions so that the atomic configuration of the sulphur atoms is no longer neutral. To describe the degree of ionization, let us introduce a definition of effective charge(EC) in the calculation. The EC is defined with the extra charge adopted in the valance electron configuration of the sulphur atom compared to the neutral one. For example, the atomic configuration of ion S⁻ is 3s² 3p⁵ while the neutral one is 3s² 3p⁴. Therefore, the EC for S⁻ is -1.0e. After choosing the atomic configuration, we generate the pseudopotential and double-zeta polarized (DZP) basis using the procedure in Appendix A and B. As a limit, EC=-1.0e corresponds to the proton dissociation.

Furthermore, to study the effect of EC extensively, we adopte a series of ECs (-0.01e , -0.05e , -0.1e, -0.2e, -0.4e, -0.6e, -0.7e -0.75e) for the anion-type S atoms. We do not generate the basis and pseudo potentials when the $|EC|$ is larger than

0.75e. For some numerical deficiency, the scheme of Kleinman-Bylander to reform the pseudopotential[146] does not work properly when the ionic charge is too large in a single S atom. However, our results with EC up to -0.75e are sufficient to uncover the physics of interface charging. With our EC model, we carry out the investigations on the sensitivity of transport with the external charging at the Au/BDT interface, which will be shown in details in the next subsection. Although fractionally ionized cation does not exist in reality, we use it as an efficient way to describe the degree of ionization. As a limit, if the effective charge approaches to zero, the system returns to the HD-model presented in Section 5.2.

Case-2: H is non-dissociative from the -SH bond but acts as a cation H^+ .

In this case, since the H is non-dissociated, we adopt the structure of the HND-model as shown in Fig. 5.7(c). Assuming that a part of the charge will be lost in two H atoms of the two -SH bonds in Au/BDT/Au, these two H atoms are treated as cation-type. Similar to Case-1, in Case-2 we define the effective charge(EC) in these two H atoms with the valance charge. For example, for a configuration $1s^{0.1}$, the EC is 0.1e. Following the definition, we construct a series of cation-type H pseudo potential and DZP basis with a set of ECs (0.01e, 0.05e, 0.1e, 0.2e, 0.4e, 0.6e, 0.8e, 0.9e). As a natural result, if the EC approaches to 1.0e, the system returns to the case of HND-model presented in Section 5.2.

5.3.2 Conductances

We investigated conductance with the EC doped in the Au/BDT/Au junction using the NEGF-DFT formalism. As before, GGA-PBE functional was employed in all the calculations.

Conductance of charged contact: Case-1

In Case-1, as the negative EC is increased in the sulphur atom (from the initial electronic configuration of $S^{0.01-}$ to $S^{0.75-}$), the conductance with the structure of the HD-model significantly drops, as shown in Fig5.10 (black solid line with circles). It is notable that the conductance keeps decreasing with the increase of EC in the

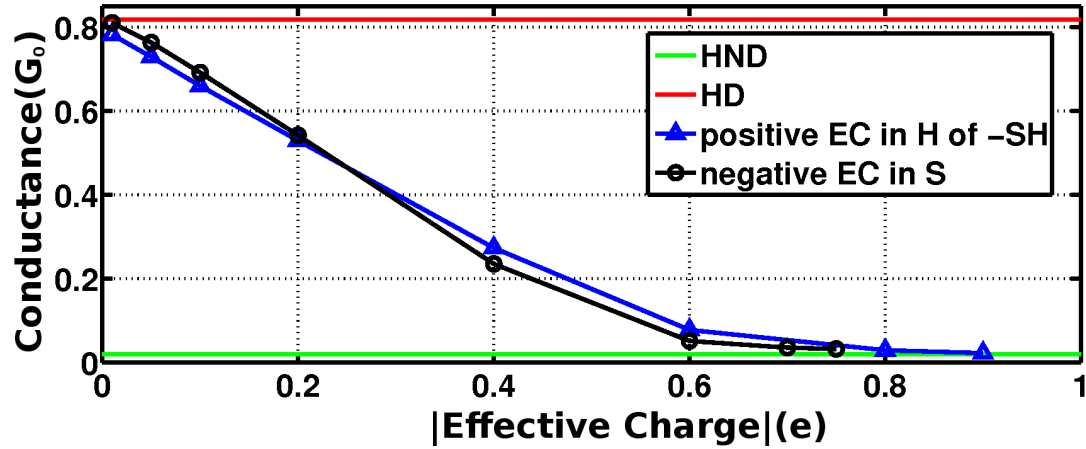


Figure 5.10: The conductance of Au/BDT/Au junction with interface charging. The black-solid line with circles is obtained with negative effective charges applied to the S atom(Case-1). The blue-solid line with triangles is obtained with positive effective charges applied to the hydrogen atom(Case-2). The green-horizontal line corresponds to conductance of the HND-model; the red-horizontal line corresponds to conductance of the HD-model.

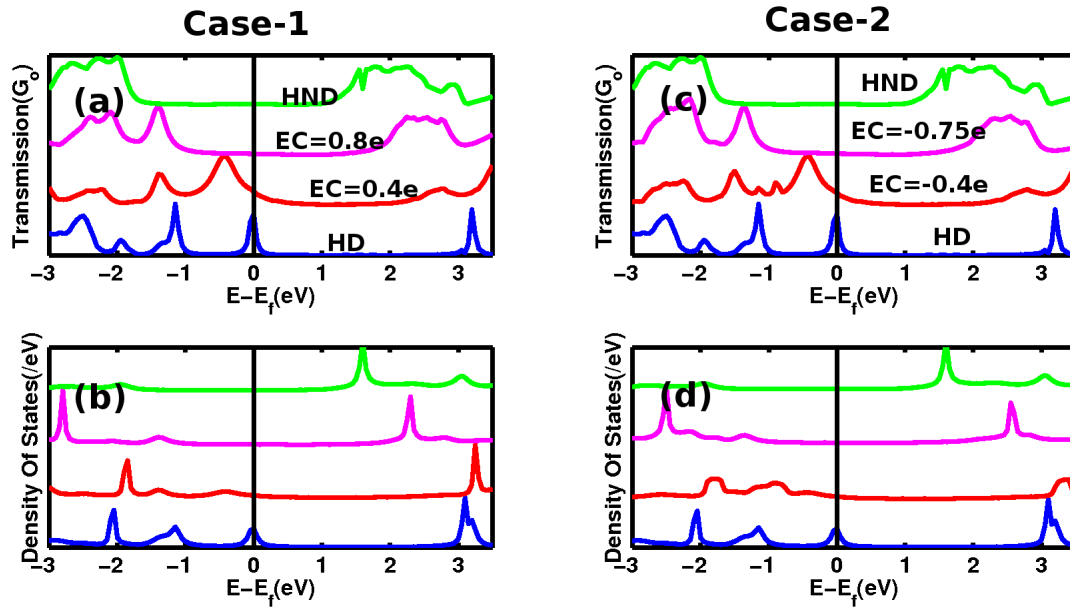


Figure 5.11: The transmission and projected density of states (PDOS) of Au/BDT/Au with the representative effective charge for both Case-1 (HD model with negative effective charge(EC)=-0.4e,-0.75e in S bond) and Case-2(HND model with positive effective charge(EC)=0.4e,0.8e in H atom of -SH bond). (a)Transmission of Case-1; (b) PDOS of Case-1; (c) Transmission of Case-2; (d) PDOS of Case-2.

two sulphur atoms. More importantly, the conductance smoothly approaches to the limit of the conductance calculated by the HND-model when the EC increases. Thus, even if the proton of the hydrogen atom is dissociated away, as long as it leaves the electron behind on the S atom, the conductance of such a junction is essentially the same as that of the HND-model. We emphasize that this is not a simple coincidence. Electronic transport in molecular junction is dominated by electronic structure of the system. Tuning the effective charge on the S atom simulates the physics of charge transfer. As clearly shown in Fig. 5.10, the transmission effectively switches from that of the HD-model to the HND-model.

To further investigate this phenomenon, we also calculated the variations of transmission coefficients and projected density of states (PDOS) by varying the effective charges. Fig. 5.11(a) plots transmission of several representative effective charging situations. In these calculations, we doped both sulphur atoms of the Au/BDT/Au junction having the HD-model structure. Fig. 5.11(b) plots the corresponding PDOS of the BDT molecule. The peaks of PDOS shift from the HD- to the HND-model when the ECs in sulphur atoms are increased.

In the HD-model, the system we studied is neutral thus there is no extra EC in the sulphur atoms. Since the hydrogen atom is dissociated from the SH group, one electron in the sulphur becomes unpaired. Such an unpaired electron is non-local and likely to attract electrons from the Au lead to fill in the LUMO of the benzene-dithiolate. Therefore, in Fig. 5.11(a,b), one can clearly see a peak, which is due to the LUMO of the benzene-dithiolate (which is also the HOMO of benzene-dithiol), pinning the Fermi level E_f . However, with EC on the sulphur atoms, the unpaired electron in the sulphur atom is partially saturated. Therefore, less electron transfer is required from the lead to the molecule. As a result the peak (LUMO of the benzene-dithiolate) shifts away from E_f of the lead and finally reaches a new configuration of the Fermi level alignment. In other words, the less the charge transfer from the lead to the molecule, the weaker the hybridization between the molecule and the lead. Therefore, increasing the extra charge on the S atoms makes scattering states have

more difficulty to traverse through the Au/BDT/Au junction.

Conductance of charged contact: Case-2

In Case-2, if the EC in the H atoms of the -SH bonds are equal to 1.0e, it is just going back to the case of the HND-model as discussed above. However, considering the possibility of losing part of the charge in the H atom of the -SH bond, the EC in H atoms might be less than one. In this case, we found that the conductance increases when the EC decreases, as shown in Fig.5.10 (blue solid line with up-triangles). Once a part of the valence charge is taken away from the H atom of the -SH group, one electron in the sulphur atom who bonds to the H atom, becomes partially unpaired. The unsaturated -SH bond thus prefers to attract some other electrons. Therefore, electrons in the Au lead likely transfer to the molecule in order to saturate the -SH bond. The more the charge taken away from the H in the -SH group, the more electrons from the lead will transfer in. As a result, the HOMO of benzene-dithiol will shift to the E_f for a new alignment due to the charge transfer. Finally, if we take away the entire valence charge from the H atom of the -SH group, the transmission behavior goes back to the HD-model even if the H (proton) is non-dissociative. A proton-type H does not contribute to transport because it only behaves as an empty orbital without a donation of valence charge.

As a summary, the calculated electronic transport behavior of two models with different atomic structures (HND and HD) can be nicely bridged through different ways of interface charging. It is clearly shown in Fig. 5.10 that the conductance of Au/BDT/Au junctions are close to each other for the two contact models if the effective charges in the -SH/-S group are the same. Such a result can be easily understood with the picture of charge transfer in the Au/BDT/Au junction. The effective charge donated by the H atom in the -SH group of HND-model is effectively the same as the extra effective charge in sulphur atom of the HD-model. Both of them will pair with the unpaired electron in the sulphur atom. Therefore, the projected density of states on the molecule are also close to each other with the same effective charge, as shown in Fig. 5.11(b,d). It means that the electronic structures with

the two geometric models (HND and HD) can be effectively the same if the effective charge in the interface is the same. This is the nature of electronic transport in the Au/BDT/Au devices.

Understanding and control of charge transfer in molecular junctions is the key to molecular electronics. Our results suggest that the control of interface charging can be a realistic way to manipulate electron transport in molecular junctions because the interface charging can simply switch the conduction in a molecular junction by orders of magnitude. The conduction in molecular junctions can be flexible if the charge transfer is under control. For example, in chemical engineering, by adjusting the PH value of the solution or functionalizing the interface, the degree of ionization can be easily tuned. It provides a promising way to switch the conductance of the molecular junctions such as Au/BDT/Au from high value (HD-model) to low value (HND-model). Such a feature is potentially useful of realizing single molecule diodes.

5.4 Other molecular junctions

In this Section, we present results of various molecular junctions calculated by the NEGF-DFT method. As we learn from the Au/BDT/Au system, the conduction is very sensitive to atomic configurations in the metal-molecule interface. Therefore, we investigate a series of molecular junctions with different bonding configurations in the interface, namely Au-NH₂, Au-SH and Au-S. As shown in Fig. 5.12, the molecular junctions are constructed as follows: (a) Au/benzene-dithiol (BDT)/Au, (b) Au/1,4-benzene-diamine(BDA)/Au (c) Au/amine-benzene-thiol(ABT)/Au (d) Au/amine-benzene-thiolate/Au (e) Au/thiol-benzene-thiolate/Au (f) Au/1,4-benzene-dithiolate. The structures of all these junctions are similar except the different bonding configurations in the gold-molecule interface. For the junction Au/1,4-benzene-diamine/Au, the contact structure is well controlled since the amine group is so stable that it is extremely difficult to introduce uncertainty in forming the Au-amine contacts.

To keep consistency with our former calculations in this Chapter, we construct all the junctions with the same size of super-cell as that of Au/BDT/Au. Namely, the

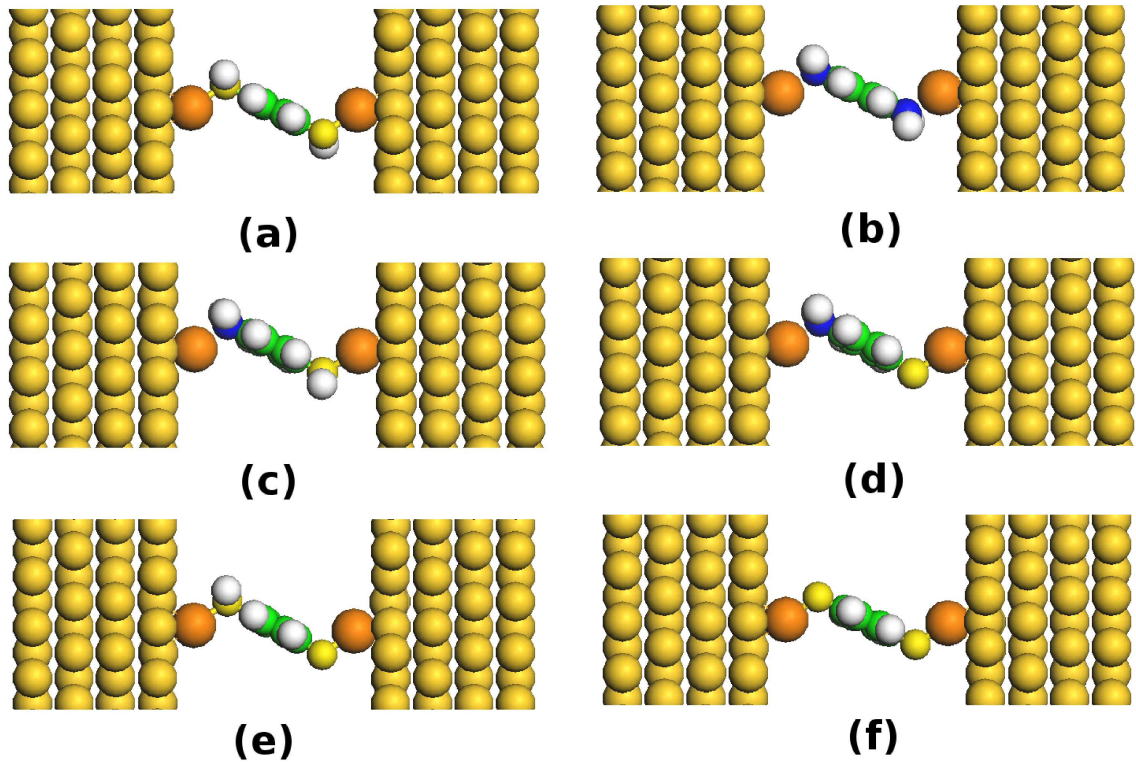


Figure 5.12: The molecular junctions calculated in this Section. (a) Au/benzene-dithiol(BDT)/Au, (b) Au/1,4-benzene-diamine(BDA)/Au (c) Au/amine-benzene-thiol(ABT)/Au (d) Au/amine-benzene-thiolate/Au (e) Au/thiol-benzene-thiolate/Au (f) Au/1,4-benzene-dithiolate.

molecules are sandwiched by two semi-infinite Au(111) slabs. The Au slabs extend to $z = \pm\infty$ along the transport direction z . Periodic boundary condition is applied to the transverse x, y directions with a super-cell cross section of $c(4 \times 3)$. Similar to the modeling of Au/BDT/Au, the atomic structures of the device scattering region for all the junctions are relaxed using the total energy DFT electronic package VASP[58], where the two outermost layers of Au atoms are fixed at their bulk positions (lattice constant 4.1712\AA , which is optimized by GGA-PBE functional in the VASP package). The relaxed scattering region is then connected to the periodic Au leads for two-probe NEGF-DFT analysis. The GGA-PBE functional is adopted throughout.

5.4.1 Total energy and conductance

Summarizing the details in calculating the Au/BDT/Au junction, we shall establish a standard procedure to investigate electronic transport problems in two-probe nano-electronic transport junctions, as follows:

- Setup the atomic two-probe model.

The two-probe model should provide a balance between reality and computational cost. For example, the junction supercell we constructed has a cross-section of $c(3 \times 4)$. Such a cross-section is large enough to avoid any strong interaction between two nearest neighbor images of the molecule. At the same time the calculation cost is acceptable, e.g. there are about 110 atoms in the supercell of the scattering region.

- Optimize the atomic structure in the scattering region.

Since the length of transport junctions in experiments is usually unknown, theoretically we need to calculate junctions having various lengths to cover the possibilities. In other words, one needs to investigate the junction formation process in detail. For example, it is helpful to know the equilibrium and break-down lengths of the junction. It is useful to also calculate the break-down force as described in Section 5.2.2.

- Calculate transport properties.

Having a good understanding of the atomic structure, NEGF-DFT is the standard method in calculating electronic transport properties.

We follow this procedure for our investigations. First, we optimize the junction length, i.e. the distance between the two leads. This is done by moving one lead toward the other lead step by step, with a minimum step of 0.1 \AA . The optimization stops until the net force acting on any atom is less than 0.01 eV/\AA , using the PAW-PBE implemented in the VASP package[58] (see Section 5.2.2).

In typical experimental measurements of junction conductance, the junctions are stretched until mechanical break down[2]. The “quantum” step with a width of 2-3Å in the measured conductance is usually observed. Readers can check with Fig. 2 of Ref.[2] for more information. The mean value of conductance in the step is taken as the conductance of the molecular junction[2]. Theoretically, we can mimic this measuring procedure by varying the length of the junction. In Tab. 5.6 and Tab. 5.7, the calculated equilibrium conductance with various junction lengths is listed. The corresponding total energies of the scattering regions are also given. The equilibrium length of the molecular junctions can be determined from the total energy. For each junction, the conductance around the equilibrium junction length roughly remains a plateau, which forms a conductance step similar to that in the experiments[2]. To view it clearly, we plot the data of all junctions in Fig. 5.13. For the Au/BDT/Au junction, the conductance at equilibrium position ($L = 13.8\text{\AA}$) is $0.054G_o$ with the HND-model (blue-circle line), which is more than an order of magnitude smaller than that of the HD-model ($0.65G_o$, black-up-triangle line). For presentation clarity, the conductance curve of the HD-model has been divided by 10 in Fig. 5.13. For Au/BDA/Au junctions, the conductance step around equilibrium junction length is about $0.028G_o$ while the experimental value is around $0.0066G_o$. For Au/ABT/Au junctions, the conductance step is found to be around $0.0356G_o$ while the experimental value is around $0.0136G_o$. Over all, for the three molecular junctions (BDT, BDA, ABT), our calculated results (NEGF-DFT with GGA-PBE functional) has a systematic difference about a factor of 2-5 larger than the reported experimental values[143]. Again, such a 2-5 factor difference reflects the present reality in theory/experimental comparisons as discussed in Ref.[26]. On the other hand, if we consider the HD-model, the equilibrium conductance found for Au/amine-benzene-thiolate/Au and Au/thiol-benzene-thiolate/Au junctions is about $0.081G_o$ and $0.084G_o$, respectively. These, once again, give much worse comparisons to the measured data.

Going back to the bond energies found in Section 5.2.3, the bond energy 0.59 eV of Au-NH₂ is weaker than the bond Au-SH (0.86eV) and Au-S (1.71eV). A simple picture emerges: the weaker the bond at the interface, the higher the potential barrier for electrons to traverse through. This is easily understandable because the coupling between the molecule and the metallic leads at the interface is mainly determined by the bond strength. Therefore, a stronger metal-molecule bonding means the interface is more transparent for electrons. Indeed, the conductance of Au/BDA/Au is the lowest over all junctions since there are two Au-NH₂ interfaces while Au/benzene-dithiolate/Au junctions have two Au-S interfaces which give the highest conductance.

Another phenomenon is also notable in our calculations. For Au/BDT/Au, the step of conductance is not as clear as the other junctions. As observable from Fig.5.13, the step of conductance in Au/BDA/Au (red-cross line) or Au/ABT/Au (green-plus line) is clearly recognized while Au/BDT/Au junctions (blue-circle line) give a relatively ambiguous step. Such a observation was also reported in experimental measurements[147]. The authors of Ref.[147] measured both Au/BDT/Au and Au/BDA/Au junctions. They stated that “...the variability of the observed conductance for the diamine molecule-Au junctions is much less than the variability for diisonitrile- and dithiol-Au junctions”[147]. Readers can find the results in Fig.2(a) of Ref.[147]. An explicit conductance step is found only for Au/BDA/Au junction but not in Au/BDT/Au, which is consistent with our calculation. Although the Au-NH₂ bond is weaker than the Au-SH bond, the well defined electronic coupling of the N lone pair to Au, makes a good formation of the junction. If we call this phenomenon “electronic stability” of molecular junction, then our calculation and the experiment of Ref.[147] suggest that amine group is a better choice than the thiol group in terms of the electronic stability for forming the transport junctions. Further research, both experimental and theoretical, are needed to test the relationship between electronic stability and interface bonding.

To summarize, a series of molecular junctions with different interface bonding configurations are carefully studied following a well-defined standard procedures.

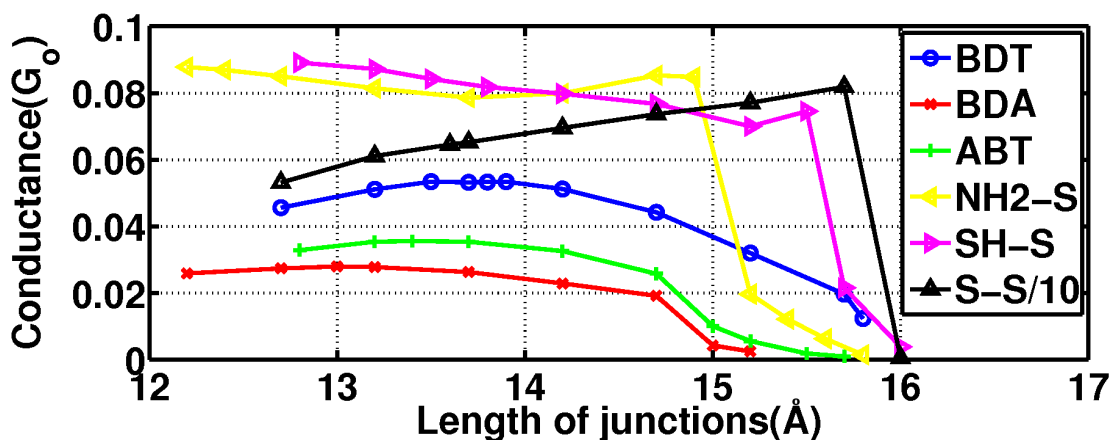


Figure 5.13: The equilibrium conductance of molecular junctions is calculated by varying the length of the junctions. The blue-circle line is for Au/benzene-dithiol/Au junctions, marked as “BDT”; the red-cross line is for Au/benzene-diamine/Au junctions, marked as “BDA”; the green-plus line is for Au/amine-benzene-thiol/Au junctions, marked as “ABT”; the yellow-left-triangle line is for Au/amine-benzene-thiolate/Au junctions, marked as “NH2-S”; the violet-right-triangle line is for Au/thiol-benzene-thiolate/Au junctions, marked as “SH-S”; and the black-up-triangle line is for Au/benzene-dithiolate/Au junctions, marked as “S-S/10” since the value of conductance is divided by a factor of 10 in order to make the data compatible to the others in the same figure.

Compared to all the available experimental data, the calculated conductance within NEGF-DFT method is about a factor of 2-5 to the reported the measured data. The relationship between conductance and the length of junctions are calculated. The conductance steps are found around the equilibrium junction length with a width of 2-3 Å while stretching the junction, which are consistent with the experimental measurements[2, 126, 128].

5.5 Summary

In this Chapter, by total energy calculations we discovered a new contact structure for the Au/BDT/Au molecular wire, the HND-model. This model produced results consistent to measured data regarding the break-down force and bond energies. The equilibrium conductances of the HND-model were found to be $0.054G_0$ at the equilibrium junction length, to $0.020G_0$ at stretched junction just just before breakdown. This range of conductance values is about a factor of 2-5 compared to the measured data. On the other hand, the conductance of any H-dissociated (HD) models is at

(a) Au/BDT/Au junctions						
L (Å)	12.7	13.2	13.5	13.7	13.8*	13.9
Total Energy(eV)	-388.268	-388.380	-388.420	-388.431	-388.434	-388.433
Conductance(G_o)	0.0456	0.0511	0.0534	0.0532	0.0538	0.0534
L (Å)	14.2	14.2	14.7	15.2	15.7**	15.8
Conductance(G_o)	0.0512	0.0442	0.032	0.0197	0.0124	
Total Energy(eV)	-388.411	-388.318	-388.150	-387.927	-387.921	
(b) Au/BDA/Au junctions						
L (Å)	12.2	12.7	13.0*	13.2	13.7	14.2
Total Energy(eV)	-404.857	-404.942	-404.968	-404.960	-404.881	-404.735
Conductance(G_o)	0.0259	0.0274	0.0280	0.0278	0.0263	0.0229
L (Å)	14.7**	15.0	15.2			
Total Energy(eV)	-404.552	-404.545	-404.529			
Conductance(G_o)	0.0192	0.0043	0.0025			
(c) Au/ABT/Au junctions						
L (Å)	12.8	13.2	13.4*	13.7	14.2	14.7
Total Energy(eV)	-396.658	-396.703	-396.710	-396.695	-396.611	-396.466
Conductance(G_o)	0.0329	0.0354	0.0356	0.0354	0.0326	0.0258
L (Å)	15.0**	15.2	15.5	15.7		
Total Energy(eV)	-396.396	-396.373	-396.352	-396.341		
Conductance(G_o)	0.0101	0.0056	0.0019	0.001		

Table 5.6: Total energies of the scattering region and the corresponding conductance are given for various length of the transport junctions. (a) Au/benzene-dithiol(BDT)/Au, (b) Au/benzene-diamine(BDA)/Au and (c) Au/amine-benzene-thiol(ABT)/Au. L is defined as the distance between the two Au lead surfaces in the junction, the same definition as Tab. 5.4 and Fig.5.3 in Section 5.2.2. The conductance is calculated using the standard NEGF-DFT method. *The equilibrium positions are found at (a) $L = 13.8\text{Å}$ (b) $L = 13.0\text{Å}$ and (c) $L = 13.4\text{Å}$. **The break-down positions are found at (a) $L = 15.7\text{Å}$ (b) $L = 14.7\text{Å}$ and (c) $L = 15.0\text{Å}$

(d)Au/amine-benzene-thiolate/Au junctions						
L (Å)	12.2	12.4	12.7	13.2*	13.7	14.2
Total Energy(eV)	-392.992	-393.049	-393.105	-393.157	-393.107	-392.969
Conductance(G_o)	0.0878	0.0869	0.0850	0.0814	0.0786	0.0799
L (Å)	14.7	14.9**	15.2	15.4	15.6	
Total Energy(eV)	-392.741	-392.675	-392.647	-392.633	-392.624	
Conductance(G_o)	0.0853	0.0848	0.0197	0.0122	0.0063	

(e)Au/thiol-benzene-thiolate/Au junctions						
L (Å)	12.8	13.2	13.5*	13.8	14.2	14.7
Total Energy(eV)	-384.821	-384.894	-384.920	-384.916	-384.859	-384.706
Conductance(G_o)	0.0891	0.0872	0.0842	0.0818	0.0798	0.0767
L (Å)	15.2	15.5**	15.7	16.0		
Total Energy(eV)	-384.733	-384.290	-384.258	-384.255		
Conductance(G_o)	0.0700	0.0745	0.0216	0.0039		

(f)Au/benzene-dithiolate/Au junctions						
L (Å)	12.7	13.2	13.6*	13.7	14.2	14.7
Total Energy(eV)	-381.195	-381.340	-381.377	-381.368	-381.282	-381.055
Conductance(G_o)	0.5314	0.6109	0.6453	0.6524	0.6953	0.7366
L (Å)	15.2	15.7	16.0**			
Total Energy(eV)	-380.682	-380.213	-379.869			
Conductance(G_o)	0.7705	0.8182	0.0058			

Table 5.7: This table is the continuation of Tab.5.6. The total energies of the scattering region and the corresponding conductance are given for various length of the (d)Au/amine-benzene-thiolate/Au, (e)Au/thiol-benzene-thiolate/Au and (f) Au/benzene-dithiolate/Au junctions. L is defined as the distance between the two Au slabs in the junctions, the same definition as Tab. 5.4 and Fig.5.3 in Section 5.2.2. For different L , the conductance of these molecular junctions is calculated using standard NEGF-DFT method. *The equilibrium positions are found at (d) $L = 13.2\text{Å}$ (e) $L = 13.5\text{Å}$ and (f) $L = 13.6\text{Å}$. **The break-down positions are found at(d) $L = 14.9\text{Å}$ (e) $L = 15.5\text{Å}$ and (f) $L = 16.0\text{Å}$

least one order of magnitude larger than the experimental value. In other words, the HND-model significantly narrowed the gap between NEGF-DFT theory and the experimental results. Our investigation clearly reveals how contact formation could drastically influence transport properties. We believe our results made a substantial step towards resolving a long standing problem of theory-experimental discrepancy concerning the Au/BDT/Au molecular wires. The discrepancy was, most likely, due to the use of incorrect contact models for the Au/BDT interface. Although standard NEGF-DFT methods have achieved a wide range of successes in quantitative predictions for many molecular and solid state devices, the junctions of Au/BDT/Au were an exception. In this work, we provided strong evidence that the discrepancy was actually not due to the NEGF-DFT formalism. Considering the complexities in experimental measurements, our results are rather satisfactory.

6

Summary

In this work, we carried out quantitative investigations on electronic transport properties of several molecular devices. The calculations are based on carrying out density function theory within the framework of Keldysh non-equilibrium Green's function formalism. The NEGF-DFT formalism allows us to make not only **qualitative** but also **quantitative** predictions that can be directly compared to the experimental measurements. Based on our calculations, a procedure emerges for systematically investigating electronic transport problems from atomic first principle. This procedure includes careful pseudopotential and basis generation, structural analysis - especially on the device contacts, and finally systematic electronic transport calculations.

In Chapter 4, we investigated the molecular spintronic junction Ni/octanethiolate/Ni. To our knowledge, this was the first time that direct and quantitative comparison was made between first principles modeling and experiments on spin injection from ferromagnetic metal to molecular layers at nonequilibrium. In our results, the maximum TMR is found to 33% at $V_b = -20mV$. This is to be compared to the measured data which is 12% to 16% at -15mV to -5mV. Our work revealed the microscopic physics of spin polarized transmission and coupling between the states in Ni and atomic orbitals in the molecule. Interface bonding shows strong influence on TMR value of the junctions. It suggests a high sensitivity on chemical details of spin polarized transport in molecular spintronics. On the technical side, for spin injection our work demonstrates that in order to obtain accurate results, enormous k-sampling is necessary. In this sense, the results provide a benchmark for further theoretical calculations of molecular spintronics. At the present stage of molecular spintronics

research, given the many uncertainties in the experimental measurements and the approximations in the NEGF-DFT formalism, we believe our quantitative consistency with the measured data is rather satisfactory in many aspects, and provides a starting point to resolve the remaining differences. While we focused on discussing Ni/octanethiolate/Ni which were measured experimentally, we have also performed similar calculations for Fe/octanethiolate (octane-dithiolate)/Fe junctions and obtained qualitatively comparable results.

In Chapter 5, we carefully investigated the Au/BDT/Au junctions in several aspects: the contact structure, break-down force, bonding energy, conductance and interface charging. On the structural side, our investigations reveal that the H atoms in the thiol groups of the BDT energetically prefer to be non-dissociative after the transport junctions are formed. This finding is supported by the force calculation that the junction break-down force of the HND structure is consistent with the measured data[142], while the HD structure gives a break-down force that is too large compared with the experimental results. The calculated bonding energy of Au-thiol within the HND-model agrees with the experimental measurement[143] much better than that is given by the HD-model. On the functional side, the introduction of non-dissociative H atoms at the Au-BDT contacts blocks charge transfer doping to BDT from Au electrodes, effectively induces an extra potential barrier that considerably reduces the electron transparency of the Au/BDT interface. The study of interface charging based on these two models (HD and HND) further confirms this physical picture. Since thiol molecules provide perhaps the most popular binding linkers in experiments, these results shed considerable light on charge conduction properties at the single-molecule level.

Based on the HND structures, we predicted a range of conductance, from $0.054G_0$ at equilibrium junction length, to $0.020 G_0$ at the junction length just before junction breakdown, which is in much better consistency with the measured values[2, 25, 126, 128] than the HD structures. Indeed, all HD junctions we have examined produced conductance values more than at least one order of magnitude larger than

the experimental value. Our investigation clearly reveals how structure formation could drastically influence transport properties. We believe that our finding is a substantial step towards resolving the long-standing theory-experiment discrepancy on the conductance of Au/BDT/Au, which is a most widely studied molecular transport junction. Finally, we also investigated a series of other molecular junctions with different interface bonding configurations following our calculation procedure. Compared to the available experimental conductance data, the predicted values are also within a factor 2-5, which is similar to the theory-experiment difference found in Au/BDT/Au and Ni/octanethiolate/Ni junctions.

Our results presented here, in published papers and manuscripts[28, 30, 31, 32], as well as reports of other researchers[26, 137, 27, 138], all indicate that the state-of-the-art NEGF-DFT formalism can achieve quantitative consistency with the measured data to within a factor of 2-5 and, in many situations, much better agreement can be obtained. The final difference between quantitative theory and measurement is likely to be resolved in the future by improvements of experimental accuracy and improvements of theoretical issues. In this work, we focused on solving issues associated with the device contact structure, k-sampling, pseudo potential and LCAO basis functions. In the future, several other issues shall be resolved. These include using or constructing better exchange-correlation functionals, removing self-interactions from the mean fields, and adding interaction effects between electrons and molecular vibrational modes. With these and perhaps other improvements, we believe excellent quantitative predictions - as excellent as those in spectroscopy, can be achieved for quantum transport modeling of molecular electronics.

Appendices

A

PSEUDOPOTENTIAL GENERATION

In this Appendix, we summarize the generation of pseudopotentials used in this thesis.

A.1 General procedure

There are several ways for constructing a pseudopotential. We follow the original work of Trouiller and Martin[144] in our implementation. The procedure are summarized in the following four steps.

- **Step 1:** We solved the all-electron Kohn-Sham equation for a single atom after choosing an appropriate exchange-correlation functional and consider the wave function in the spherical form: $R_l(r)Y_{ml}(\theta, \phi)$ where $Y_{ml}(\theta, \phi)$ is the spherical harmonics at polar and azimuthal angles θ, ϕ . A spherical screening approximation is applied as an additional constraint to produce a spherically symmetric charge density $\rho(\vec{r})$. The radial Kohn-Sham equation is[144]:

$$\left[\frac{-1}{2} \frac{d^2}{dr^2} + \frac{l(l+1)}{2r^2} + V[\rho; r] \right] r R_{nl}(r) = \epsilon_{nl} r R_{nl}(r) , \quad (\text{A.1})$$

and the all-electron (AE) single atom potential is:

$$V_{AE} = -Z/r + V_H[\rho(r)] + V_{xc}[\rho(r)] . \quad (\text{A.2})$$

- **Step 2:** In the second step, the pseudo valence orbitals are constructed from the all-electron valence orbitals. The norm-conserving pseudopotential are constructed with the following four criteria[144]:

- The pseudopotential wave function should be nodeless because a smooth pseudo-wave function is desirable.
- Beyond a chosen radial cutoff r_c , the radial part of the pseudo-wave function should be equal to the all-electron wave function, namely $R_l^{PP}(r) = R_l^{AE}(r)$ for $r > r_c$.
- Conservation of charge within r_c should be guaranteed:

$$\int_0^{r_c} |R_l^{PP}(r)|^2 r^2 dr = \int_0^{r_c} |R_l^{AE}(r)|^2 r^2 dr . \quad (\text{A.3})$$

- The valence all-electron and pseudo-potential eigenvalues should equal to each other.
- **Step 3:** Given the pseudo-wave function, the screened pseudo potential is obtained by:

$$V_{scr,l}^{PP}(r) = \epsilon_l - \frac{l(l+1)}{2r^2} + \frac{1}{2rR_l^{PP}(r)} \frac{d^2}{dr^2} [rR_l^{PP}(r)] . \quad (\text{A.4})$$

From this equation, two important details are introduced. The only singularity for pseudopotential is at the origin; the continuity of pseudo potential depends on the continuity of pseudo-wave function up to second order derivative.

- **Step 4:** The final pseudopotential is obtained by subtracting off the contribution from the Hartree and exchange-correlation terms from the pseudo orbital valence charge:

$$V_l^{PP} = V_{scr,l}^{PP} - V_H[\rho^{PP}] - V_{xc}[\rho^{PP}] . \quad (\text{A.5})$$

Using our implementation, we generated pseudopotentials and pseudo atomic orbitals for most elements of the periodic table.

A.2 Non-linear Core corrections

For transition metals whose typical outer electronic configuration is $nd^i(n+1)s^j(n+1)p^k$, the valence nd -electrons are localized in the same spatial region as ns and np which

should be taken as the semi-core electron. The overlap of core and valence electrons makes it necessary to evaluate the potential using the total charge density $\rho^{val} + \rho^{core}$. In this case the contribution to the exchange-correlation potential from the core density is also subtracted from the screened pseudopotential, it becomes:

$$V_l^{PP} = V_{scr,l}^{PP} - V_H[\rho^{PP}] - V_{xc}[\rho_0^{core} + \rho^{PP}] \quad (\text{A.6})$$

The core density may oscillate rapidly near the atomic nucleus making it difficult to represent on a real space grid. However, since the only relevant portion of the core charge is that overlapping with the valence charge, the inner core electron density is replaced by a smooth function which is called ‘‘core correction’’ of the pseudo potential:

$$\rho_c(r) = \begin{cases} Ar^l e^{-\alpha r} & \text{if } r < r_c \\ \rho_{core}(r) & \text{if } r > r_c \end{cases} . \quad (\text{A.7})$$

A typical radius for core correction is around 0.6 – 1 au. Usually, for semi-core cases the core correction approach is helpful. However, limited by the hybridization of core-valence electrons, the transferability of these core corrected pseudo potential is generally poor. Therefore, very careful checks are necessary before using these pseudo potentials to a specific physical system.

A.3 Non-local pseudo potential

The norm-conserving pseudopotential is angular-momentum l -dependent which is attributed to the non-local part for each l based pseudo potential. To treat this part independently, a local potential V_{local} is introduced and subtracted for each angular momentum channel l :

$$V_{non-local}(r) = V_{ion,l}^{PP} - V_{ion,local}^{PP}(r) . \quad (\text{A.8})$$

The exact form of V_{local} is in principle arbitrary. Following Ref.[53], the form we use is given by the potential generated by a positive charge distribution of the following form:

$$\rho^{local}(r) \propto \exp[-(\sinh(a \cdot b \cdot r)/\sinh(b))^2] , \quad (\text{A.9})$$

where the total charge of ρ_{local} is equal to the valence of the atom. The procedure outlined above is performed with the atomic software package ATOM[63] and Nanobase[62], respectively.

A.4 Kleinman-Bylander non-local pseudo-potential

To speed up pseudopotentials calculation in plane wave basis methods, one introduces the fully separable form of the pseudopotential. The pseudopotentials we generated above is in semi-local form which can be costly for numerical integrals over the orbital. To bypass such a difficulty, Kleinman and Bylander proposed a fully separable form of the pseudopotential[146]:

$$\hat{V}_{KB} = \hat{V}_{local} + \sum_{lm} \frac{|\delta V_l^{PP} \phi_{lm}\rangle \langle \delta V_l^{PP} \phi_{lm}|}{\langle \phi_{lm} | \delta_l^{PP} | \phi_{lm} \rangle}. \quad (\text{A.10})$$

The Kleinman-Bylander scheme is usually good. Nevertheless, for some cases an inappropriate cutoff might lead to un-physical ghost states, namely it can make the lowest p state is lower than the lowest s state. Therefore, checking of ghost states is a standard procedure for Kleinman-Bylander pseudo potential generation.

A.5 Tips for pseudo potential generation

Typically there are two criteria to judge the quality of a pseudo potential: softness and transferability. A pseudo potential is said to be “soft” if the cutoff radius r_c is large. A soft pseudo potential always gives faster computation but loses transferability. Therefore it is usually a good idea to reduce r_c , i.e. making the pseudopotential harder, to improve transferability. Practically, we should keep r_c larger than the outmost node of all-electron wave function. The art in creating a good pseudopotential requires a balance between the softness and transferability. For more details about pseudo potential, a useful note is recommended: <http://www.fisica.uniud.it/gian-nozz/Atom/doc.pdf>.

B

LCAO BASIS SET

In this Appendix, we introduce the generation of LCAO (linear combination atomic orbital) basis sets. In DFT, apart from numerical errors, there are three main systematic errors. They are due to the use of approximate exchange-correlation potential, the use of pseudopotential, and the use of finite basis sets for expanding physical quantities. This Appendix discusses the issues of basis sets. We have generated a comprehensive database for pseudopotential and atomic orbital basis set for most elements of the periodic table that has been carefully calibrated and can be used by the DFT community at large.

In Appendix A, we have discussed the generation of pseudo potential. A well tested pseudo potential has good transferability. This is important for basis generation because the LCAO type basis sets are constructed from the pseudopotential. In plane wave basis set, the accuracy can be controlled by simply increasing the number of plane waves. It is however difficult to arbitrarily increase the number of LCAO basis functions. Basis optimization provides an option to achieve high accuracy with finite number of atomic orbital basis functions.

B.1 Data of benchmark calculation

All the optimized basis sets in our database are compared with benchmark calculations. The benchmark results in this work are obtained by the VASP and Gaussian98 electronic package[58]. The lattice constant of all the elements with the structure of FCC (face centered cubic), BCC (body centered cubic) , HCP (hexagonal close-

packed), and other compounds (mainly (0,1/4) and (0,1/2) FCC structures) are optimized with LDA/PBE functional by the VASP package. The aim of this work is to provide the benchmark data for users with broad interests. All the benchmark results (band structures, density of states, .etc.) are calculated based on the optimized lattice constants instead of the experimental values. Such a way is usually recommended because the experimental values deviate from the energetic minimum predicted by the DFT functionals. These optimized lattice constants are shown in Tab. B.1, B.2 and B.3.

B.2 Basis optimization with constructed cost function

The idea of basis optimization is to find a cost function to be minimized. Usually, a basis set is constructed with several parameters, i.e. the atomic orbital is defined as a multi-dimensional function. The change of any parameter will influence the shape of the orbital. The best way to evaluate a set of optimal parameters is the minimization with the chosen cost function. Downhill simplex algorithm is taken as one of the best schemes to find minimum in multi-dimensional space, which has been implemented in NanoDCAL package[52]. A cost function is usually adopted from real physical quantities such as total energy or band structure. We make the choice carefully regarding our specific systems. For metallic systems, the total energy is a good cost function. For semiconductors, the band structure/band gap can be a better choice.

In Fig.B.1, we give an example of the basis optimization with different cost functions. The system is Si FCC structure with lattice constant 5.4080\AA and single-zeta polarized basis sets (SZP). SZP includes one s-orbital, three p-orbital and five d-orbital. In Fig.B.1(b), the basis is optimized with total energy as the cost function. Compared to the pre-optimization result, the valence bands have a better match with the benchmark provided by VASP. However, the conduction bands are still wrong although some improvements were obtained compared to the pre-optimization one. With the basis optimized by the cost function of band gap (0.4522eV), it captures

Element	lattice constant(Å)				Element	lattice constant(Å)			
	Str	Exp	LDA	PBE		Str	Exp	LDA	PBE
Au	FCC	4.0782	4.0655	4.1712	Li	BCC	3.5100	3.3639	3.4412
Ag	FCC	4.0853	4.0189	4.1705	Na*	BCC	4.2906	4.0498	4.1956
Cu	FCC	3.6149	3.5241	3.6385	K*	BCC	5.3280	5.0434	5.2888
Ni	FCC	3.5240	3.4218	3.5224	Rb*	BCC	5.5850	5.3750	5.6725
Al	FCC	4.0495	3.9917	4.0450	Cs*	BCC	6.1410	5.7613	6.1606
Pt	FCC	3.9242	3.9075	3.9779	Ba*	BCC	5.0280	4.7692	5.0284
Pd	FCC	3.8907	3.8570	3.9573	Fe	BCC	2.8665	2.7418	2.8360
Pb*	FCC	4.9508	4.8860	5.0449	W	BCC	3.1652	3.1308	3.1747
Co	FCC	—	3.4135	3.5207	V	BCC	3.0300	2.9064	2.9761
Si	FCC	5.4309	5.4080	5.4739	V*	BCC	3.0300	2.9258	2.9999
Ge	FCC	5.6575	5.6503	5.7878	Cr	BCC	2.9100	2.7859	2.8678
Ca*	FCC	5.5884	5.3299	5.5269	Cr*	BCC	2.9100	2.7913	2.8877
Sr*	FCC	6.0849	5.7875	6.0203	Mn	BCC	—	2.7146	2.7769
Rh	FCC	3.8034	3.7675	3.8418	Nb*	BCC	3.3004	3.2635	3.3204
Ir	FCC	3.8390	3.8201	3.8772	Mo*	BCC	3.1470	3.1251	3.1680
Hg	FCC	—	4.4684	4.4780	Ta*	BCC	3.3013	3.2594	3.3222

* **semicore is considered**

Table B.1: Lattice constants for elements with FCC, BCC structures are optimized by LDA/PBE functional using the VASP package. The results are compared with the available experimental data in www.webelements.com.

Element	lattice constant(\AA)			
	Str	Exp	LDA	PBE
Co	HCP	2.5071/4.0695	2.4252/3.9271	2.5032/4.0342
Be	HCP	2.2858/3.5843	2.2279/3.5173	2.2645/3.5679
Mg	HCP	3.2094/5.2108	3.1290/5.0962	3.1909/5.1948
Zn	HCP	2.6649/4.9468	2.5826/4.7264	2.6850/4.9093
Cd	HCP	2.9794/5.6186	2.9269/5.4575	3.0479/5.6923
Sc*	HCP	3.3090/5.2733	3.2163/5.0416	3.3208/5.1764
Ti*	HCP	2.9508/4.6855	2.8622/4.5420	2.9402/4.6546
Y *	HCP	3.6474/5.7306	3.5345/5.5361	3.6556/5.6969
Zr*	HCP	3.2320/5.1470	3.1699/5.0703	3.2418/5.1872
Tc*	HCP	2.7350/4.3880	2.7141/4.3588	2.7506/4.4287
Ru*	HCP	2.7059/4.2815	2.6905/4.2424	2.7379/4.3116
Hf*	HCP	3.1964/5.0511	3.1223/4.9386	3.2044/5.0678
Re*	HCP	2.7610/4.4560	2.7455/4.4235	2.7754/4.4906
Os*	HCP	2.7344/4.3173	2.7186/4.2840	2.7518/4.3572
Tl*	HCP	3.4566/5.5248	3.4140/5.4242	3.5873/5.6611
ZnO	HCP	3.2500/5.2000	3.2050/5.1357	3.2976/5.2913

* **semicore is considered**

Table B.2: Lattice constants(a/c) for elements and compounds with HCP structure are optimized by LDA/PBE functionals using the VASP package. The results are compared with the available experimental data in www.webelements.com.

Element	lattice constant(\AA)			
	Str	Exp	LDA	PBE
ZnS	FCC(0,1/4)	5.4093	5.3037	5.4518
ZnSe	FCC(0,1/4)	5.6710	5.5759	5.7436
BN	FCC(0,1/4)	3.6150	3.5857	3.6254
GaN	FCC(0,1/4)	4.5000	4.5039	4.5894
GaP	FCC(0,1/4)	5.4500	5.4271	5.5355
GaAs	FCC(0,1/4)	5.6532	5.6284	5.7669
AlN	FCC(0,1/4)	4.3700	4.3480	4.4005
AlP	FCC(0,1/4)	5.4500	5.4366	5.5065
AlAs	FCC(0,1/4)	5.6600	5.6394	5.7355
InSb	FCC(0,1/4)	6.4790	6.4715	6.6498
MgO	FCC(0,1/2)	4.2112	4.1542	4.2403
MnO	FCC(0,1/2)	4.4480	4.0110	4.1054
KCl*	FCC(0,1/2)	6.2900	6.1299	6.4220
AgBr	FCC(0,1/2)	5.7745	5.5973	5.8557
KBr*	FCC(0,1/2)	6.5966	6.4189	6.7415
NaCl*	FCC(0,1/2)	5.6200	5.4676	5.6985
SnTe*	FCC(0,1/2)	6.3268	6.2385	6.4116

* **semicore is considered**

Table B.3: Lattice constants of various compounds are optimized by LDA/PBE functionals using the VASP package. The results are compared with the available experimental data in www.webelements.com.

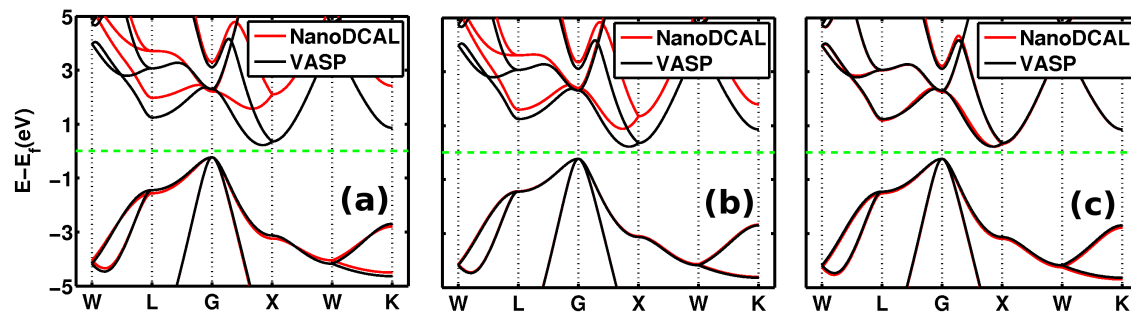


Figure B.1: The calculated band structures of Silicon FCC crystal with different sets of SZP basis obtained in the example of the present appendix. (a) Basis parameters generated by a reasonable initial guess. (b) Starting from the initial guess in (a), optimized against total energy. (c) Starting from the initial guess in (a), optimized against band gap.

the Si FCC bands extremely well, as shown in Fig.B.1(c).

There are two pieces of important information suggested by this example. (i) A proper choice of cost function is crucial for basis optimization. It should not be just an arbitrary combination of physical quantities, and too many freedoms in the cost function will reduce the effectiveness of the optimization process. According to our experience, a good optimization should capture the most important properties one is interested in. For example, the bands near the Fermi level sensitively influence quantum transport. The cost function should therefore be defined to optimize these bands. (ii) In general, our scheme of basis optimization does effectively improve the accuracy of calculation with a limited-size basis sets. In Fig.B.1(c), substantial improvement is evident with the small 9-orbital SZP basis sets.

We end this appendix by several suggestions:

- If the calculation cost allows, always use fairly large basis sets. Double-Zeta polarized basis sets are recommended in general.
- Always check the validity of basis before use. There are no “all-purpose” basis sets.
- Basis optimization is sensitive to initial values. Checking with different initial values will be helpful to find a “best” one.

- Email me(zyning@hotmail.com) for help.

BIBLIOGRAPHY

- [1] Mads Brandbyge, José-Luis Mozos, Pablo Ordejón, Jeremy Taylor, and Kurt Stokbro. Density-functional method for nonequilibrium electron transport. *Phys. Rev. B*, 65(16):165401, Mar 2002.
- [2] Xiaoyin Xiao, Bingqian Xu, and Nongjian J. Tao. Measurement of single molecule conductance: Benzenedithiol and benzenedimethanethiol. *Nano Lett.*, 4:267, 2003.
- [3] Richard Feynman. There's plenty of room at the bottom. <http://www.zyvex.com/nanotech/feynman.html>, Dec 1959.
- [4] Arieh Aviram and Mark A. Ratner. Molecular rectifiers. *Chemical Physics Letters*, 29(2):277, 1974.
- [5] Frank Fan, Brock F. Binkowski, Braeden L. Butler, Peter F. Stecha, Martin K. Lewis, and Keith V. Wood. Novel genetically encoded biosensors using firefly luciferase. *ACS Chem. Biol.*, 3:346, 2008.
- [6] A. M. Hermann and L. Fabick. Research on polycrystalline thin-film photovoltaic devices. *J. Crystal Growth*, 61:658, 2002.
- [7] Victor Giurgiutiu. Review of smart-materials actuation solutions for aeroelastic and vibration control. *J. Intel. Mat. Sys. Str.*, 11:525, 2000.
- [8] V. Dediu, L. E. Hueso, I. Bergenti, A. Riminucci, F. Borgatti, P. Graziosi, C. Newby, F. Casoli, M. P. De Jong, C. Taliani, and Y. Zhan. Room-temperature spintronic effects in alq_3 -based hybrid devices. *Phys. Rev. B*, 78(11):115203, Sep 2008.

- [9] Nongjian Tao. Electron transport in molecular junctions. *Nature nanotechnology*, 1:173, Dec 2006.
- [10] Wei Tang, Huazhong Shi, Gu Xu, Beng S. Ong, Zoran D. Popovic, Jiachun Deng, Jie Zhao, and Guanghui Rao. Memory effect and negative differential resistance by electrode-induced 2-dimensional single-electron tunneling in molecular and organic electronic devices. *Adv. Mater.*, 17:2307, 2005.
- [11] Jeremy Lawrence and Gu Xu. High pressure saturation of hydrogen stored by single-wall carbon nanotubes. *Appl. Phys. Lett.*, 84:918, 2004.
- [12] X. H Qiu, G. V. Nazin, and W. Ho. Vibrationally resolved fluorescence excited with submolecular precision. *Science*, 299:542, 2003.
- [13] T. H. Lee, J. I. Gonzalez, J. Zheng, and R. M. Dickson. Single-molecule optoelectronics. *Acc. Chem. Res.*, 38:534, 2005.
- [14] Z. H. Xiong, D. Wu, Z. V. Vardeny, and J. Shi. Giant magnetoresistance in organic spin-valves. *Nature*, 427:821, 2004.
- [15] Derek Waldron, Paul Haney, Brian Larade, Allan MacDonald, and Hong Guo. Nonlinear spin current and magnetoresistance of molecular tunnel junctions. *Phys. Rev. Lett.*, 96(16):166804, Apr 2006.
- [16] J. R. Petta, S. K. Slater, and D. C. Ralph. Spin-dependent transport in molecular tunnel junctions. *Phys. Rev. Lett.*, 93(13):136601, Sep 2004.
- [17] Y.-C. Chen, M. Zwolak, and M. Di Ventra. Local heating in nanoscale conductors. *Nano Lett.*, 3:1691, 2003.
- [18] T. Seideman and H. Guo. Quantum transport and current-triggered dynamics in molecular tunnel junctions. *J. Theor. Comp. Chem.*, 2:439, 2003.
- [19] Pramod Reddy, Sung-Yeon Jang, Rachel A. Segalman, and Arun Majumdar. Thermoelectricity in molecular junctions. *Science*, 315:1568, 2007.

- [20] Niall J. English, John S. Tse, and Declan J. Carey. Mechanisms for thermal conduction in various polymorphs of methane hydrate. *Phys. Rev. B*, 80(13):134306, Oct 2009.
- [21] A. Rochefort, E. Bayard, and S. Hadj-Messaoud. Competitive hydrogen bonding in p-stacked oligomers. *Adv. Mater.*, 19:1992, 2007.
- [22] Stéphane Bedwani, Daniel Wegner, Michael F. Crommie, and Alain Rochefort. Strongly reshaped organic-metal interfaces: Tetracyanoethylene on cu(100). *Phys. Rev. Lett.*, 101(21):216105, Nov 2008.
- [23] M. A. Reed, C. Zhou, C. J. Muller, T. P. Burgin, and J. M. Tour. Conductance of a molecular junction. *Science*, 278:252, 1997.
- [24] Wenyong Wang, Takhee Lee, and M. A. Reed. Mechanism of electron conduction in self-assembled alkanethiol monolayer devices. *Phys. Rev. B*, 68(3):035416, Jul 2003.
- [25] Hyunwook Song, Youngsang Kim, Yun Hee Jang, Heejun Jeong, Mark A. Reed, and Takhee Lee. Observation of molecular orbital gating. *Nature*, 462:1039, 2009.
- [26] Stuart M. Lindsay and Mark A. Ratner. Molecular transport junctions:clearing mists. *Advanced Materials*, 19:23, 2007.
- [27] Chao-Cheng Kaun and Hong Guo. Resistance of alkanethiol molecular wires. *Nano Lett.*, 3:1521, 2003.
- [28] Zhanyu Ning, Yu Zhu, Jian Wang, and Hong Guo. Quantitative analysis of nonequilibrium spin injection into molecular tunnel junctions. *Phys. Rev. Lett.*, 100(5):056803, Feb 2008.
- [29] Zahid Ferdows, Zhanyu Ning, and Hong Guo. Tuning tunneling magnetoresistance in molecular tunnel junctions. To be submitted to *Phys. Rev. B*.

- [30] Zhanyu Ning, Wei Ji, and Hong Guo. Role of contact formation in transport properties of molecular junctions: conductance of au/bdt/au molecular wires. Being review at Phys. Rev. Lett.
- [31] Wei ji, Zhanyu Ning, and Hong Guo. Manipulation of quantum conductance of molecular wires with interface charging. To be submitted to J. Am. Chem. Soc.
- [32] Zhanyu Ning, Wei Ji, and Hong Guo. Thermal stability and force of mechanical breakdown in molecular wires. To be submitted to Nano Lett.
- [33] Z. Y. Li, W. Sheng, Z. Y. Ning, Z. H. Zhang, Z. Q. Yang, and H. Guo. Magnetism and spin-polarized transport in carbon atomic wires. *Phys. Rev. B*, 80(11):115429, Sep 2009.
- [34] W. Sheng, Z. Y. Li, Z. Y. Ning, Z. H. Zhang, Z. Q. Yang, and H. Guo. Quantum transport in alkane molecular wires: Effects of binding modes and anchoring groups. *J. Chem. Phys.*, 131(24):244712, 2009.
- [35] W. Sheng, Z. Y. Ning, Z. Q. Yang, and H. Guo. Magnetism and perfect spin filtering effect in graphene nanoflakes. *Nanotechnology*, Accepted on Aug.3, 2010.
- [36] Pierre Hohenberg and Walter Kohn. Inhomogeneous electron gas. *Physical Review*, 136(3B):B864, 1964.
- [37] W. Kohn and L. J. Sham. Self-consistent equations including exchange and correlation effects. *Physical Review*, 140(4A):1133, 1965.
- [38] S. H. Vosko, K. A. Jackson, M. R. Pedersen, D. J. Singh, J. P. Perdew, J. A. Chevary, and C. Fiolhais. Atoms, molecules and surfaces: Application of the generalized gradient approximation from exchange and correlation. *Phys. Rev. B*, 46:6671, 1992.

- [39] D. M. Ceperly and B. J. Alder. Ground state of the electron gas by a stochastic method. *J. Chem. Phys.*, 45:566, 1980.
- [40] J. P. Perdew and A. Zunger. Self-interaction correction to densityfunctional approximations for many-electron systems. *Phys. Rev. B*, 23:5048, 1981.
- [41] John P. Perdew and Yue Wang. Accurate and simple analytic representation of the electron-gas correlation energy. *Phys. Rev. B*, 45:13244, 1992.
- [42] U. von Barth and L. Hedin. A local exchange-correlation potential for the spin polarized case. *J. Phys. C:Solid State Phys.*, 5:1629, 1972.
- [43] L. Wilk S. J. Vosko and M. Nusair. Accurate spin-dependent electron liquid correlation energies for local spin density calculations: a critical analysis. *Can. J. Phys.*, 58:1200, 1980.
- [44] K. Burke, J. P. Perdew, and M. Ernzerhof. Generalized gradient approximation made simple. *Phys. Rev. Lett.*, 77:3865, 1996.
- [45] B. Hammer, L. B. Hansen, and J. K. Nørskov. Improved adsorption energetics within density-functional theory using revised perdedw-burke-ernzerhof functionals. *Phys. Rev. B*, 59(11):7413–7421, Mar 1999.
- [46] C. Lee, W. Yang, and R. G. Parr. Development of the colle-salvetti correlation-energy formula into a functional of the electron density. *Phys. Rev. B*, 37:785, 1988.
- [47] A. D. Becke. Density functional thermochemistry. iii. the role of exact exchange. *J. Chem. Phys.*, 98:5648, 1993.
- [48] A. D. Becke. Exploring the limits of gradient corrections in density functional theory. *J. Comp. Chem.*, 20:63, 1999.
- [49] Jianmin Tao, John P. Perdew, Viktor N. Staroverov, and Gustavo E. Scuseria. Climbing the density functional ladder: Nonempirical meta-generalized gradient

- approximation designed for molecules and solids. *Phys. Rev. Lett.*, 91:146401, 2003.
- [50] O. A. Vydrov and G. E. Scuseria. Effect of the perdew-zunger self-interaction correction on the thermochemical performance of approximate density functionals. *J. Chem. Phys.*, 121:8187, 2004.
- [51] Derek Waldron. Ab-initio simulation of spintronic devices. *PhD thesis, McGill University*, 2007.
- [52] www.nanoacademic.ca. Nanodcal is an *ab-initio* code based on dft-negf method developed by dr. lei liu in nanoacademic company. 2010.
- [53] José M. Soler, Emilio Artacho, Julian D. Gale, Alberto García, Javier Junquera, Pablo Ordejón, and Daniel Sánchez-Portal. The siesta method for ab initio order-n materials simulation. *J. Phys.: Condens. Matter*, 14:2745, 2002.
- [54] G. Kresse and J. Hafner. Ab initio molecular dynamics for liquid metals. *Phys. Rev. B*, 47(1):558–561, Jan 1993.
- [55] G. Kresse and J. Hafner. Ab initio molecular-dynamics simulation of the liquid-metal–amorphous-semiconductor transition in germanium. *Phys. Rev. B*, 49(20):14251–14269, May 1994.
- [56] G. Kresse and J. Furthmüller. Efficient iterative schemes for ab initio total-energy calculations using a plane-wave basis set. *Phys. Rev. B*, 54(16):11169–11186, Oct 1996.
- [57] G. Kresse and J. Furthmüller. Efficiency of *ab-initio* total energy calculations for metals and semiconductors using a plane-wave basis set. *Comput. Mat. Sci.*, 6:15, 1996.
- [58] VASP code <http://cms.mpi.univie.ac.at/vasp/>.
- [59] P. Blaha, K. Schwarz, G. Madsen, D. Kvasicka, and J. Luitz. *WIEN2k (Technical University of Vienna)*.

- [60] S Cottenier. *Density Functional Theory and The Family of (L) APW-Methods: A Step-by-Step Introduction*, Instituut Voor Kern-en Stralingsfysica: K. U. Leuven, Belgium.
- [61] A. Cheng and D. T. Cheng. Heritage and early history of the boundary element method. *Engineering Analysis with Boundary Elements*, 29.
- [62] www.nanoacademic.ca. Nabase is a pseudo potential and lcao-type basis generator developed by dr. yu zhu in nanoacademic company. 2010.
- [63] Paolo Giannozzi. Notes on pseudopotential generation, available at <http://www.nest.sns.it/~giannozz>. 2004.
- [64] M. J. Frisch et al. Gaussian98(gaussian inc. pittsburg, pa).
- [65] W. H. Press, B. P. Flannery, S. A. Teukolsky, and W. T. Vetterling. "downhill simplex method in multidimensions" and "linear programming and the simplex method." chapter 10.4 and 10.8 in numerical recipes in fortran: The art of scientific computing, 2nd edition. 1992.
- [66] Javier Junquera, Óscar Paz, Daniel Sánchez-Portal, and Emilio Artacho. Numerical atomic orbitals for linear-scaling calculations. *Phys. Rev. B*, 64(23):235111, Nov 2001.
- [67] Paul Michael Haney. Spintronics in ferromagnets and antiferromagnets from first principles. *PhD thesis, The University of Texas at Austin*, August 2007.
- [68] Rolf Landauer. Can a length of perfect conductor have a resistance? *Physics Letters A*, 85:91, 1981.
- [69] Rolf Landauer. *IBM J. Res. Dev.*, 1:223, 1957.
- [70] Supriyo Datta. Electronic transport in mesoscopic systems. 1995.

- [71] Eldon G. Emberly and George Kirczenow. Landauer theory, inelastic scattering, and electron transport in molecular wires. *Phys. Rev. B*, 61(8):5740–5750, Feb 2000.
- [72] Hartmut J. W. Haug and Antti-Pekka Jauho. Quantum kinetics in transport and optics of semiconductors. 1997.
- [73] Jeremy Taylor. Ab-initio modeling of transport in atomic scale device. *PhD thesis, McGill University*, 2000.
- [74] Yigal Meir and Ned S. Wingreen. Landauer formula for the current through an interacting electron region. *Phys. Rev. Lett.*, 68(16):2512–2515, Apr 1992.
- [75] S. Sanvito, C. J. Lambert, J. H. Jefferson, and A. M. Bratkovsky. General green’s-function formalism for transport calculations with *spd* hamiltonians and giant magnetoresistance in co- and ni-based magnetic multilayers. *Phys. Rev. B*, 59(18):11936–11948, May 1999.
- [76] F M P Lopez Sancho, J M Lopez Sancho, and J Rubio. Quick iterative scheme for the calculation of transfer matrices: application to mo (100). *J. Phys. F: Met. Phys.*, 14:1205, 1984.
- [77] T. Jungwirth, Jairo Sinova, J. Mašek, J. Kučera, and A. H. MacDonald. Theory of ferromagnetic (iii,mn)v semiconductors. *Rev. Mod. Phys.*, 78(3):809–864, Aug 2006.
- [78] T. Jungwirth, Qian Niu, and A. H. MacDonald. Anomalous hall effect in ferromagnetic semiconductors. *Phys. Rev. Lett.*, 88(20):207208, May 2002.
- [79] G. Binasch, P. Grünberg, F. Saurenbach, and W. Zinn. Enhanced magnetoresistance in layered magnetic structures with antiferromagnetic interlayer exchange. *Phys. Rev. B*, 39(7):4828–4830, Mar 1989.

- [80] William J. Gallagher and Stuart S. P. Parkin. Development of the magnetic tunnel junction mram at ibm: From first junctions to a 16-mb mram demonstrator chip. *IBM*, 2006.
- [81] Rajagopalan Desikan, Charles R. Lefurgy, Stephen W. Keckler, and Doug Burger. On-chip mram as a high-bandwidth, low-latency replacement for dram physical memories. *Computer Architecture and Technology Laboratory, Department of Computer Sciences, The University of Texas at Austin*, 2002.
- [82] http://en.wikipedia.org/wiki/giant_magnetoresistance.
- [83] W. H. Butler, X.-G. Zhang, T. C. Schulthess, and J. M. MacLaren. Spin-dependent tunneling conductance of $fe|mgo|fe$ sandwiches. *Phys. Rev. B*, 63(5):054416, Jan 2001.
- [84] J. Mathon and A. Umerski. Theory of tunneling magnetoresistance of an epitaxial $fe/mgo/fe(001)$ junction. *Phys. Rev. B*, 63(22):220403, May 2001.
- [85] Stuart S. P. Parkin, Christian Kaiser, Alex Panchula, Philip M. Rice, Brian Hughes, Mahesh Samant, and See-Hun Yang. Giant tunnelling magnetoresistance at room temperature with $mgo(100)$ tunnel barriers. *Nat. Mater.*, 3:862, 2004.
- [86] Shinji Yuasa, Taro Nagahama, Akio Fukushima, Yoshishige Suzuki, and Koji Ando. Giant room-temperature magnetoresistance in single-crystal $fe/mgo/fe$ magnetic tunnel junctions. *Nature Mater.*, 3:868, 2004.
- [87] S. Ikeda, J. Hayakawa, Y. Ashizawa, Y. M. Lee, K. Miura, H. Hasegawa, M. Tsunoda, F. Matsukura, and H. Ohno. Tunnel magnetoresistance of 604% at 300 k by suppression of ta diffusion in $cofeb/mgo/cofeb$ pseudo-spin-valves annealed at high temperature. *App. Phys. Lett.*, 93:082508, 2008.

- [88] Kazuhito Tsukagoshi, Bruce W. Alphenaar, and Hiroki Ago. Coherent transport of electron spin in a ferromagnetically contacted carbon nanotube. *Nature*, 401:572, 1999.
- [89] V. Dediu, M. Murgia, F. C. Matocota, C. Taliania, and S. Barbanerab. Room temperature spin polarized injection in organic semiconductor. *Solid State Commun.*, 122:181, 2002.
- [90] Min Ouyang and David D. Awschalom. Coherent spin transfer between molecularly bridged quantum dots. *Science*, 301:1074, 2003.
- [91] Z. H. Xiong, Di Wu, Z. Vally Vardeny, and Jing Shi. Giant magnetoresistance in organic spin-valves. *Nature*, 427:821, 2003.
- [92] T. X. Wang, H. X. Wei, Z. M. Zeng, X. F. Han, Z. M. Hong, and G. Q. Shi. Magnetic/nonmagnetic/magnetic tunnel junction based on hybrid organic langmuir-blodgett-films. *App. Phys. Lett.*, 88:242505, 2006.
- [93] W. Harneit, C. Boehme, S. Schaefer, K. Huebener, K. Fostiropoulos, and K. Lips. Room temperature electrical detection of spin coherence in *c60*. *Phys. Rev. Lett.*, 98(21):216601, May 2007.
- [94] S. Pramanik, C.-G. Stefanita, S. Patibandla, S. Bandyopadhyay, K. Garre, N. Harth, and M. Cahay. Observation of extremely long spin relaxation times in an organic nanowire spin valve. *Nat. Nanotec.*, 2:216, 2007.
- [95] H. Mehrez, Jeremy Taylor, Hong Guo, Jian Wang, and Christopher Roland. Carbon nanotube based magnetic tunnel junctions. *Phys. Rev. Lett.*, 84(12):2682–2685, Mar 2000.
- [96] Ranjit Pati, Laxmidhar Senapati, Pulikel M. Ajayan, and Saroj K. Nayak. First-principles calculations of spin-polarized electron transport in a molecular wire: Molecular spin valve. *Phys. Rev. B*, 68(10):100407, Sep 2003.

- [97] L. Senapati, R. Pati, and S. C. Erwin. Controlling spin-polarized electron transport through a molecule: The role of molecular conformation. *Phys. Rev. B*, 76(2):024438, Jul 2007.
- [98] Eldon G. Emberly, , and George Kirczenow. Molecular spintronics: spin-dependent electron transport in molecular wires. *Chem. Phys.*, 281:311, 2002.
- [99] Hugh Dalglish and George Kirczenow. Inverse magnetoresistance of molecular junctions. *Phys. Rev. B*, 72(18):184407, Nov 2005.
- [100] Rui Liu, San-Huang Ke, Harold U. Baranger, and Weitao Yang. Organometallic spintronics: Dicobaltocene switch. *Nano Lett.*, 5:1959, 2005.
- [101] Alexandre R. Rocha, Vctor M. García-suárez, Steve W. Bailey, Colin J. Lambert, Jaime Ferrer, and Stefano Sanvito. Towards molecular spintronics. *Nat. Mater.*, 4:335, 2005.
- [102] Lei Liu Derek Waldron and Hong Guo. Ab initio simulation of magnetic tunnel junctions. *Nanotechnology*, 18:424026, 2007.
- [103] Bin Wang, Yu Zhu, Wei Ren, Jian Wang, and Hong Guo. Spin-dependent transport in fe-doped carbon nanotubes. *Phys. Rev. B*, 75(23):235415, Jun 2007.
- [104] Igor Žutić, Jaroslav Fabian, and S. Das Sarma. Spintronics: Fundamentals and applications. *Rev. Mod. Phys.*, 76(2):323–410, Apr 2004.
- [105] M. Julliere. Tunneling between ferromagnetic films. *Phys. Lett.*, 54A:225, 1975.
- [106] G. A. de Wijs and R. A. de Groot. Towards 100nmnsb/cds interface. *Phys. Rev. B*, 64(2):020402, Jun 2001.
- [107] M. I. Katsnelson, V. Yu. Irkhin, L. Chioncel, A. I. Lichtenstein, and R. A. de Groot. Half-metallic ferromagnets: From band structure to many-body effects. *Rev. Mod. Phys.*, 80(2):315–378, Apr 2008.

- [108] J. M. D. Coey and M. Venkatesan. Half-metallic ferromagnetism: Example of cro_2 . *J. Appl. Phys.*, 91:8345, 2002.
- [109] J. M. Pruneda, V. Ferrari, R. Rurali, P. B. Littlewood, N. A. Spaldin, and Emilio Artacho. Ferrodistortive instability at the (001) surface of half-metallic manganites. *Phys. Rev. Lett.*, 99(22):226101, Nov 2007.
- [110] L. A. Bumm, J. J. Arnold, T. D. Dunbar, D. L. Allara, and P. S. Weiss. Electron transfer through organic molecules. *J. Phys. Chem. B*, 103:8122, 1999.
- [111] David J. Wold and C. Daniel Frisbie. Fabrication and characterization of metal/molecule/metal junctions by conducting probe atomic force microscopy. *J. Am. Chem. Soc.*, 123:5549, 2001.
- [112] X. D. Cui, X. Zarate, J. Tomfohr, O. F. Sankey, A. Primak, A. L. Moore, T. A. Moore, D. Gust, G. Harris, and S. M. Lindsay. Making electrical contacts to molecular monolayers. *Nanotechnology*, 13:5, 2002.
- [113] Wenyong Wang, Takhee Lee, and M. A. Reed. Mechanism of electron conduction in self-assembled alkanethiol monolayer devices. *Phys. Rev. B*, 68(3):035416, Jul 2003.
- [114] O. Wunnicke, N. Papanikolaou, R. Zeller, P. H. Dederichs, V. Drchal, and J. Kudrnovský. Effects of resonant interface states on tunneling magnetoresistance. *Phys. Rev. B*, 65(6):064425, Jan 2002.
- [115] Derek Waldron, Vladimir Timoshevskii, Yibin Hu, Ke Xia, and Hong Guo. First principles modeling of tunnel magnetoresistance of $fe/mgo/fe$ trilayers. *Phys. Rev. Lett.*, 97(22):226802, Nov 2006.
- [116] Richard L. McCreery. Molecular electronic junctions. *Chem. Mater.*, 16:4477, 2004.

- [117] Michael Galperin, Mark A. Ratner, Abraham Nitzan, and Alessandro Troisi. Nuclear coupling and polarization in molecular transport junctions: Beyond tunneling to function. *Science*, 319:1056, 2008.
- [118] Yibin Hu, Yu Zhu, Hongjun Gao, and Hong Guo. Conductance of an ensemble of molecular wires: A statistical analysis. *Phys. Rev. Lett.*, 95(15):156803, Oct 2005.
- [119] C. Toher and S. Sanvito. Efficient atomic self-interaction correction scheme for nonequilibrium quantum transport. *Phys. Rev. Lett.*, 99(5):056801, Jul 2007.
- [120] P. Delaney and J. C. Greer. Correlated electron transport in molecular electronics. *Phys. Rev. Lett.*, 93(3):036805, Jul 2004.
- [121] K. Stokbro, J. Taylor, M. Brandbyge, J. L. Mozos, and P. Ordejón. Theoretical study of the nonlinear conductance of di-thiol benzene coupled to $\text{Au}(111)$ surfaces via thiol and thiolate bonds. *Comp. Mat. Sci.*, 27:151, 2003.
- [122] San-Huang Ke, Harold U. Baranger, and Weitao Yang. Molecular conductance: Chemical trends of anchoring groups. *J. Am. Chem. Soc.*, 126:15897, 2004.
- [123] San-Huang Ke, Harold U. Baranger, and Weitao Yang. Models of electrodes and contacts in molecular electronics. *J. Chem. Phys.*, 123:114701, 2005.
- [124] San-Huang Ke, Harold U. Baranger, and Weitao Yang. Electron transport through single conjugated organic molecules: basis set effects in ab initio calculations. *J. Chem. Phys.*, 127:144107, 2007.
- [125] M. Strange, I. S. Kristensen, K. S. Thygesen, and K. W. Jacobsen. Benchmark density functional theory calculations for nanoscale conductance. *J. Chem. Phys.*, 128:114714, 2008.
- [126] Makusu Tsutsui, Kohei Shoji, Masateru Taniguchi, and Tomoji Kawai. Formation and self-breaking mechanism of stable atom-sized junctions. *Nano Lett.*, 9:2433, 2008.

- [127] Emanuel Lörtscher, Heiko B. Weber, and Heike Riel. Statistical approach to investigating transport through single molecules. *Phys. Rev. Lett.*, 98(17):176807, Apr 2007.
- [128] Shu Kurokawa Makusu Tsutsui, Yumi Teramae and Akira Sakai. High-conductance states of single benzenedithiol molecules. *App. Phys. Lett.*, 89:163111, 2006.
- [129] Manabu Kiguchi, Shinichi Miura, Kenji Hara, Masaya Sawamura, and Kei Murakoshi. Conductance of a single molecule anchored by an isocyanide substituent to gold electrodes. *App. Phys. Lett.*, 89:213104, 2006.
- [130] M. Di Ventra, S. T. Pantelides, and N. D. Lang. The benzene molecule as a molecular resonant-tunneling transistor. *App. Phys. Lett.*, 76:3448, 2000.
- [131] Jun Nara, W. T. Geng, Hiori Kino, Nobuhiko Kobayashi, and Takahisa Ohno. Theoretical investigation on electron transport through an organic molecule: Effect of the contact structure. *J. Chem. Phys.*, 121:6485, 2004.
- [132] Tomofumi Tada, Masakazu Kondo, and Kazunari Yoshizawa. Greens function formalism coupled with gaussian broadening of discrete states for quantum transport: Application to atomic and molecular wires. *J. Chem. Phys.*, 121:8050, 2004.
- [133] Gemma C. Solomon, Jeffrey R. Reimers, and Noel S. Hush. Overcoming computational uncertainties to reveal chemical sensitivity in single molecule conduction calculations. *J. Chem. Phys.*, 122:224502, 2005.
- [134] Renato B. Pontes, Frederico D. Novaes, Adalberto Fazzio, and Antônio J. R. da Silva. Adsorption of benzene-1,4-dithiol on the au(111) surface and its possible role in molecular conductance. *J. Am. Chem. Soc.*, 128:8996, 2006.

- [135] David Q. Andrews, Revital Cohen, Richard P. Van Duyne, and Mark A. Ratner. Single molecule electron transport junctions: Charging and geometric effects on conductance. *J. Chem. Phys.*, 125:174718, 2006.
- [136] David Q. Andrews, Richard P. Van Duyne, and Mark A. Ratner. Stochastic modulation in molecular electronic transport junctions: Molecular dynamics coupled with charge transport calculations. *Nano Lett.*, 8:1120, 2008.
- [137] Chao-Cheng Kaun, Brian Larade, and Hong Guo. Electrical transport through oligophenylene molecules: A first-principles study of the length dependence. *Phys. Rev. B*, 67(12):121411, Mar 2003.
- [138] Thomas Frederiksen, Mads Brandbyge, Nicolás Lorente, and Antti-Pekka Jauho. Inelastic scattering and local heating in atomic gold wires. *Phys. Rev. Lett.*, 93(25):256601, Dec 2004.
- [139] Fang-Sen Li, Wancheng Zhou, and Quanmin Guo. Uncovering the hidden gold atoms in a self-assembled monolayer of alkanethiol molecules on au(111). *Phys. Rev. B*, 79(11):113412, Mar 2009.
- [140] Izabela I. Rzeźnicka, Junseok Lee, Petro Maksymovych, and Jr. John T. Yates. Nondissociative chemisorption of short chain alkanethiols on au(111). *J. Phys. Chem. B*, 109:15992, 2005.
- [141] Jian-Ge Zhou and Frank Hagelberg. Do methanethiol adsorbates on the au(111) surface dissociate? *Phys. Rev. Lett.*, 97(4):045505, Jul 2006.
- [142] Zhifeng Huang, Bingqian Xu, Yuchang Chen, Massimiliano Di Ventra, and Nongjian Tao. Measurement of current-induced local heating in a single molecule junction. *Nano Lett.*, 6:1240, 2006.
- [143] Makusu Tsutsui, Masateru Taniguchi, and Tomoji Kawai. Quantitative evaluation of metal-molecule contact stability at the single-molecule level. *J. Am. Chem. Soc.*, 131:10552, 2009.

-
- [144] N. Troullier and José Luriaas Martins. Efficient pseudopotentials for plane-wave calculations. *Phys. Rev. B*, 43(3):1993–2006, Jan 1991.
- [145] Wei Ji, Zhong-Yi Lu, and Hong-Jun Gao. Multichannel interaction mechanism in a molecule-metal interface. *Phys. Rev. B*, 77(11):113406, Mar 2008.
- [146] Leonard Kleinman and D. M. Bylander. Efficacious form for model pseudopotentials. *Phys. Rev. Lett.*, 48(20):1425–1428, May 1982.
- [147] Latha Venkataraman, Jennifer E. Klare, Iris W. Tam, Colin Nuckolls, Mark S. Hybertsen, and Michael L. Steigerwald. Single-molecule circuits with well-defined molecular conductance. *Nano Lett.*, 6:458, 2006.